FINITE ELEMENT ANALYSIS OF BALLISTIC PENETRATION OF PLAIN WEAVE TWARON CT709® FABRICS: A PARAMETRIC STUDY

A Thesis

by

SIREESHA GOGINENI

Submitted to the Office of Graduate Studies of
Texas A&M University
in partial fulfillment of the requirements for the degree of

MASTER OF SCIENCE

August 2010

Major Subject: Mechanical Engineering

Finite Element Analysis of Ballistic Penetration of Plain Weave Twaron CT709®

Fabrics: A Parametric Study.

FINITE ELEMENT ANALYSIS OF BALLISTIC PENETRATION OF PLAIN WEAVE TWARON CT709® FABRICS: A PARAMETRIC STUDY

A Thesis

by

SIREESHA GOGINENI

Submitted to the Office of Graduate Studies of
Texas A&M University
in partial fulfillment of the requirements for the degree of

MASTER OF SCIENCE

Approved by:

Chair of Committee,	Xin-Lin Gao
Committee Members,	Junuthula N. Reddy
	Zoubeida Ounaies
Head of Department,	Dennis O'Neal

August 2010

Major Subject: Mechanical Engineering

ABSTRACT

Finite Element Analysis of Ballistic Penetration of Plain Weave Twaron CT709® Fabrics: A Parametric Study.

(August 2010)

Sireesha Gogineni, B.E., Osmania University

Chair of Advisory Committee: Dr. Xin-Lin Gao

The ballistic impact of Twaron CT709® plain weave fabrics is studied using an explicit finite element method. Many existing approximations pertaining to woven fabrics cannot adequately represent strain rate-dependent behavior exhibited by the Twaron fabrics. One-dimensional models based on linear viscoelasticity can account for rate dependency but are limited by the simplifying assumptions on the fabric architecture and stress state. In the current study, a three-dimensional fabric model is developed by treating each individual yarn as a continuum. The yarn behavior is phenomenologically described using a three-dimensional linear viscoelastic constitutive relation. A user subroutine VUMAT for ABAQUS/Explicit® is developed to incorporate the constitutive behavior.

By using the newly developed viscoelasticity model, a parametric study is carried out to analyze the effects of various parameters on the impact behavior of the Twaron fabrics, which include projectile shape and mass, gripping conditions, inter-yarn friction, and the number of fabric layers. The study leads to the determination of the optimal

number of fabric layers and the optimized level of inter-yarn friction that are needed to achieve the maximum energy absorption at specified impact speeds.

The present study successfully utilizes the combination of 3D weave architecture and the strain rate dependent material behavior. Majority of the existing work is based either on geometry simplification or assumption of elastic material behavior. Another significant advantage with the present approach is that the mechanical constitutive relation, coded in FORTRAN®, is universal in application. The desired material behavior can be obtained by just varying the material constants in the code. This allows for the extension of this work to any fabric material which exhibits a strain-rate dependent behavior in addition to Twaron®.

The results pertaining to optimal number of fabric layers and inter-yarn friction levels can aid in the manufacturing of fabric with regard to the desired level of lubrication/additives to improve the fabric performance under impact.

Dedicated to my parents

ACKNOWLEDGEMENTS

First and foremost, I would like to thank my research advisor, Dr. Xin-Lin Gao, for his encouragement and patient support throughout the period of my thesis. I would also like to thank Dr. Frank Richter for his expert advice and helping me de-bug my code. I'm grateful to Rahul and David for their help during the initial stages of the projects. I will always be grateful to my family for their love and support through the years, without which I could not have completed this assignment. Finally, I'd like to thank my friends Ashish, Bhanu, Sarat, Kalpana, Nishitha, Swetha, and Vandana, for the many discussions both on and off research.

TABLE OF CONTENTS

Page

ABSTRACT iii

ACKNOWLEDGEMENTS vi

TABLE OF CONTENTS vii

LIST OF FIGURES ix

LIST OF TABLES xiv

1. INTRODUCTION 1

    1.1 Armor systems 1
    1.2 Impact experiments 2
    1.3 Fabrics in ballistic applications 5
    1.4 Existing models and methods 7
        1.4.1 Analytical models 8
        1.4.2 Empirical models 9
        1.4.3 Numerical methods 9
        1.4.4 FE models of plain weave fabrics 11
    1.5 Penetration mechanics 19
        1.5.1 Penetration and failure in fabric targets 20
        1.5.2 Fabric failure mechanisms 23
    1.6 Introduction to FE method 26
        1.6.1 Theory of FE method 26
        1.6.2 Explicit time integration 31

2. FINITE ELEMENT MODEL OF BALLISTIC IMPACT 34

    2.1 Geometry models of plain weave Twaron® fabric and projectile 34
    2.2 Materials for Twaron® and projectile 40
    2.3 Contact between the fabric and projectile 41
    2.4 Meshing scheme of the fabric and the projectile 43

3. DEFINITION OF TWARON® MATERIAL BEHAVIOR 46

    3.1 Viscoelastic behavior 46
    3.2 Constitutive modeling: 3D linear viscoelastic model 48

Page

3.3 Implementation of 3D constitutive equation: subroutine VUMAT 51
3.4 VUMAT algorithm 57
3.5 VUMAT testing and validation 58

4. NUMERICAL SIMULATION RESULTS, DISCUSSION AND CONCLUSION. 71

4.1 Validation 71
4.2 Parametric study 73
4.2.1 Test series I: simulation of a 9mm diameter cylindrical bullet (8g) impacting fabric at different velocities 76
4.2.2 Test series II: simulation for different projectile masses at impact velocity of 250 m/s 91
4.2.3 Test series III: simulation for three projectile shapes at impact velocity of 332 m/s 93
4.2.4 Test series IV: simulation for different gripping conditions 108
4.2.5 Test series V: simulation of 8g, hemi-spherical projectile impact for 1- , 2-, 3-, and 4- fabric layers 125
4.2.6 Test series VI: simulations for studying frictional effects on energy absorbed by the fabric 128
4.3 Conclusions and future work 135
4.3.1 Impact velocity 136
4.3.2 Projectile mass 136
4.3.3 Projectile shape 137
4.3.4 Gripping conditions 137
4.3.5 Number of fabric layers 138
4.3.6 Friction 138

REFERENCES 141

VITA 146

LIST OF FIGURES

FIGURE		Page
1-1	Schematic arrangement for ballistic testing [4]	4
1-2	Traditional weave types [5]	6
1-3	Typical non-traditional weave constructions [6]	7
1-4	Cone formation during ballistic impact [8]	8
1-5	Network of bar elements [12]	12
1-6	3D shell model for fabric [13]	13
1-7	Finite element model using membrane elements [14]	14
1-8	Twaron® plain weave fabric cross-section [15]	15
1-9	Twaron® fabric geometry model [15]	15
1-10	Global and local solution domain [16]	16
1-11	3D single yarn crossover [17]	17
1-12	Transverse impact on single yarn [20]	20
1-13	Top and side view of fabric just after the impact [21]	21
1-14	Top and side view showing the transverse wave propagation [21]	21
1-15	Material volume under consideration	27
2-1	Yarn crimp wave	35
2-2	Unit cell of a loosely woven plain weave fabric [32]	36
2-3	(a) Geometric model of yarn crimp and (b) yarn cross section	36
2-4	3D yarn model	37

FIGURE Page

2-5 Spatially varying material coordinates 38

2-6 Plain weave Twaron® fabric 3D geometry: quarter model 38

2-7 (a) Geometry properties and (b) quarter models of the bullets 39

2-8 Fabric-projectile system: FE model 40

2-9 Global contact search 42

2-10 Yarn mesh 44

2-11 (a) fabric mesh and (b) bullet mesh 44

3-1 Termonia and Smith's polymer model [25] 46

3-2 Three element spring-dashpot model (GKV model) 47

3-3 Generalized Maxwell model [24] 49

3-4 Standard linear solid ($GM^{n=1}$) 50

3-5 Standard linear solid model with different coefficients 50

3-6 VUMAT and FE solver interface 55

3-7 Material vector in reference and deformed configurations 56

3-8 Flowchart for VUMAT 57

3-9 Stress-strain curves for low strain rates [24] ($\dot{\varepsilon} < 400s^{-1}$) 58

3-10 Stress-strain curves for high strain rates [24] ($\dot{\varepsilon} \geq 400s^{-1}$) 59

3-11 (a) Viscoelastic bar with uniaxial loading (b) Mesh consisting of four C3D8R elements 61

3-12 Applied load 62

3-13 Principal axial stress at (a) t = 250μs (b) t = 600μs (c) t = 1000μs 62

FIGURE Page

3-14 Principal axial strain at (a) t = 250 μs (b) t = 600μs (c) t = 1000μs 64

3-15 Stress-strain curves for the material at different strain rates 66

3-16 Comparison of strain histories for stress at (a) 50 MPa, (b) 200 MPa, (c) 500 MPa, and (d) 900 MPa 68

4-1 Residual vs. Impact velocity (m/s) 72

4-2 Fabric transverse deformation profile for impact velocity of 250 m/s 77

4-3 Bullet residual velocity for impact velocity of 250 m/s 79

4-4 Kinetic energy loss for impact velocity of 250 m/s 80

4-5 Bullet residual velocity for impact velocity of 332 m/s 80

4-6 Kinetic energy loss for impact velocity of 332 m/s 81

4-7 Fabric transverse deformation profile for impact velocity of 358 m/s 82

4-8 Bullet residual velocity for impact velocity of 358 m/s 85

4-9 Kinetic energy loss for impact velocity of 358 m/s 85

4-10 Bullet residual velocity for impact velocity of 427 m/s 86

4-11 Kinetic energy loss for impact velocity of 427 m/s 86

4-12 Energy absorbed by the fabric for different impact velocities 87

4-13 Variation of frictional dissipation 88

4-14 Variation in contact force with projectile velocity 90

4-15 Residual velocity of bullet 91

4-16 Strain energy rise in the fabric 92

4-17 Residual velocity as a function of projectile mass 93

FIGURE Page

4-18 Three projectile shapes used for simulation 94

4-19 Fabric deformation for a hemi-spherical projectile 95

4-20 Fabric deformation for a spherical projectile 98

4-21 Fabric deformation for a cylindrical projectile 101

4-22 Residual velocity of the projectile with different shapes 104

4-23 Kinetic energy lost by the projectile 105

4-24 Strain energy rise in the fabric for different projectile shapes 106

4-25 Contact force history for spherical and hemi-spherical projectiles 107

4-26 Transverse displacement of the fabric at a low impact velocity of 100 m/s for the case of all four edges clamped 109

4-27 Transverse displacement of the fabric at low a impact velocity of 100 m/s for the case of two edges clamped 112

4-28 Kinetic energy lost by the projectile at the impact velocity of 100 m/s 116

4-29 Strain energy gained by the fabric at the impact velocity of 100 m/s 116

4-30 Transverse displacement of fabric at high impact velocity of 332 m/s for the case of all four edges clamped 117

4-31 Transverse displacement of the fabric at a high impact velocity of the case of 332 m/s for two edges clamped 119

4-32 Kinetic energy lost by the projectile at the impact velocity of 332 m/s 122

4-33 Strain energy gained by the fabric at the impact velocity of 332 m/s 122

4-34 Strain history for element 1714 for the two gripping conditions 124

4-35 Fabric layers 125

4-36 Residual velocity for different fabric layers 126

FIGURE Page

4-37 Strain energy rise in the fabric layer system 127

4-38 Fabric deformation history for (a) f =0.01 (b) f =0.5..... 129

4-39 Kinetic energy lost by the projectile for different friction coefficients..... 131

4-40 Increase in the fabric strain energy 132

4-41 Frictional dissipation in the fabric..... 132

4-42 von Mises stress history for an element near impact zone..... 134

LIST OF TABLES

TABLE		Page
1-1	Comparison of FE models	18
1-2	Dynamic mechanical properties of Twaron® [15]	25
2-1	Fabric properties [27, 28, 29, 30, 31]	34
2-2	Twaron CT709® yarn mechanical properties	41
3-1	Summary of constitutive equation parameters	60
4-1	Comparison of predicted and measured values of residual velocity	71
4-2	Test series I: Impact velocity variation	73
4-3	Test series II: Variation in projectile mass	74
4-4	Test Series III: Projectile geometry variation	74
4-5	Gripping conditions	75
4-6	Variation in fabric target layers	75
4-7	Variation in inter-yarn friction factor	76
4-8	Comparison of energy variation	88
4-9	List of residual velocities	126
4-10	Comparison of energy history	134

1. INTRODUCTION

1.1 Armor systems

Military systems, especially the ones supporting ground forces are relying on faster and more mobile equipment to counteract the warfare tactics. During the World War II, most models for body armor were too heavy and mobility-restricting for use in the field. Since then increased demand for improved armor led to the development of new armor materials. Materials such as polymer matrix composites and ceramics have gradually replaced earlier metal armor shields. Since 1970's, considerable research has been going on in this field to replace the armor shield with composite materials which offer good strength to weight ratios, chemical resistance and high cut resistance.

A ballistic vest is a personal armor system worn on torso to provide protection against fire-arm projectiles and fragments from explosions. When a bullet strikes body armor, it is caught against layers of woven or laminated fibers. These individual fibers absorb and disperse the impacting kinetic energy of the bullet, causing the bullet to deform. With each successive layer of bullet proof material included, additional energy is absorbed [1].

The materials used for light weight body armor range from silk to new fibers which can be woven into fabrics with excellent ballistic properties. One of the most significant developments in fabric armor systems was DuPont's Kevlar. Although Kevlar fibers continue to find some use today due to their low cost, the Kevlar soft

---

This thesis follows the style of International Journal of Impact Engineering.

armor has its shortcomings. The fabric could not effectively absorb energy of large fragments or high velocity bullets hitting the vest, leading to blunt trauma injuries. High performance fibers such as DSM's Dyneema, Teijin's Twaron, Honeywell's Gold Flex and Spectra and Pinnacle Armor's Dragon skin are much lighter and more ballistic-impact resistant than Kevlar, although they are much more expensive.

Twaron, developed by Azko Nobel, is a synthetic para-aramid fiber [2]. With a high modulus and high heat resistance, it is highly impact resistant. The main characteristics of this high-strength fabric include fatigue resistance and high dimensional stability. The inherent molecular structure is highly oriented which leads to high elastic modulus, low creep and stress relaxation.

1.2 Impact experiments

Impact studies are performed to determine the crashworthiness and the effects of impacting debris or projectiles including bullets.

The study of the performance of an armor system under impact typically involves four different phases [3]. The first phase primarily deals with testing the ability of the armor to resist penetration. The second phase helps determine the optimum number of layers required to prevent penetration by varying bullet speeds and sizes. In the third phase, an extensive medical testing is often performed to determine the amount of impact energy transmitted to the wearer. Such impacts may lead to trauma causing serious damage to internal organs. The final phase involves monitoring the armor's ease

of use without causing any undue stress on the torso. The material resistance against wear and elevated temperatures is also evaluated.

The velocity of the projectile is the most important factor in determining the ballistic performance of armor with the key parameter being the velocity at which no bullets will penetrate the armor. Determining the velocity can be done experimentally, by using analytical models or empirical penetration equations or through a combination of these methods. Each of these methods has inherent limitations that cannot account for the test variability. Ballistic testing has various sources causing variability: test backing materials, bullet, casing, powder and others.

The limitations with experiments are numerous due to the inherent nature of them being destructive by design. They are very expensive to perform in terms of equipment, materials, labor, and time. Also, the stochastic mature of experiments make it difficult to repeat any given experiment or apply the results accurately. A typical test setup for projectile impact is shown in Figure 1-1. For assessing the ballistic performance of light weight armor, a witness plate or a backing material, typically oil-based clay is placed behind the armor. After the impact process, the vest is removed from the clay and the depth of indentation in the clay is measured.

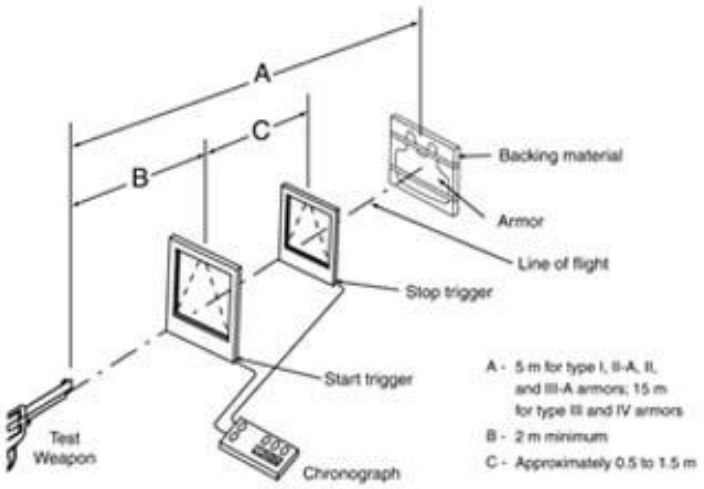

Figure 1-1 Schematic arrangement for ballistic testing [4]

However, as the projectile impact velocity increases the complexity involved in the measurements increases. The physics-based analytical models have shortcomings with regard to the simplifying assumptions used to reduce the governing equations to simpler one- or two- dimensional equations. These models are not capable of examining the details of complex penetration such as the deformation shape.

The use of penetration equations, which are essentially curve-fits of experimental data are limited to the range of conditions in which the experiment is performed. Since it is practically impossible to conduct a real-world impact experiment for every possible scenario, the databases from which the empirical equations are created are limited.

With increasing use of computational methods and the constant refinement of finite element codes and explicit dynamics solvers, it is much simpler and more cost effective to use numerical analysis and simulations to model the impact behavior. Once a model is generated, it can be used to simulate the impact event under prescribed

conditions and to compare the results with available experimental data. Some finite element (FE) modeling parameters like the material properties at various strain rates depend on the experimental data, but the results are not affected by possible experimental errors as the FE modeling is not dependant on curve-fits to impact test data. Thus FE simulation results can be applied in greater confidence in regions where no test data is available.

1.3 Fabrics in ballistic applications

With the development of high strength and high modulus fibers, woven fabrics have found numerous impact-related applications such as protective vests for military personnel, armor plating of vehicles and many other applications involving resistance against high velocity projectile. Though individual yarns have no strength to safeguard against impact, when woven together they possess strength much higher than the sum of individual yarns and a very high strength to weight ratio much higher than that of steel.

Fibers have varied structural properties depending on the class to which they belong. Even the method of weaving the fibers into fabric can have significant impact on the ballistic response. Some examples are aramid fibers, such as Kevlar (DuPont) and Twaron (Teijin); poly fibers such as Zylon (Toyobo); highly processed ultra-high molecular weight polyethylene such as Spectra (Honeywell); and PIPD fibers such as M5.

Figures 1-2 and 1-3 show the different types of fabric configurations. Traditionally, for armor applications, fibers have been woven into unidirectional, plain or basket weave composites.

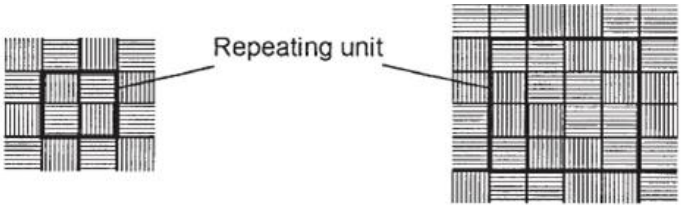

Plain weave Twill weave

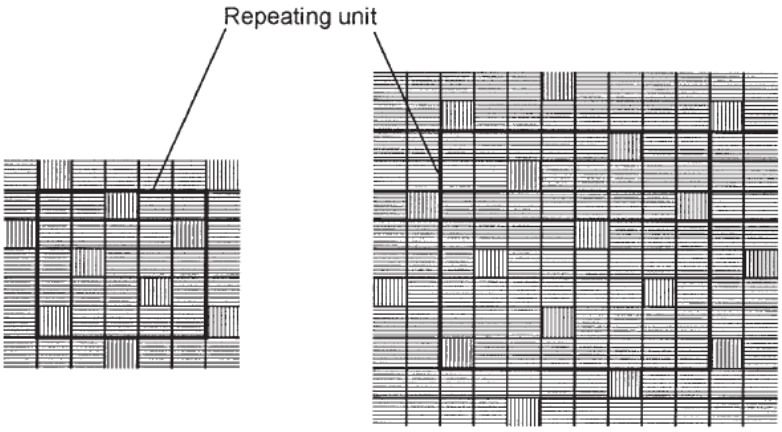

5-Harness satin weave 8-harness satin weave

Figure 1-2 Traditional weave types [5]

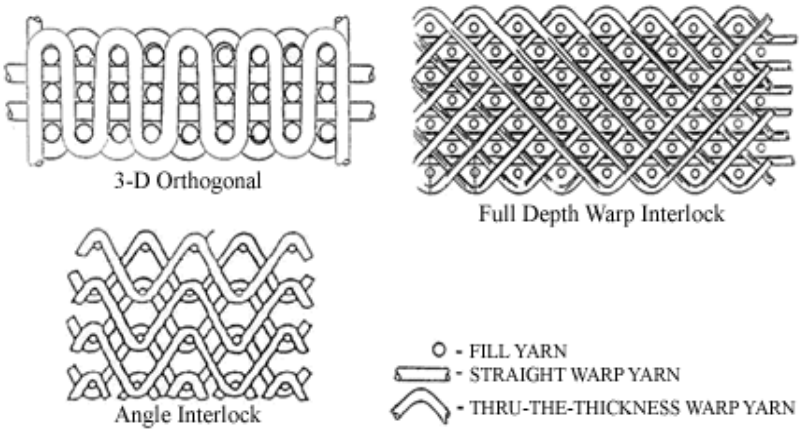

Figure 1-3 Typical non-traditional weave constructions [6]

High velocity impacts on fabrics results in high local deformations with insignificant global structural responses. The nature of damage in woven fabrics depends on many parameters such as the fabric weave, architecture, yarn crimp and various other mechanisms. Hence the study of parameters that affect the energy absorbed during an impact is important.

1.4 Existing models and methods

The study of high-velocity impact is of high importance and there are numerous models available for the same in the literature. Such models can be categorized into two types: one based on the type of model, viz. analytical or numerical; and the other being the type of impact, which is further based on the projectile shape or size, target material or impact velocity.

There are different ways to model ballistic responses of dry woven fabrics. In the following paragraphs, some methodology and theories are discussed.

1.4.1 Analytical models

Analytical models are typically derived from the general continuum mechanics equations for energy and momentum conservation. Gu [7] presented an analytical model to calculate the decrease in kinetic energy of the projectile based on the energy conservation law. He assumed that the decrease in projectile kinetic energy is equal to the kinetic and strain energy of the fabric in the deformed region. However his analysis involves many simplifying assumptions. For instance, the projectile is simplified as a particle and the yarn crimp is neglected.

The analytical model described by Naik et al. [8] considers the energy absorbed due to cone formation (see Figure 1-4) and that due to friction between the projectile and target, in addition to the strain energy of the fabric.

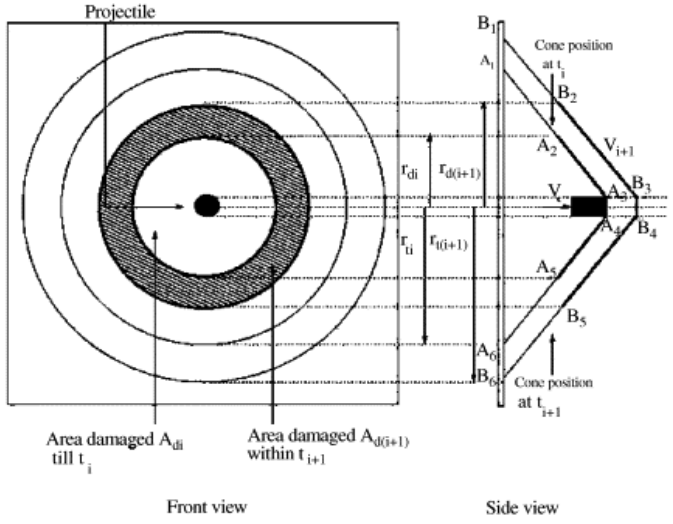

Figure 1-4 Cone formation during ballistic impact [8]

The input data for the model are the material and geometrical properties for the projectile and the target. The analytical equations are solved for the ballistic limit, damage area, contact duration and energy absorbed by each mechanism. This model compares well with experimental results, though the governing equations involve considerable complexity.

Analytical models such as these can handle only simple physical phenomena and tend to become more complex as many variables are involved.

1.4.2 Empirical models

Empirical models are built on experimentally obtained data. Techniques such as curve fitting and non-linear regression methods are used along with statistical analyses. Such models consist of parametric equations which relate the various parameters studied during experiments. These equations can be solved to predict the outcome of an impact event such as the bullet residual velocity.

Empirical penetration equations are of the form f ($x_1, x_2, \dots, x_n$) where $x_1, x_2, \dots, x_n$ are parameters such as projectile size and target thickness. Such models can be applied accurately only to cases which replicate the experimental data to which the equations are fit.

1.4.3 Numerical methods

This method relies on techniques such as the finite difference and finite element methods, using either a Lagrangian (deformable) mesh or an Eulerian (Fixed mesh).

Most of the commercial FE codes today utilize the Lagrangian formulation. One of the early works in impact analysis using computational techniques was carried out by Sedgwick et al. in 1978 [9]. They performed a series of simulations for low velocity and hypervelocity impacts using finite difference based computer code called HELP (abbreviated for Hydrodynamic Elastic Plastic). This Eulerian code solves 2D material flow problems in the hydrodynamic and elastic-plastic regions. Their results for the impact of an aluminum projectile on a thin aluminum plate compared well with experiments. In 1989, Chen [10] performed impact analyses of aluminum targets penetrated by conical-nosed steel projectiles. The simulations were carried out using a finite element code PRONTO 2D. It is a Lagrangian finite element program which uses explicit time integration techniques to solve the equations of motion. This finite element code could accurately predict the residual velocity of a conical nosed steel projectile penetrating a 25.4 mm thick aluminum target. Though such numerical codes give reasonable results for simple target geometries, they have their inherent shortcomings in modeling complex geometries. In comparison, widely used commercial software packages for ballistic impact of fabrics such as ABAQUS, DYNA 3D and LS DYNA, with enhanced design capabilities can provide better and more reliable simulation results in such situations.

The design of a fabric armor system is still largely empirical, partly on account of the difficulty in accurately modeling the fabric behavior and partly due to the high computational time and cost. Recent developments in numerical modeling of fabrics and added functionalities in commercial software packages have helped capture the fabric

behavior better. The interactions between yarns, yarn slippage, inter-yarn friction and the damage and failure of the fabric can be better handled through the use of such commercial packages. Further, these finite element codes also allow one to employ user defined material behavior in place of standard material models.

Numerous finite element models have been developed. Some of these are based on oversimplifying geometries, while others use detailed 3D geometries that provide the yarn level resolution. Few of such models will be discussed in detail in the following sub-sections.

1.4.4 FE models of plain weave fabrics

Most of the FEM based impact deal with a single layer of fabric only. This can be attributed to the inherent complexity in accounting for new energy dissipation mechanisms and interactions amongst the fabric plies.

FE models are often based on underlying simplifying assumptions about the fabric geometry and material properties. The ultimate aim of such models is to replicate the fabric behavior with suitable approximations and reduce the computational time and cost.

Vinson and Zukas [11] modeled fabrics as conical shells. They treated each fabric as isotropic and having no distinct warp and weft directions. This model predicts the transverse deflection as conical shaped, which is contrary to the experimentally observed pyramidal shape.

Ching et al. [12] modeled a fabric using pin-jointed linear or bar elements. Such simplified network-type models with reduced number of degrees of freedom is much less computationally expensive than the detailed full-scale discretization of individual yarns. Their fabric mesh with the orthogonal warp and weft yarns is shown in Figure 1-5.

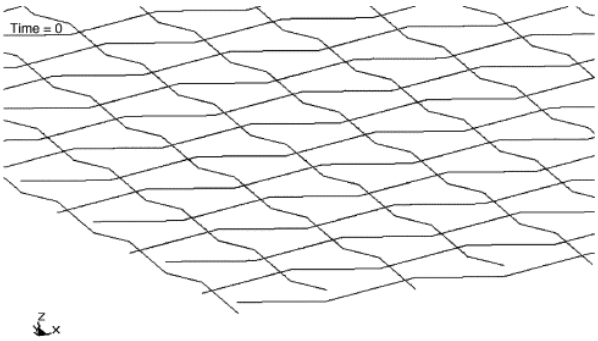

Figure 1-5 Network of bar elements [12]

This FE model accounts for several representative features of the woven fabric architecture such as sliding of yarns, yarn crimping and strain rate dependant material behavior. The simulations performed using LS-DYNA, showed good agreement with the measured residual velocities of the projectile.

A shell model for impact was proposed by Shockey et al.[13]. The model idealizes a fabric as an orthotropic continuum. The fabric model is shown in Figure 1-6, with the two orthogonal directions corresponding to the warp & weft orientations of yarns.

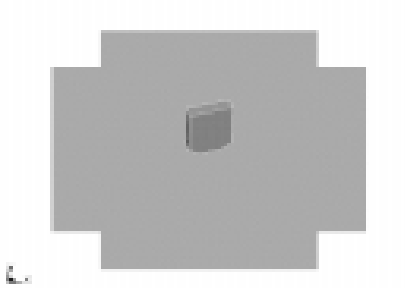

Figure 1-6 3D shell model for fabric [13]

The young's modulus was calculated by measuring the yarn load at 1% strain and multiplying it with the yarn pitch. The resultant load was then distributed over the fabric thickness. Also, the Poisson's ratio was assumed to be zero in all directions. The effect of design variables such as yarn pitch, number of fabric plies and gripping conditions were evaluated. Though this model simulates the impact response of the fabric accurately, it lacks well-defined failure mechanisms such as yarn slippage and yarn pull-out in the principal yarns.

Lim et al. [14] modeled the ballistic impact on Twaron® fabrics using membrane elements. The impact event was analyzed using the finite element code DYNA3D. The fabric and projectile were modeled together to simulate the stress wave propagation from the point of projectile impact on the fabric. The membrane finite element model is shown in Figure 1-7.

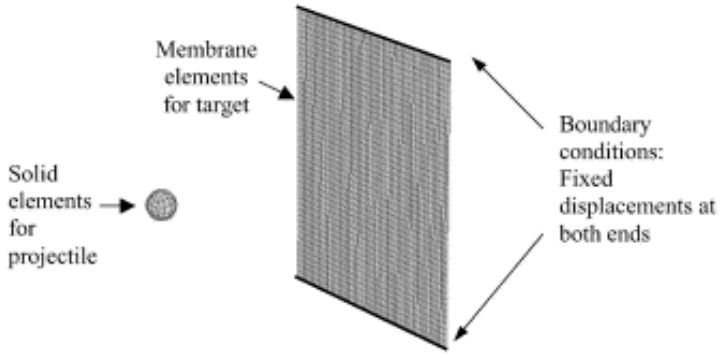

Figure 1-7 Finite element model using membrane elements [14]

This model does not consider various frictional effects during the impact process. Though the shell or membrane models partly resemble the actual fabric, the details of woven architecture are lost with such assumptions. Typical characteristics of woven fabric such as yarn slippage, yarn unraveling and yarn crimp are lost with this modeling approach.

Gu [15] explicitly modeled the fabric at the yarn level resolution. The cross section of an actual Twaron® fabric, shown in Figure 1-8, is studied using Quester 3-D video microscopy and the yarn crimp wave is modeled mathematically as a sinusoidal equation. Several such yarns were then assembled to form the fabric geometry as shown in Figure 1-9. Utilizing the symmetry, only a quarter model was used for the analysis. The impact analysis was carried out using LS-DYNA.

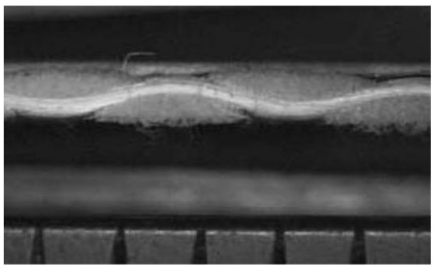

Figure 1-8 Twaron® plain weave fabric cross-section [15]

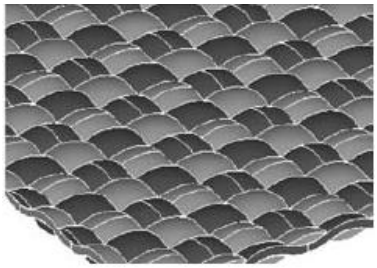

Figure 1-9 Twaron® fabric geometry model [15]

Though the explicit modeling of yarns is computationally expensive than that based on simplified models, it allows for the inclusion of physical phenomena such as yarn-yarn interaction, yarn crimp and yarn pull-out.

Rao et al. [16] developed a local/global modeling approach in order to capture the yarn-to-yarn interactions in detail. Modeling the entire fabric patch in detail not only tends to be computationally expensive but also is redundant as the yarns in the regions far away from impact zone are almost intact during the impact. The local/global modeling approach solves this issue by combining the detailed modeling of undulating yarns and a homogeneous continuum in which there is no discrete modeling of individual yarns. The regions that retain undulating yarn descriptions are termed ‘local’

and the region that consists of the homogenized continua is termed ‘global’. The fundamental idea of this approach is illustrated in Figure 1-10.

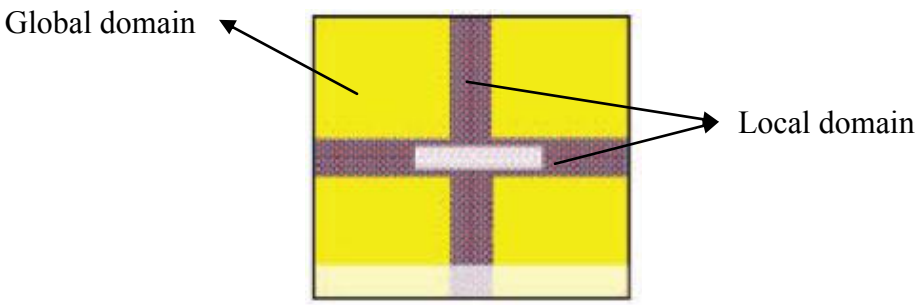

Figure 1-10 Global and local solution domain [16]

The solution domain in this case incorporates two necessary conditions. Firstly, the areal density of fabric is consistent throughout the domain. Secondly, the transverse wave propagates with the same velocity across the solution domain. This approach reduced the computational time by about 50% without losing the essential physics of the problem.

Shahkarami et al. [17] developed a new computational approach to predict the impact behavior of Kevlar® fabrics based on the individual response of the smallest repeating unit in the fabric panel. Such a repeating unit is also called a representative volume element (RVE). The fundamental approach is to study the interactions between the yarn crossovers for a single unit, which essentially give rise to a bi-axial response of the fabric. The underlying objective is to obtain the membrane response of a fabric unit cell and smear the properties onto a single representative shell element. Finally, a full scale model of the fabric panel is constructed using these shell elements.

Using the yarn geometry parameters (such as the cross section profile) and dimensions and fabric properties (such as the yarn count, yarn crimp in warp and weft directions), a 3D yarn crossover was built, as shown in Figure 1-11.

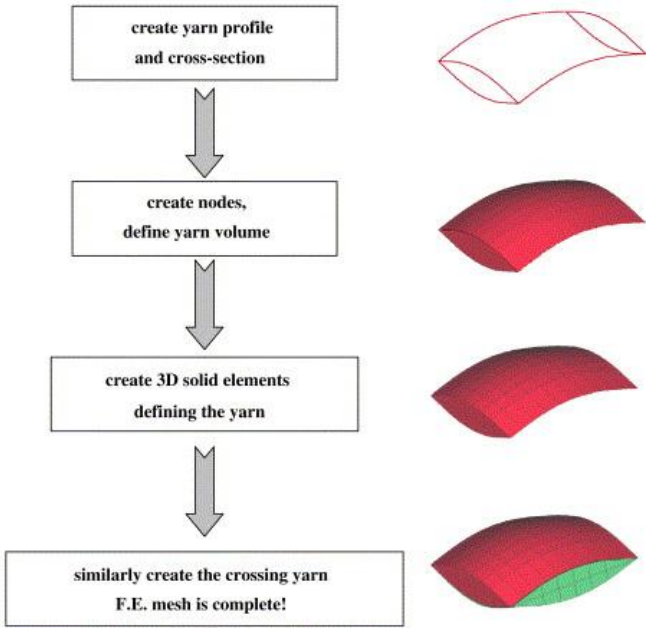

Figure 1-11 3D Single yarn crossover [17]

The main drawback of this model is that the yarn slippage and inter-yarn friction were not taken into account, though the model proved to be effective in predicting the impact response of the Kevlar® 129 plain weave fabric considered in this study. This discrete continuum shell model provides increased accuracy at reduced computational costs.

A comparison of different compares the different modeling approaches is given in Table 1-1, where advantages and disadvantages of each method are listed.

Table 1-1 Comparison of FE models

Model	Advantages	Limitations
Network of bar elements	1) Fewer degrees of freedom 2) Simpler geometry	1) No control on yarn crimp 2) Yarn-yarn interaction
Membrane approximation	1) Good agreement with the transverse displacement profile 2) Simple geometry	1) Plane stress assumption 2) Not replicating the woven architecture 3) Friction between yarns not considered
Explicit modeling of yarns	1) Accounting for yarn-yarn interaction	1) Computationally expensive
Global/local approach	1) Undulations in the far-field domain neglected 2) Detailed 3D model of yarns only along principal yarns 3) Minimized computational time	1) Rate dependent behavior of yarns neglected.

The first step to model the behavior of any system is to make sure that the model does not violate the physics of the process. To understand the impact phenomenon, the following sub-section briefly explains the mechanics of penetration in woven fabrics.

1.5 Penetration mechanics

Impact mechanics spans a wide variety of problems involving collisions of two bodies. The collision of a rigid or deformable body onto another body fixed in space can be described as a projectile-target impact. When a projectile impinges on a target, at each instant during the impact the contact pressure acts on the two bodies resisting interpenetration. This contact pressure causes local deformations which vary according to the velocity of impact and the material properties of the two bodies. Though the effect of contact pressure is different on the target and the projectile, the stress-continuity constraint has to be satisfied at the projectile-target interface.

The target can be considered as thin or thick depending on the ratio of the target thickness to the projectile diameter. If this ratio is greater than 5, the target is considered to be thick and in this case the steady state effects dominate [18]. However for thin targets, transient effects due to initial impact dominate. Fabric targets, such as the Twaron CT709® used in the present study are analyzed as thin targets, as the diameter of the projectile is much higher than the thickness of the target.

1.5.1 Penetration and failure in fabric targets

Impact into fabrics is a complex process involving the interaction of a large number of variables such as the fabric structure, shape and size of the impacting projectile. Several models have been proposed identifying the major control variables. Smith et al. [19] explains the impact on a single yarn. Figure 1-12 shows the transverse impact into a single yarn.

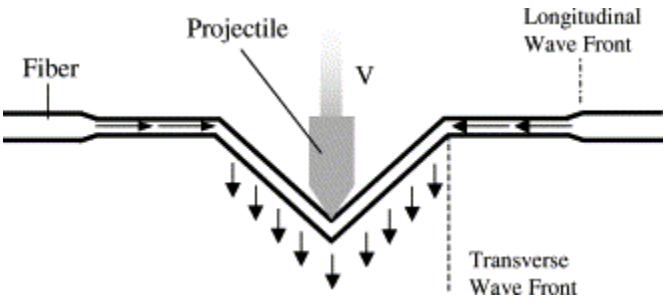

Figure 1-12 Transverse impact on single yarn [20]

At the time of impact two stress waves originate from the impact point, namely longitudinal and transverse. The longitudinal wave travels along the axis of the yarn at the speed of sound. The tensile wave as shown in the Figure 1-12 propagates away from the point of impact causing the material behind the wave front to flow towards the impact point, which has now moved along with the projectile. However, this model is not adequate for describing what happens in an actual fabric due to the complex stress wave interaction at the yarn crossovers.

In an actual fabric, the projectile causes the principal yarns (i.e., yarns in direct contact with the projectile during the impact) to deflect in the transverse direction, as schematically shown in Figure 1-13.

Figure 1-13 Top and side view of fabric just after the impact [21]

As the transverse wave progresses, yarns orthogonal to the principal yarns are also pulled towards the impact point by the principal yarns. Such yarn-yarn interactions produce non orthogonal movement or bowing of yarns towards the impact point, as shown in Figure 1-14.

Figure 1-14 Top and side view showing the transverse wave propagation [21]

Roylance and Wang [22] studied the effect of stress wave interactions at yarn crossovers using a numerical analysis. They idealized the woven fabric as an assembly of pin-jointed elements of certain mass, with the areal mass density of the mesh equal to that of the fabric panel under consideration.

The initial velocity of impact is imposed on the node at impact point as shown. Using finite difference equations, the impulse-momentum equations are solved at each crossover point and stresses and strains are evaluated at each time step.

Since there is no external force acting on the projectile-fabric system, the total energy of the system is conserved. The loss in kinetic energy of the projectile, ΔKE, can be written as

$$\Delta KE = \frac{1}{2} M_P (v_i^2 - v_r^2), \tag{1.1}$$

where M_P is the mass of the projectile, and v_i and v_r are the impact velocity and residual velocity of the projectile, respectively. This energy is dissipated in many forms. Some of the mechanisms of energy loss are:

(a) Strain energy gain by the fabric;

(b) Kinetic energy of the fabric yarns;

(c) Frictional dissipation due to sliding;

(d) Projectile deformation energy;

(e) Friction within the yarn (inter fibril friction);

(f) Heat and acoustic losses.

The fabric strain energy and kinetic energy together with the frictional dissipation constitute the majority of the energy absorbed. The other losses are assumed to be negligible. Therefore, the energy transfer between the fabric and projectile can be expressed as

$$\Delta KE = SE + KE_f + E_f, \tag{1.2}$$

where SE is the fabric strain energy, KE_f is the fabric kinetic energy, and E_f is the frictional dissipation.

1.5.2 Fabric failure mechanisms

As described earlier, the transverse wave originating at the impact point causes transverse deflection in the yarns near the impact point. This transverse deflection proceeds until the strains in the yarns reaches the breaking strain. Ballistic fibers possess high tensile strengths and can absorb considerable energy before failure. Experiments performed by Shockey et al. [23] showed that there are four distinct fabric failure modes: breakage of bonds, local yarn rupture, remote yarn failure, and yarn pull-out.

Shim et al. [24] observed that breakage of bonds in PPTA fibers such as Twaron® occurs when stress for a particular failure mode is reached, which triggers the fracture initiation. He observed that at low strain rates plastic deformation and intermolecular slippage occur, resulting in failure of secondary hydrogen bonds in preference to primary C-C bond breakage. However at high strain rates both Shim et al. [24] and Termonia et al. [25] observed that primary bond breakage or brittle fracture is predominant, since at

high strain rates the time for which the bond is under a particular stress level is very short.

Local yarn rupture is the most common failure mode which occurs at the impact point. It is usually followed by a sudden drop in load when all the fibrils in the yarn break apart at once. The two main causes of yarn rupture are yarn stretching and shearing of yarns across other yarns.

Remote yarn failure occurs at regions away from the impact point due to the increased tensile load acting on the yarns after the impact. Yarn pull-out does not damage the yarn but instead, the yarn at the ungripped edges is pulled loose from the fabric by the moving projectile. Generally, it is observed that failure takes place due to the axial tensile failure of yarns.

For Twaron®, numerous experimental studies have shown strong strain-rate dependant behavior. It was observed that as the strain rate increases, the tensile strength and Young's modulus increase, whereas the failure strain decreases. The failure is more in a brittle manner as the strain rate increases.

Shim et al. [24] performed dynamic tensile tests on Twaron® and observed that the failure strain is dependent on the applied strain rate. At low strain rates of the order of $\dot{\varepsilon} < 400s^{-1}$, the failure strain is much higher than that at high strain rates. Using the dynamic stress-strain curves from experiments, two different failure strain expressions were proposed in Shim et al. [24].

$$\begin{aligned} \varepsilon_f &= 0.04383 - 0.0108\,\dot{\varepsilon}/\dot{\varepsilon}_o\,, && 100s^{-1} < \dot{\varepsilon} < 410s^{-1} \\ &= 0.0192\left[1 + exp\left(-11.8(\dot{\varepsilon}/\dot{\varepsilon}_o - 0.9725)\right)\right], && 410\mathrm{s}^{-1} < \dot{\varepsilon} < 600\ \mathrm{s}^{-1} \end{aligned} \tag{1.3}$$

Gu [15] obtained the mechanical properties of Twaron® at different strain rates as shown in Table 1-2.

Table 1-2 Dynamic mechanical properties of Twaron® [15]

Strain rate(s^{-1})	E(GPa)	σ_{max} (GPa)	ε_{max} (GPa)
10^{-2}	62	2.395	5.19
180	69	2.596	5.22
480	70	2.704	5.47
1000	72	2.753	5.70

The complexity of the phenomenon associated with the impact process has resulted in wide spread applications of numerical methods such as FEA to understand the ballistic behavior. Commercially available FE codes have excellent capabilities to analyze high velocity impact dynamics. Explicit and Implicit solution techniques are used as the basis for such FE codes. The basic theory and formulation of the finite element analysis is discussed in the next sub-section.

1.6 Introduction to FE method

Finite element (FE) method is a popular numerical technique used to find approximate solutions by solving the reduced forms of partial differential equations and integral equations using standard techniques such as Runge- Kutta method and Euler method over complex solution domains.

Commercial FE software packages currently available have enhanced capabilities of analyzing complex engineering problems. Some of the commercially available FEA solvers are ABAQUS, ANSYS, LS-DYNA, COSMOS, and NASTRAN. The present study is carried out using the explicit dynamic FE solver ABAQUS/Explicit. In this sub-section, the principal development of FE equations is discussed next.

1.6.1 Theory of FE method

Solving for the displacements, stresses or forces for a solid body subjected to loading over a period of time requires setting up equations of equilibrium at all time instants over an infinitesimal volume of the body. This is simplified further to a weaker requirement that the equilibrium be maintained in an average sense over a finite number of discrete elements in the volume of the body. The derivation of the equilibrium in the form of a virtual work statement is discussed and the approximate algebraic equations for the equilibrium will be reviewed below [26].

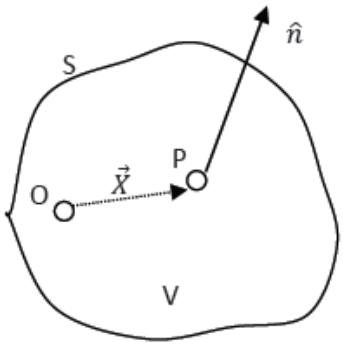

Figure 1-15 Material volume under consideration

Let V be the volume of the body under consideration and S be the surface bounding this volume as shown in Figure 1-15. V is the volume occupied by the material at the current time instant. This material definition refers to the Lagrangian approach. In this approach the coordinate system moves with the material. In the Eulerian approach, on the other hand, the volume remains fixed in space and the material flows through it. The only disadvantage of using the Lagrangian approach is that it can cause excessive distortion and hence need much smaller time steps. This can be however avoided by using a suitable element deletion criterion.

Let **t** be the surface traction at any point on the surface S and **f**, the body force at a point in the material volume. Balancing the forces gives

$$\int_S \mathbf{t} dS + \int_V \mathbf{f} dV = 0. \tag{1.4}$$

Define **n** as the unit normal vector on the surface S at the point P under consideration. The Cauchy stress or the true stress at any point is given by

$$\mathbf{t} = \boldsymbol{\sigma}\mathbf{n}, \tag{1.5}$$

Using divergence theorem, the surface integral can be rewritten as a volume integral as

$$\int_S \boldsymbol{\sigma}\mathbf{n}\mathrm{d}S = \int_V \mathrm{Div}\boldsymbol{\sigma}\mathrm{d}V \tag{1.6}$$

Substituting Eq. (1.6) into Eq. (1.4) and integrating will give

$$\mathrm{Div}\boldsymbol{\sigma} + \mathbf{f} = \mathbf{0}, \tag{1.7}$$

which gives the familiar force equilibrium equations in 3D.

The moment equilibrium is established by taking the moment balance about the origin. We get

$$\int_S (\mathbf{X} \times \mathbf{t})\mathrm{d}S + \int_V (\mathbf{X} \times \mathbf{f})\mathrm{d}V = \mathbf{0}. \tag{1.8}$$

Applying the divergence theorem gives

$$\boldsymbol{\sigma} = \boldsymbol{\sigma}^{\mathbf{T}}. \tag{1.9}$$

This shows that a symmetric stress matrix automatically satisfies the moment equilibrium equations.

Ultimately, the aim is to develop local spatial approximation of displacement for parts of the solution. Such an approximation calls for a weak form of Eq. (1.7).

The weak form is obtained by first multiplying point-wise differential equations by an arbitrary vector known as ‘test function’ having continuity over the entire volume and then integrating.

The use of an arbitrary test function helps in recovering the differential equilibrium statement at any point by making the test function zero only at that point. This equivalent 'weak form' consisting of a general stress matrix is known as the virtual work principle. The test function can be assumed to be an arbitrary continuous 'virtual' velocity field, δV, obeying all the prescribed kinematic constraints. The dot product of this equation with the equilibrium equation gives the 'virtual' rate of work.

Taking the dot product of Eq. (1.7) with δV gives a single scalar equation at each at each material point, which is then integrated over the entire volume as follows:

$$\left(\frac{\partial \sigma_{ij}}{\partial X_j} + f_i\right) \delta v_i = 0. \tag{1.10}$$

Applying the product rule gives

$$\left[\frac{\partial}{\partial X_j}\left(\sigma_{ij}\, \delta v_i\right) - \sigma_{ij}\, \frac{\partial \delta v_i}{\partial X_j}\right] + f_i \delta v_i = 0 \tag{1.11}$$

Note that

$$\int_V \sigma_{ij\,,j}\; \delta v_i dV = \int_V \left[\left(\sigma_{ij}\, \delta v_i\right)_{,j} - \sigma_{ij}\, (\delta v_i)_{,j}\; \right] dV\,, \tag{1.12}$$

Applying the Divergence theorem to the first term in Eq. (3.9) leads to

$$\int_V \left(\sigma_{ij}\, \delta v_i\right)_{,j}\; dV = \int_S \sigma_{ij}\; \delta v_i n_j\, ds = \int_S \mathbf{t} \cdot \delta \boldsymbol{v} dS$$

Using these, Eq. (1.11) can be rewritten as

$$\int_S \mathbf{t} \cdot \delta \boldsymbol{v} dS + \int_V \mathbf{f} \cdot \delta \boldsymbol{v} dS = \int_V \sigma : \left(\frac{\partial \delta \boldsymbol{v}}{\partial \mathbf{X}}\right) dV \tag{1.13}$$

The next step in the FE method is to discretize the body. This is done by discretizing the body approximated as a continuum into smaller elements and nodes. As a result differential equations governing the deformation of the continuum are replaced by algebraic equations, which are finally assembled for all elements in the domain. The displacement field is approximated with finite terms and is interpolated between nodes to obtain an approximate solution. This implies that a finer mesh leads to a more precise solution.

The equation system in an FE analysis can be expressed as [26]

$$[\mathrm{M}]\{\ddot{\mathbf{u}}\} + [\mathrm{K}]\{\mathbf{u}\} = \mathbf{F}(\mathrm{t}, \mathbf{u}) \qquad (1.14)$$

where $[\mathrm{M}]$ is the mass matrix, $[\mathrm{K}]$ is the stiffness matrix , $\mathbf{u}$ is the displacement vector, and $\mathbf{F}$ is the applied load vector. This system of algebraic equations can be solved for displacements.

The manner in which displacements and accelerations are evaluated at each node leads to an Implicit or an Explicit formulation. In an implicit method the global stiffness matrix on the left hand side of the equation system remains in all equations after substituting the nodal displacements and accelerations. This requires solving a system of equations at each time step and store the stiffness matrix. For a static analysis, the stiffness matrix remains constant, but for dynamic analyses involving non- linearity, the stiffness matrix needs to be updated at each and every time step. One advantage of an implicit method is the control on time step size, which can be selected by the user. An Explicit solution, on the other hand, is stable only when Δt is smaller than the critical step size Δt_{cr} , which is equal to L_s/C_d , where L_s is the element characteristic length

and C_d is the current dilatational wave speed that is dependent on the worst element in the mesh.

The main advantage of an explicit method is that it requires shifting of the stiffness matrix to the right-hand side of equation system, thereby foregoing the necessity to invert stiffness matrix at each time step. Even though explicit methods require a large number of increments, the net computational cost is low owing to the efficiency of each increment, as there it is not necessary to form and store the stiffness and mass matrices at each time step.

1.6.2 Explicit time integration

The equations of motion in an explicit formulation are solved by using a central difference rule. That is, the nodal displacement values of the next time step are determined from the previous time step [26].

The acceleration and displacement can be expressed as

$$\dot{u}^{(i+1/2)} = \dot{u}^{(i-1/2)} + \frac{\Delta t^{i+1} + \Delta t^{i}}{2} \ddot{u}^{(i)} , \tag{1.15}$$

$$\dot{u}^{(i+1)} = \dot{u}^{(i)} + \frac{\Delta t^{i+1}}{2} \dot{u}^{(i+1/2)} , \tag{1.16}$$

where i denotes the increment number, and $(i - 1/2)$ and $(i + 1/2)$ represent the mid-increment values.

The computational efficiency arises due to the use of diagonal element mass matrices, as the inversion of the mass matrix used in the computation for accelerations at the beginning of each increment becomes trivial:

$$\dot{u}^{(i)} = [\mathrm{M}]^{-1} \cdot \left\{ \mathrm{F}^{(i)} - \mathrm{I}^{(i)} \right\}. \tag{1.17}$$

where M is the diagonal lumped mass matrix, I is the internal force vector.

The mean velocities $\dot{u}^{(i+1/2)}$ and $\dot{u}^{(i-1/2)}$ are defined in a specific way for initial conditions and the presentation of results. The velocity at each time step is stored as a linear interpolation of mean velocities, i.e.,

$$\dot{u}^{(i+1)} = \dot{u}^{(i+1/2)} + \frac{\Delta t^{i+1}}{2} \ddot{u}^{(i+1)}. \tag{1.18}$$

To start the calculations, $\dot{u}^{(i-1/2)}$ has to be defined. At t=0, the initial values of velocity and acceleration are set to zero unless user-defined values are specified, which gives

$$\dot{u}^{(+1/2)} = \dot{u}^{(0)} + \frac{\Delta t^{1}}{2} \ddot{u}^{(0)}. \tag{1.19}$$

Substituting into expression for $\dot{u}^{(+1/2)}$ leads to

$$\dot{u}^{(-1/2)} = \dot{u}^{(0)} - \frac{\Delta t^{0}}{2} \ddot{u}^{(0)}. \tag{1.20}$$

The solution procedure can be summarized as follows:

Step1 At each time step *t*, the dynamic equilibrium Eq. (1.17) is solved to calculate the nodal accelerations

Step2 By integrating these accelerations nodal velocities and displacements are calculated by using the central difference scheme as mentioned in equations above.

Step3 By using the strain increment $\mathbf{d\varepsilon}$ calculated from the strain rate $\dot{\varepsilon}$, element strains are updated.

Step 4 The stresses are then updated for the time step using the material constitutive relation $\sigma_{t+\Delta t} = \sigma_t + \Delta\sigma(\sigma_t, d\varepsilon)$.

Step 5 Internal forces $I_{t+\Delta t}$ are calculated from adjacent elements for the next time step

Step 6 Replace $t + \Delta t$ with t for the current step and then return to *step 1.*

The time step size is automatically chosen by ABAQUS/Explicit without necessary user intervention. The critical maximum time increment depends on the elements with the smallest maximum time increment.

2. FINITE ELEMENT MODEL OF BALLISTIC IMPACT

To save computational effort and time, only a quarter of the fabric projectile model is analyzed due to the symmetry of the problem.

2.1 Geometry models of Plain weave Twaron® fabric and projectile

The geometric properties of Twaron CT709® fabrics are listed in Table 2-1. A comparison with more widely used Kevlar fabrics indicates that the Twaron CT709® fabric is approximately two times lighter than a Kevlar 29® fabric.

Table 2-1 Fabric properties [27,28,29,30,31]

Properties	**Kevlar®**	**Twaron CT709®**
Physical		
Density(kg/m^3)	1440	1440
Areal density(g/m^2)	475	202
Denier	3000	837
Yarn thickness, h(mm)	0.79	0.15
Yarn width, b(mm)	1.49	0.952
Warp count (yarns/inch)	17.78(0.7 yarn/mm)	27(1.06 yarn/mm)
Weft count(yarns/inch)	17.78(0.7 yarn/mm)	27(1.06 yarn/mm)
Fabric area(mm/mm)	100×100	100×100

The plain weave fabric for the current study is modeled with a yarn level resolution. Each individual yarn is treated as a continuum. The first step is to model a single yarn and then assemble the yarns to obtain the plain weave characteristics. Gu [15] obtained the following equation for the yarn crimp wave shown in Figure 2-1 by sampling and plotting points from the fabric photographed with Quester 3D video microscopy.

$$y = 0.017\, sin\left(\pi \frac{x - 0.744}{0.151}\right) \tag{2.1}$$

Figure 2-1 Yarn crimp wave

The 3D model using this equation, however, had many over-closures (interpenetrating volumes) which cause erroneous contact behavior in the FE calculations presented in Gu [15].

The geometry used for the loosely woven plain weave fabric in the current study is described below. Figure 2-2 shows a repeating unit in a plain weave fabric, which is also called an RVE or a unit cell.

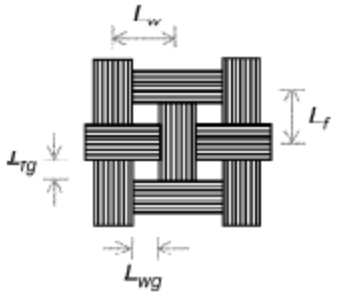

Figure 2-2 Unit cell of a loosely woven plain weave fabric [32]

In this unit cell, the yarn crimp is achieved by a combination of circular arcs and straight lines and the yarn cross section is assumed to be of lenticular shape, as shown in Figure 2-3.

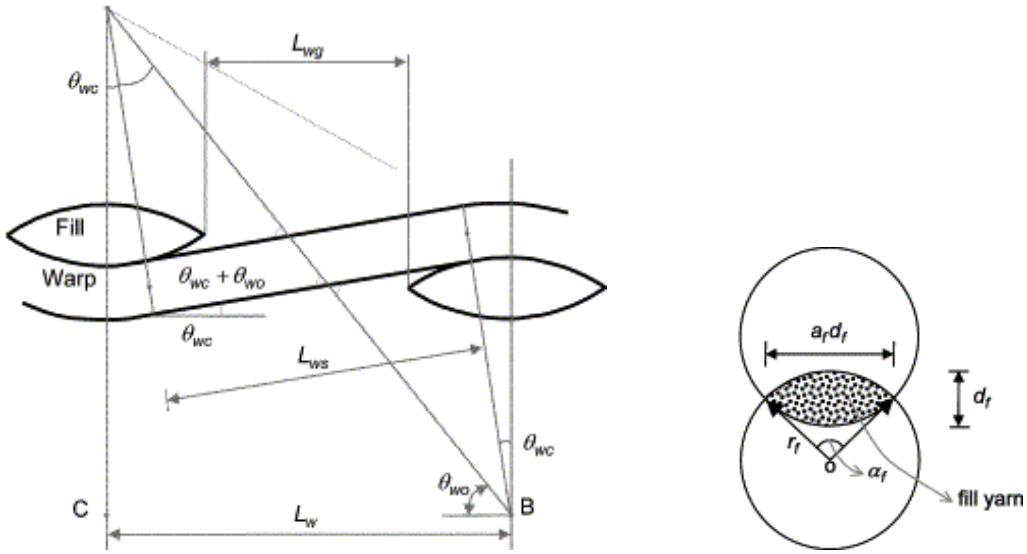

(a) (b)

Figure 2-3 (a) Geometric model of yarn crimp and (b) yarn cross section [32]

In Figure 2-3,d_w, d_f= thickness/ height of the warp and fill yarn respectively.

a_f = shape factor of the fill yarn cross section.

α_f = the chord angle of the lenticular shape

r_f = radius of the cross section

L_w = yarn to yarn distance

L_{wg} =gap length

L_{ws} = straight part of the yarn

θ_{wc} =crimp angle

These parameters are evaluated for Twaron® employing the properties in Table 2-1 and the yarn model is generated using ABAQUS/CAE. Figure 2-4 shows the 3D yarn model to be analyzed in the current study.

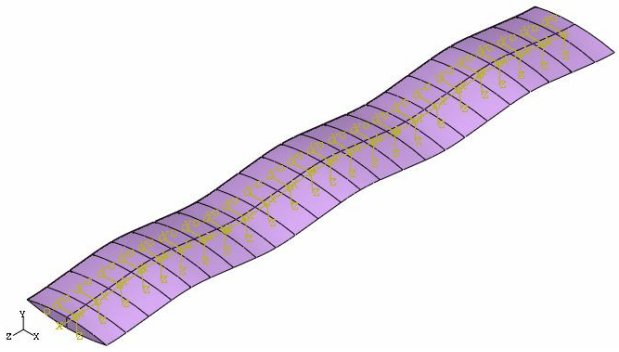

Figure 2-4 3D yarn model

A number of referential local material coordinates have been specified along the yarn axis to account for the yarn crimp behavior in the FE analysis. Upon loading, the

yarn first undergoes decrimping or straightening out before any strain is produced. This behavior can be replicated by using numerous local material orientations along the axis, as shown in Figure 2-5.

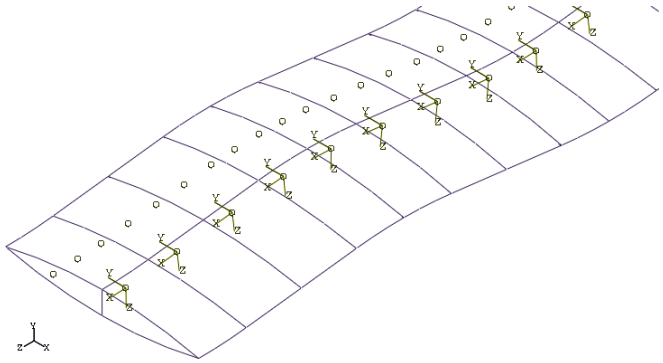

Figure 2-5 Spatially varying material coordinates

The yarns are finally assembled to form the required loosely woven plain weave fabric geometry shown in Figure 2-6.

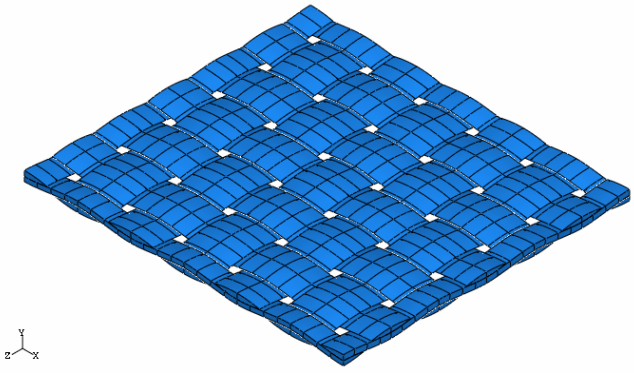

Figure 2-6 Plain weave Twaron® fabric 3D geometry: quarter model

Three projectile shapes are considered in the present simulations: cylindrical, hemi-spherical and spherical. The bullets are modeled as rigid shells. The geometry and the 3D model generated using ABAQUS/CAE for each projectile shape is shown in Figure 2-7.

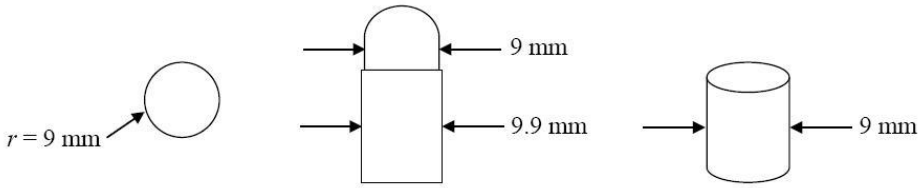

(a)

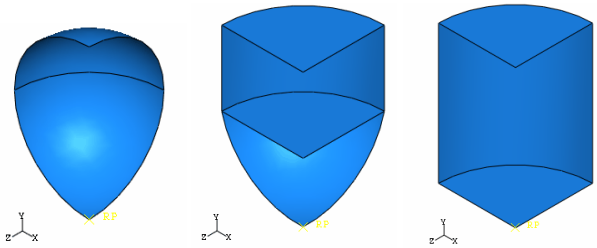

(b)

Figure 2-7 (a) Geometry properties and (b) quarter models of the bullets

The projectile fabric system is shown in Figure 2-8. The outer two edges away from the impact point are fixed, and for the remaining two edges symmetry conditions are applied. The fabric is in the x-z plane, with negative y axis as the impact direction.

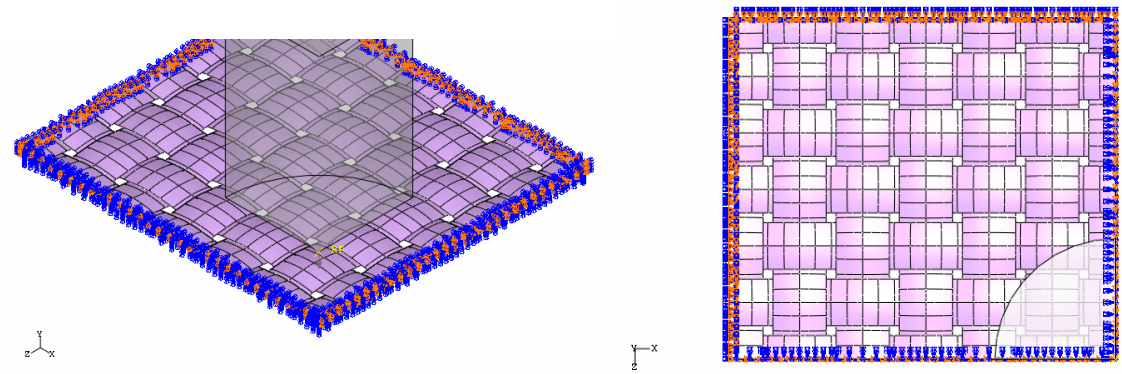

(a) Isometric view (b) Top view

Figure 2-8 Fabric-projectile system: FE model

2.2 Materials for Twaron® and projectile

The material behavior for the Twaron® fabric is incorporated into the analysis by using a user subroutine VUMAT discussed in detail in the next section. Since the present study deals with only high velocity impacts, the failure is essentially brittle, i.e., there is no significant plastic deformation due to the very short loading times. In the finite element model, the failure of yarn is assumed to arise from tensile failure when the maximum effective stress (von Mises) reaches the failure stress of 3.6 GPa. This maximum stress failure criterion is used for deleting elements from the mesh. The material properties for a single Twaron yarn are tabulated in Table 2-2.

Table 2-2 Twaron CT709® yarn mechanical properties

Mechanical properties	Twaron CT709®
Tensile modulus(GPa)	90
Tensile strength(GPa)	3.6
Failure strain in tension (%)	4.0
Poisson's ratio	0.3

The projectile is defined as a rigid shell and is made of steel of density 7.8 g/cm^3.

2.3 Contact between the fabric and projectile

The contact formulation should include the contact between the projectile and fabric, contact between the warp and weft yarns and contact between the fabric layers. A finite sliding global contact search algorithm is used.

The friction coefficient between the projectile and fabric and between the yarns is assumed to be 0.3. The inter-layer dynamic friction coefficient is 0.01 [15].

Due to the large number of contacts between the weft and warp yarns, choosing a master surface and a slave surface individually is highly complicated. The global contact search algorithm in ABAQUS/Explicit is equipped with capabilities for tracking the master and slave surfaces. This contact algorithm is robust and computationally efficient for complex contact problems.

The global contact search algorithm uses a bucket sorting algorithm, as shown in Figure 2-9.

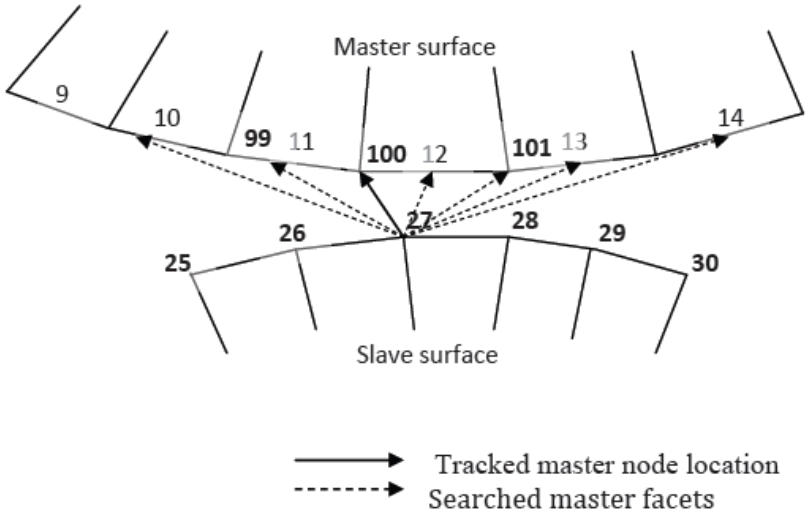

Figure 2-9 Global contact search

Based on Figure 2-9, the procedure can be summarized as following [33]:

Step 1 Consider a node numbered 27. The global search algorithm calculates the distance to node 27 from all the master surface facets in the same bucket as node 27.

Step 2 The nearest node is determined on the master surface. In this case it is the facet of element 12.

Step 3 In element 12, the node nearest to node 27, which is node 100, is made the tracked master surface node.

Step 4 Step 1 is repeated for all slave nodes against all facets of the master surface that are in the same bucket as the node.

Since the search is conducted for each slave node in the computational domain, the global searches are computationally expensive. However, in the present model, due to the complexity of the surfaces in contact, this contact algorithm is best suitable.

2.4 Meshing scheme of the fabric and the projectile

Each yarn in the fabric is meshed using 8-node solid brick elements with reduced integration and hour glassing (C3D8R) in ABAQUS. Reduced integration can be used for 3D hexahedral elements with many advantages. This is because in ABAQUS numerical integration is done by replacing the virtual work integral with a summation in the form [26]:

$$\int_V \boldsymbol{\sigma} : \delta \boldsymbol{D}\, dV = \sum_{i=1}^{n} \sigma_i : \delta D_i V_i \tag{2.2}$$

where n is the number of integration points, and V_i is the volume associated with the integration point i. Since the present analysis involves a large number of elements, using reduced integration can reduce the computational time & storage requirements.

The cross section of each yarn is meshed with 42 C3D8R elements in ABAQUS using the structured mesh technique as shown in Figure 2-10.

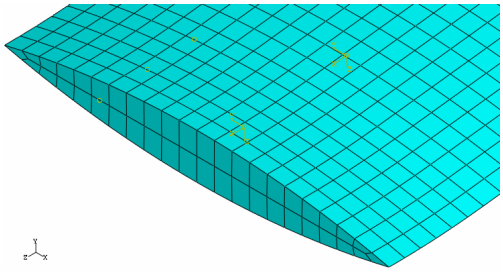

Figure 2-10 Yarn mesh

Structured meshing is used for models which have a complex geometry but contain faces with relatively simple geometry. In each case the cross section of the yarn is first patterned with rectangular faces and is then mapped over the entire length.

The bullet is modeled using linear quadrilateral R3D4 elements in ABAQUS, which are 3D, 4-node rigid elements. The fabric and bullet mesh are shown in Figure 2-11.

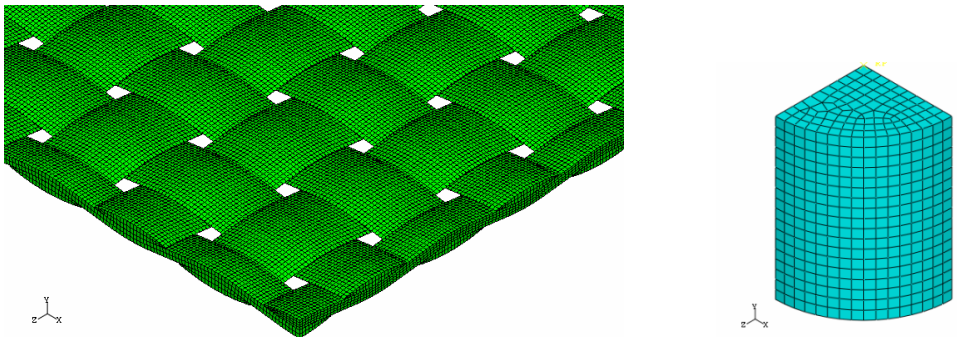

(a) (b)

Figure 2-11 (a) fabric mesh and (b) bullet mesh

In the next section the material behavior of the Twaron fabric will be presented in detail together with its definition in ABAQUS.

3. DEFINITION OF TWARON® MATERIAL BEHAVIOR

3.1 Viscoelastic behavior

Ballistic fibers such as TWARON® typically show viscoelastic material behavior that is highly dependent on the imposed strain rate. The work of Roylance et al. [22] illustrated that the viscoelastic relaxation gives rise to a slower transverse shock wave propagation. They also demonstrated that this rate-dependent non-linear behavior can be represented by linear viscoelastic models.

Termonia and Smith [25] proposed a model of highly oriented polymeric fibers, as shown in Figure 3-1, which can explain the material behavior linked to the polymer molecular structure.

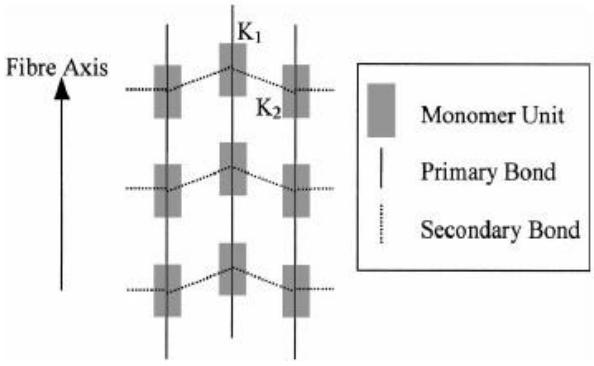

Figure 3-1 Termonia and Smith's polymer model [25]

Twaron® is a *p*-phenylene terephtalamide (PPTA). When subjected to tensile load part of the strain comes from the elongation of polymer chains, and another part from the relative displacement between individual chains. Bicerano [33] proposed that

this molecular arrangement can be viewed as a particular arrangement of springs. The intramolecular C-C bonds in the polymer chains, which are covalent in nature, can be viewed as a spring with certain stiffness. Such covalent bonds are called primary bonds. Similarly, the intermolecular bonds which arise due to attraction between chains, such as the Vander Waals forces and hydrogen bonds, can be associated with a spring of a certain stiffness constant. Such intermolecular attractions which are comparatively weaker are termed as the secondary bonds. These molecular deformation mechanisms can be accurately described by the three element model as shown in Figure 3-2 using springs and dashpots. This is known as the generalized Kevin-Voigt (GKV) model.

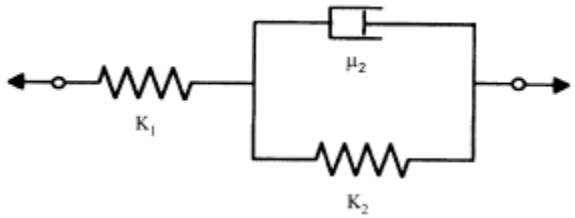

Figure 3-2 Three element spring-dashpot model (GKV model)

The behavior of the primary bonds can be represented by a spring of stiffness constant k_1 and that of the secondary bonds by k_2. k_1 is higher than k_2, as the primary bonds which are covalent are much stiffer than the secondary hydrogen bonds. The sliding of chains relative to each other can be represented by the viscoelastic constant μ_2.

It can be observed that at low strain rates, both springs extend under tensile load. As the stiffness of k_2 is lower than k_1 , the spring with stiffness k_2 fails sooner. This captures the intermolecular slip at low strain rates. At high strain rates, the dashpot

prevents the extension of the spring with stiffness k_2 , resulting in early failure of the spring with stiffness k_1 . This represents the brittle fracture which occurs at high strain rates. In this case, mainly the primary bonds are fractured.

The proposed three-element model by Shim et al.[24] provides an accurate 1-D, small-strain linear viscoelastic description of the material behavior of Twaron® fibers.

The stress-strain relation can be represented by Eq. (3.1) for the GKV model shown in Fig.3-2 as:

$$(1 + k_1/k_2)\sigma + (\mu_2/k_1)\dot{\sigma} = k_2\varepsilon + \mu_2\dot{\varepsilon} \ , \qquad (3.1)$$

where dot denotes the first-order derivative with respect to time. Utilizing the 1D construction, a 3D finite deformation viscoelastic model is provided below, which accounts for the typical behavior of polymeric materials such as stress relaxation, strain-rate dependence and creep. Such 3D models can be utilized to model polymer materials under a wide range of loading conditions.

3.2 Constitutive modeling: 3D linear viscoelastic model

Linear viscoelasticity accounts for the small deformation behavior. The responses of polymeric fibers such as Twaron® can be described well with the classical theory of viscoelasticity, which include creep and stress relaxation. Linear viscoelastic constitutive models are of two distinct types: integral forms and differential forms. Integral forms provide the stress (or strain) as a function of time integral of the strain (or stress rate) multiplied by a material function, which is the stress relaxation or creep function. On the other hand, differential forms are ordinary differential equations in

time, which relate the stress and strain with their rates. Such a model can be represented by a combination of springs and dashpots.

A number of viscoelasticity-based constitutive models exist in the literature, which use springs (representing elastic responses) and dashpots (representing viscous behavior). Just by varying the number of springs and dashpots and their arrangement, different material responses can be described.

The simplest models are the Maxwell model and Voigt model. These models cannot replicate the complicated behavior of polymers which requires generalized models. However, the generalized Maxwell model, as shown in Figure 3-3 and the generalized Voigt model require extensive experiments to determine many material parameters involved.

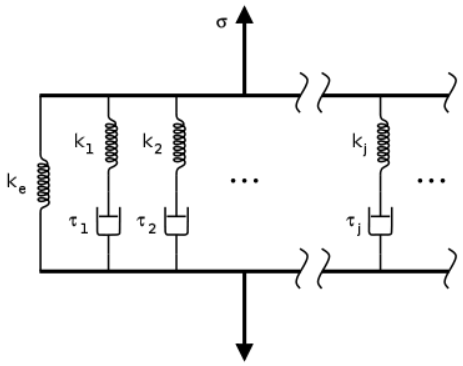

Figure 3-3 Generalized Maxwell model

The standard linear solid model in its Maxwell form is the simplest generalized Maxwell model and is also known as $GM^{n=1}$ model. It consists of a linear spring arranged in parallel with a Maxwell element as shown in Figure 3-4.

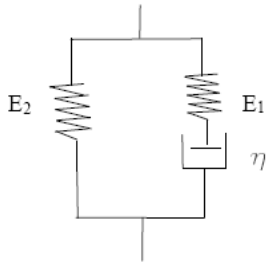

Figure 3-4 Standard linear solid ($GM^{n=1}$)

The mechanical coefficients of the GKV model (Figure 3-2) and the $GM^{n=1}$ (Figure 3-4) model can be used interchangeably using the following conversion formulae.

$$E_2 = k_1^2/k_1 + k_2\,,\ E_1 = k_1k_2/k_1 + k_2,\ \eta = k_1^2\mu_2/(k_1 + k_2)^2 \qquad (3.2)$$

Figure 3-5 depicts the coefficients used in the three-dimensional constitutive equation.

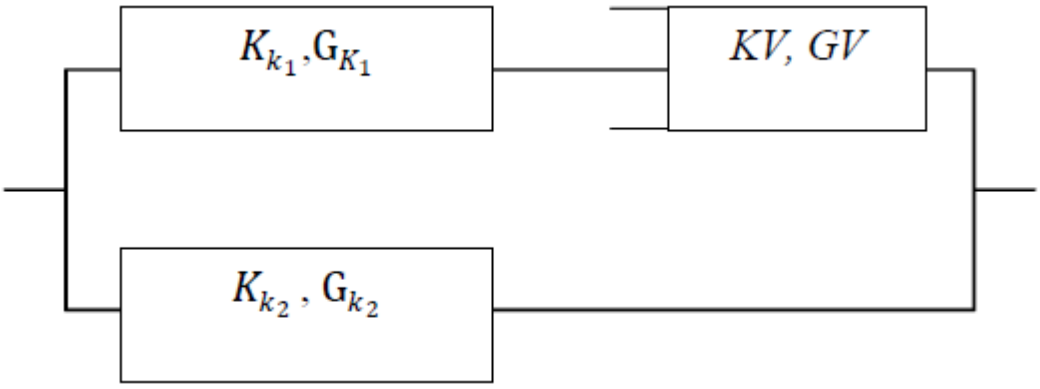

Figure 3-5 Standard linear solid model with different coefficients

The constitutive equation for this model in a 3D setting reads [34]

$$\left(1+\frac{G_{k_2}}{G_{k_1}}\right)\varepsilon_{ij}+\frac{1}{3}\left(\frac{K_{k_2}}{K_{k_1}}-\frac{G_{k_2}}{G_{k_1}}\right)\delta_{ij}\,tr(\dot{\varepsilon})+\frac{G_{k_2}}{GV}\varepsilon_{ij}+\frac{1}{3}\left(\frac{K_{k_2}}{KV}-\frac{G_{k_2}}{GV}\right)\delta_{ij}\,tr(\varepsilon)$$

$$=\frac{\dot{\sigma}_{ij}}{2G_{k_1}}+\frac{1}{3}\left(\frac{1}{3K_{k_1}}-\frac{1}{2G_{k_1}}\right)\delta_{ij}\,tr(\dot{\sigma})+\frac{\sigma_{ij}}{2GV}+\frac{1}{3}\left(\frac{1}{3KV}-\frac{1}{2GV}\right)\delta_{ij}\,tr(\sigma)\,, \qquad (3.3)$$

where *i* and *j* are two free indices each ranging from 1 to 3, δ_{ij} is the Kronecker delta, *G* and *K* denote, respectively, the elastic shear and bulk modulus, and *GV* and *KV* denote the equivalent shear viscosity and bulk viscosity. In addition, the index k_1 denotes the elastic spring in the Maxwellian arm of the model, whereas the index k_2 denotes the elastic spring in the purely elastic arm.

For 1D cases, this equation reduces to [34]

$$\left(1+K_{k_1}/K_{k_2}\right)\dot{\varepsilon}+\left(K_{k_2}/3GV\right)=\dot{\sigma}/K_{k_1}+\sigma/3GV\,. \qquad (3.4)$$

The 3D constitutive equation in (3.3) is used to describe the material behavior of the Twaron CT709® fabric in the present study.

3.3 Implementation of 3D constitutive equation: subroutine VUMAT

The commercial FE software ABAQUS/Explicit® used in the current study has two types of viscoelastic material definitions, including the finite strain viscoelasticity, which is a time domain generalization of either the hyper-elastic or hyper-foam constitutive models. The basic hereditary integral form based on the linear isotropic viscoelasticity is of the form [26]:

$$\sigma(t) = 2G_0 e(t) + \int_0^{\tau} 2\dot{G}(\tau')e(t-t')\,d\tau' + I\left(K_0\varphi(t) + \int_0^{\tau} \dot{K}(\tau')\varphi(t-t')d\tau'\right) \quad (3.5)$$

where τ is the reduced time. K_0 and G_0 are the instantaneous small-strain shear and bulk moduli, and *G(t)* and *K(t)* are the shear and bulk relaxation moduli at instant *t*. These relaxation moduli can be represented in terms of Prony series as

$$G(\tau) = G_0\left(g_\infty + \sum_{i=1}^{N_G} g_i\, exp\left(-\tau/\tau_i^G\right)\right),$$
$$K(\tau) = K_0\left(k_\infty + \sum_{k=1}^{N_k} g_k\, exp(-\tau/\tau_k^K)\right) \quad (3.6)$$

where g_∞ and k_∞ are long term shear and bulk moduli determined from elastic or hyper-elastic properties.

The numerical implementation of a viscoelastic material in ABAQUS is defined by a Prony series expansion of the relaxation modulus as

$$g_R(t) = \left[1 - \sum_{i=1}^{N} \overline{g_i^P}\,(1 - exp\left(-\tau/\tau_i^G\right)\right], \quad (3.7)$$

where *N*, g_i^P, τ_i^G, *(i=1,2….N)* are material constants.

These relaxation parameters can be defined in four ways: specifying the Prony series parameters (g_i^P, k_i^P, τ_i^G) which can be defined directly for each term in the Prony series, input the creep test data, input the relaxation test data, or input the frequency dependent data obtained from sinusoidal oscillation experiments.

The frequency domain definition of viscoelastic behavior describes frequency – dependent material behavior in small steady-state harmonic oscillations for materials in which dissipative losses caused by internal damping effects are modeled in frequency domain. This is not applicable for the Twaron® material behavior. There are many disadvantage of using Prony series to approximate the responses of polymer materials. To get an accurate prediction of material behavior, more than 20 elements are needed which becomes impractical. Hence, the 3D material constitutive model discussed in the previous section is implemented in the subroutine VUMAT of ABAQUS/Explicit®.

The subroutine VUMAT is written in FORTRAN and then linked with the finite element solver to obtain the state of material and mechanical response at each time step for each material calculation point. The flow chart in Figure 3-6 describes the interaction of VUMAT with the FE solver.

The linking between the ABAQUS/Explicit solver and the VUMAT subroutine can be summarized as the following steps:

Step1: ABAQUS provides the strain distributions and user defined state variables to the user subroutine at the beginning of each time step and the constitutive definition in the subroutine then provides the updated stress distribution at the end of each increment to ABAQUS. In the present study, the element deletion status is used as a state variable.

Step 2: In the VUMAT it is necessary to include the variables passed in for information, such as the number of material points, the number of normal and shear components, the number of user defined state variables, and user defined material properties, which are provided as input to the subroutine.

Step 3: The most important task is the definition of the stress increment and value of the state variable at each material point at the end of each increment. The VUMAT then updates the material stress state as well as the user defined state variables at the end of each time increment and return it to the ABAQUS/Explicit® solver. In addition to the stress state, the changes in total internal and inelastic energies are computed and updated to the solver.

Step 4: Material points that reach a user defined failure criterion can be deleted from the model and ABAQUS/Explicit® passes zero stresses and strain increments for all such material points. This can be achieved by specifying a state variable which controls the element deletion. This state variable is initialized to one at the start of the analysis. A value of one indicates that the material point is active. The value of the material deletion state variable can be set to zero in the VUMAT when the material point satisfies a particular failure criterion. A zero value indicates that the material point is deleted from the model by setting the stresses to zero.

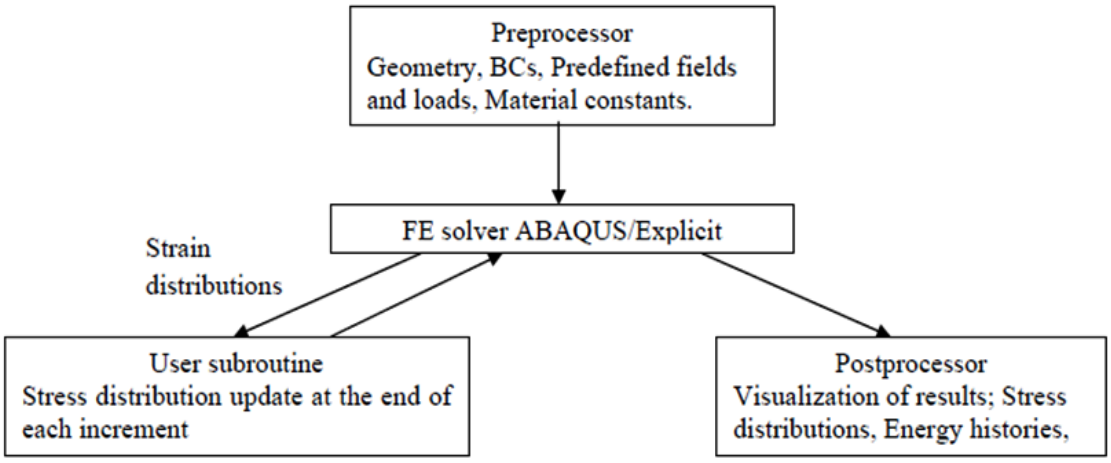

Figure 3-6 VUMAT and FE solver interface

The VUMAT compiled for the present study computes a 3D stress state. The constitutive model is defined in a corotational coordinate system in which the system base rotates with the material. All stresses and strains are computed in the local material coordinate systems. The Green strain measure is used to compute the strains at the end of each increment. This is computationally very convenient as the strain tensor can be directly obtained from the deformation gradients (which are passed by ABAQUS at the beginning of each time step), without solving for the principal directions and can be used for small strains, similar to the case considered in the current study.

Strain measure from the deformation gradient

The deformation gradient maps the position vectors in the initial to deformed configurations. In Figure 3-7 the infinitesimal material vector *dx'* is shown in the

reference configuration. This material vector been stretched and rotated, becoming *dx* in the deformed configuration.

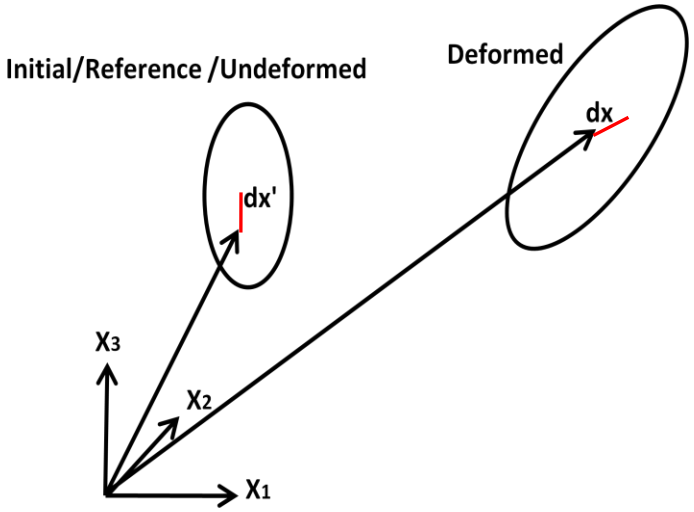

Figure 3-**7** Material vector in reference and deformed configurations

The dx and $dx^{'}$ are related through

$$dx_i = (\partial x_i / \partial x_j^{'})\, dx_j^{'} \,, \tag{3.8}$$

where $F_{ij} \equiv (\partial x_i / \partial x_j^{'})$ is the deformation gradient tensor, which maps the material vector in the undeformed configuration to the deformed configuration. In a matrix form, the deformation gradient tensor can be expressed as

$$F_{ij} = \begin{pmatrix} F_{11} & F_{12} & F_{13} \\ F_{21} & F_{22} & F_{23} \\ F_{31} & F_{32} & F_{33} \end{pmatrix} = \begin{bmatrix} \partial x_1/\partial x_1^{'} & \partial x_1/\partial x_2^{'} & \partial x_1/\partial x_3^{'} \\ \partial x_2/\partial x_1^{'} & \partial x_2/\partial x_2^{'} & \partial x_2/\partial x_3^{'} \\ \partial x_3/\partial x_1^{'} & \partial x_3/\partial x_2^{'} & \partial x_3/\partial x_3^{'} \end{bmatrix}. \tag{3.9}$$

The Lagrangian or Green strain tensor, E_{ij} is defined in terms of strain gradient as

$$E_{ij} = \frac{1}{2}\left(F_{ki}\, F_{kj} - \delta_{ij} \right), \tag{3.10}$$

where δ_{ij} is the Kronecker delta. This equation is utilized to calculate the strain during each time step.

3.4 VUMAT algorithm

The flow chart in Figure 3-8 provides a detailed description of the structure and functionality of the VUMAT coded in FORTRAN developed in the present study.

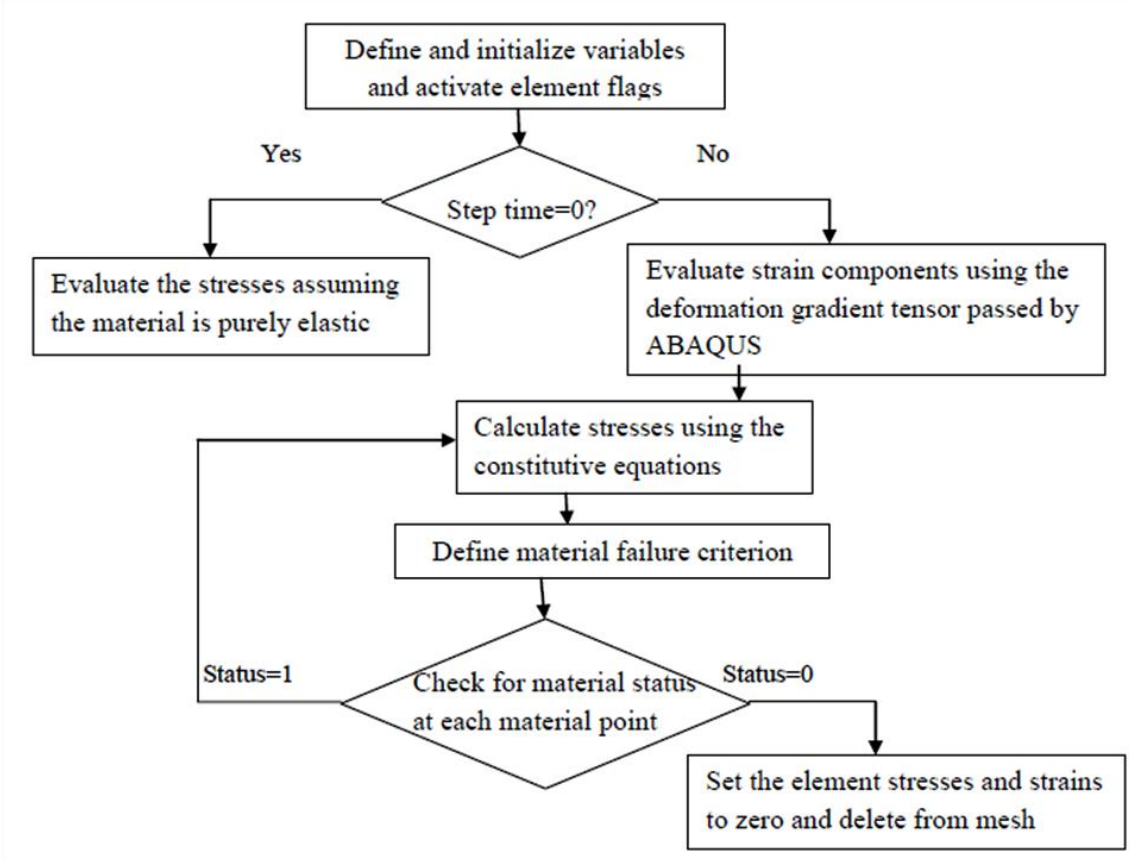

Figure 3-8 Flowchart for VUMAT

3.5 VUMAT testing and validation

In ABAQUS, the implementation of any constitutive model requires extensive initial testing on a single element model with prescribed traction loading.

For the constitutive relationship listed in Eq. (3.3), the values of the spring constants k_1, k_2 and dashpot μ are to be obtained first. The parameters for a constitutive equation of any linear viscoelastic model can be assigned values such that the stress-strain behavior of the derived equation reflects actual constitutive properties of the material of interest. Shim et al. [24] performed dynamic tensile tests on Twaron CT716® fibers using a conventional split Hopkinson bar arrangement to determine the parameters for the three-element linear viscoelastic model. Observations from the experiments showed two distinct regimes of material response in relation to the strain rate. For strain rates exceeding 400 s^{-1} (termed as 'high' strain rates), the stress-strain curves exhibit a much stiffer behavior and also result in an increased tensile strength. Figure 3-9 and Figure 3-10 show the distinct stress-strain behavior for high and low strain rates.

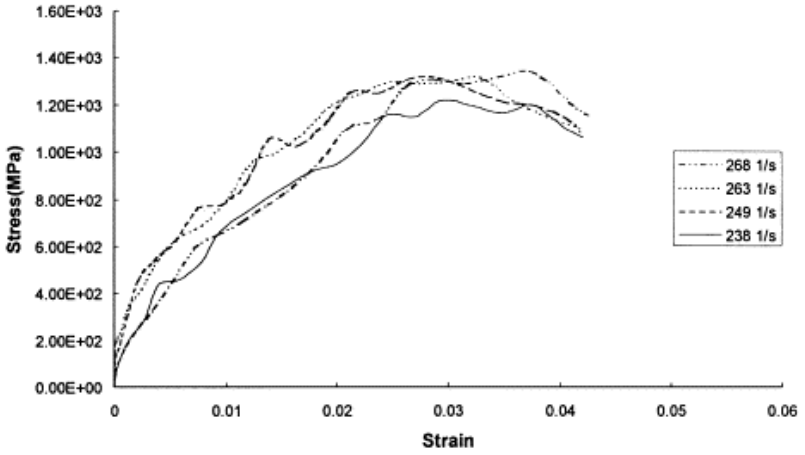

Figure 3-9 Stress-strain curves for low strain rates [24] ($\dot{\varepsilon} < 400\text{s}^{-1}$)

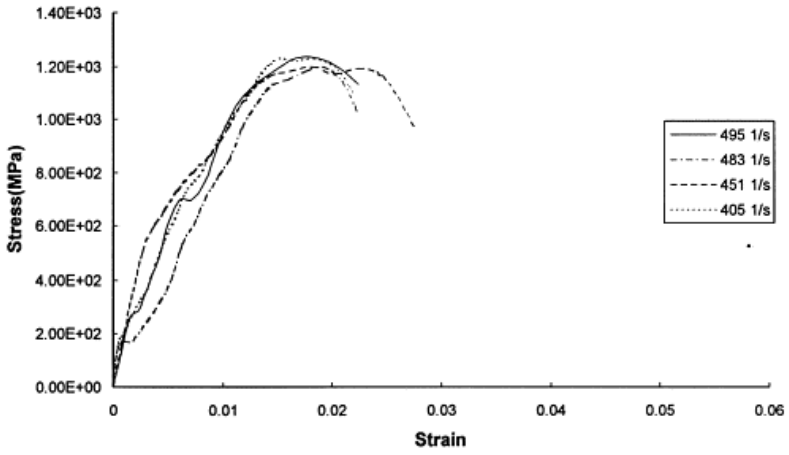

Figure 3-10 Stress-strain curves for high strain rates [24] ($\dot{\varepsilon} \geq 400\mathrm{s}^{-1}$)

David et al. [35] derived the parameters for the same constitutive model by modifying and adjusting the values used in [36], which improved the correlation between the predicted results and the experimental data. Table 3-1 summarizes the constants used in [35] and [36]. The values for the equivalent standard linear solid are evaluated by using Eq. (3.2).

Table 3-1 Summary of constitutive equation parameters

	Paper title	Model	K_1 (Pa)	K_2 (Pa)	η_t (Pa·s)
CT716®	Shim, V.P.W., Lim, C.T., and Tay, T.E., "Modeling Deformation and Damage Characteristics of Woven Fabric under Small Projectile Impact," *Int. J. of Impact Engineering* **16** pp. 585 – 605, 1995.	GKV	1.60×10^{11}	1.56×10^{11}	3.50×10^{7}
		GM(n=1)	8.10×10^{10}	7.90×10^{10}	8.97×10^{5}
	Shim, V.P.W., Lim, C.T., and Foo, K.J., "Dynamic Mechanical Properties of Fabric Armor," *Int. J. of Impact Engineering* **25** pp. 1 – 15, 2001.	GKV	1.10×10^{11}	2.72×10^{9}	4.80×10^{5}
		GM(n=1)	1.07×10^{11}	2.65×10^{9}	4.57×10^{5}
	Lim, C.T., Shim, V.P.W. and Ng, Y.H., "Finite-Element Modeling of the Ballistic Impact of Fabric Armor," *Int. J. of Impact Engineering* **28** pp. 13 – 31, 2003.	GKV	1.60×10^{11}	2.80×10^{9}	3.00×10^{5}
		GM(n=1)	1.57×10^{11}	2.75×10^{9}	2.90×10^{6}
CT709®	David, N.V., Gao, X.-L. and Zheng, J.Q., 2009	GM(n=1)	6.80×10^{10}	2.80×10^{9}	3.00×10^{6}

Using the values obtained in [35] and setting the Poisson's ratio of springs to zero, the coefficients for the $GM^{n=1}$ model shown in Figure 3-5 can be calculated as follows:

Bulk moduli of the two springs

$$K_{k_1} = k_1/3(1-2\nu) = k_1/3 = 22666.7 \text{ MPa},$$

$$K_{k_2} = k_2/3 = 933 \text{ MPa};$$

Shear moduli of the two springs

$$G_{k_1} = k_1/2(1+\nu) = k_1/2 = 34000 \text{ MPa},$$

$$G_{k_2} = k_2/2 = 1400 \text{ MPa};$$

Shear and bulk moduli of the dashpot

$$GV = \eta/3 = 1 \text{ MPa},$$

$$KV = \infty.$$

These values are input to the VUMAT as user defined material constants. The newly developed VUMAT code is then applied and tested on a simple bar consisting on four continuum elements. The uniaxial loading on the viscoelastic bar and the mesh are shown in Figure 3-11. The load is applied instantaneously and the material response is studied for a time period of 0.001s.

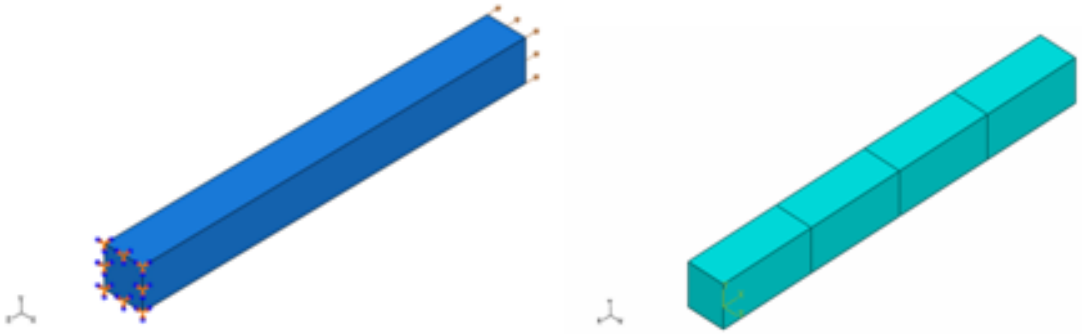

(a) (b)

Figure 3-11 (a) Viscoelastic bar with uniaxial loading (b) Mesh consisting of four C3D8R elements

The load is applied instantaneously and held constant throughout the time step as shown in Figure 3-12, which is equivalent to creep loading.

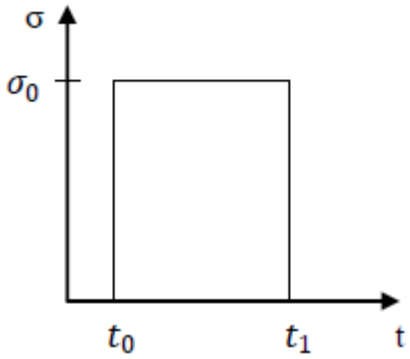

Figure 3-12 Applied load

The following contours in Figure 3-13 depict the principal stress distributions in the axial direction for a load case of 200 MPa at different time instants.

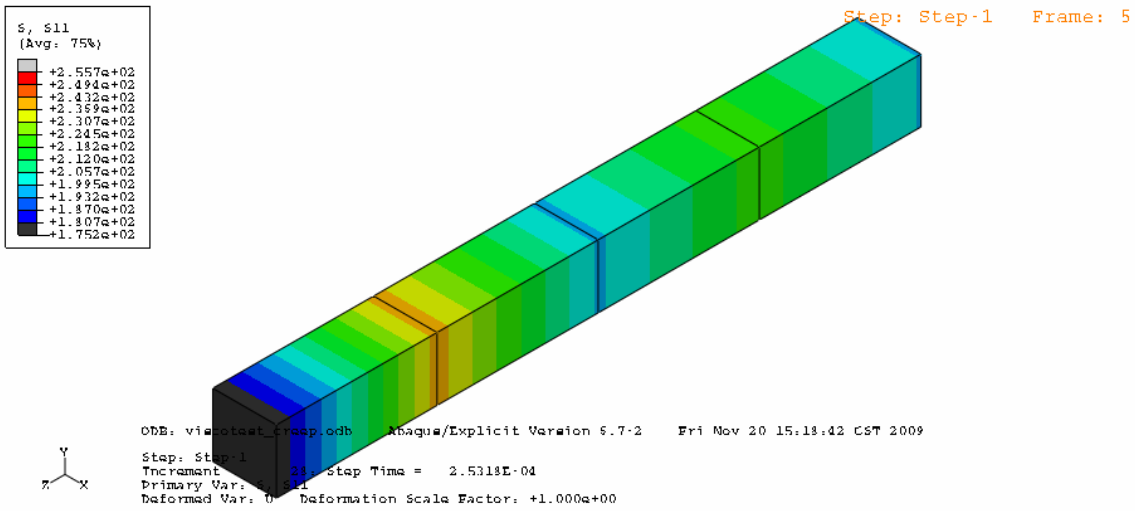

(a)

Figure 3-13 Principal axial stress at (a) t = 250 μs (b) t = 600 μs (c) t = 1000 μs

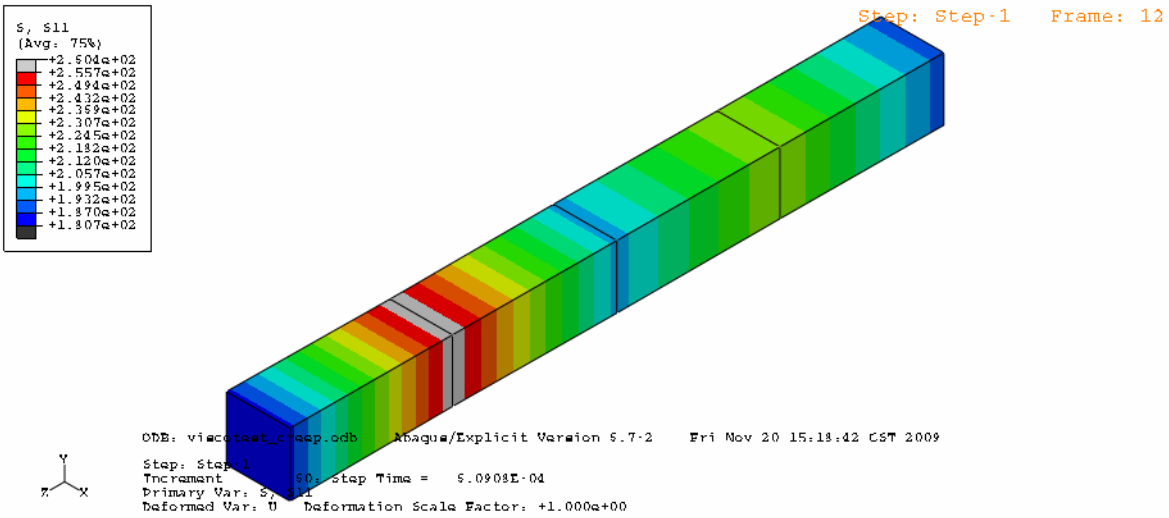

(b)

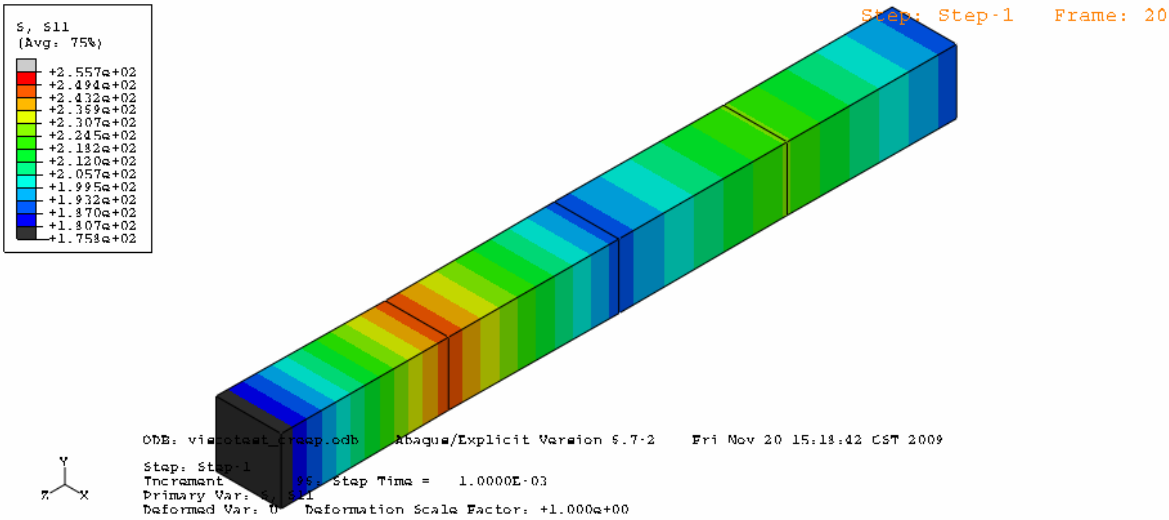

(c)

Figure 3-13 Continued

The corresponding principal logarithmic strain contours in the axial direction are shown in Figure 3-14.

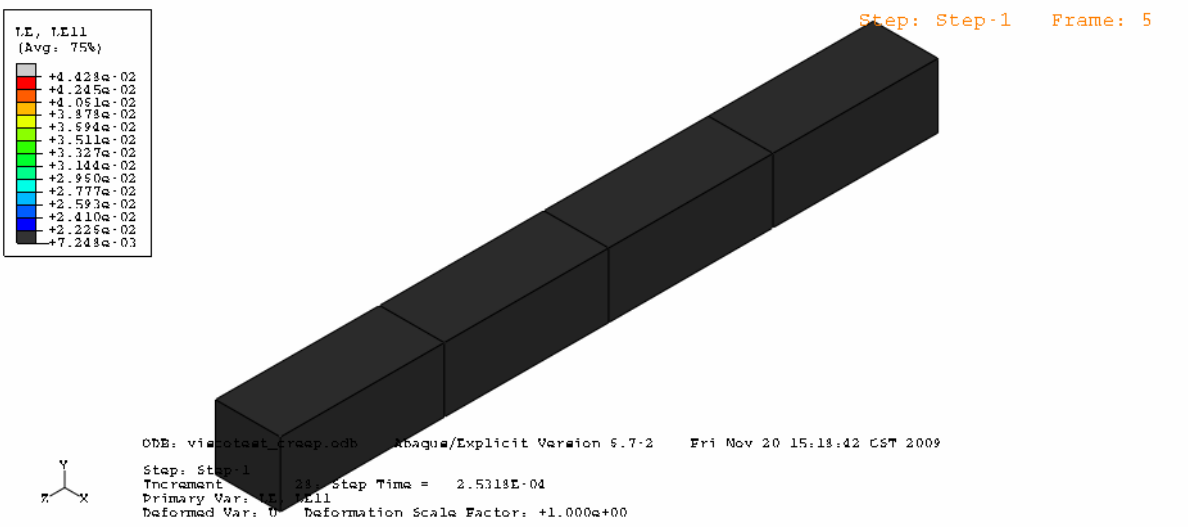

(a)

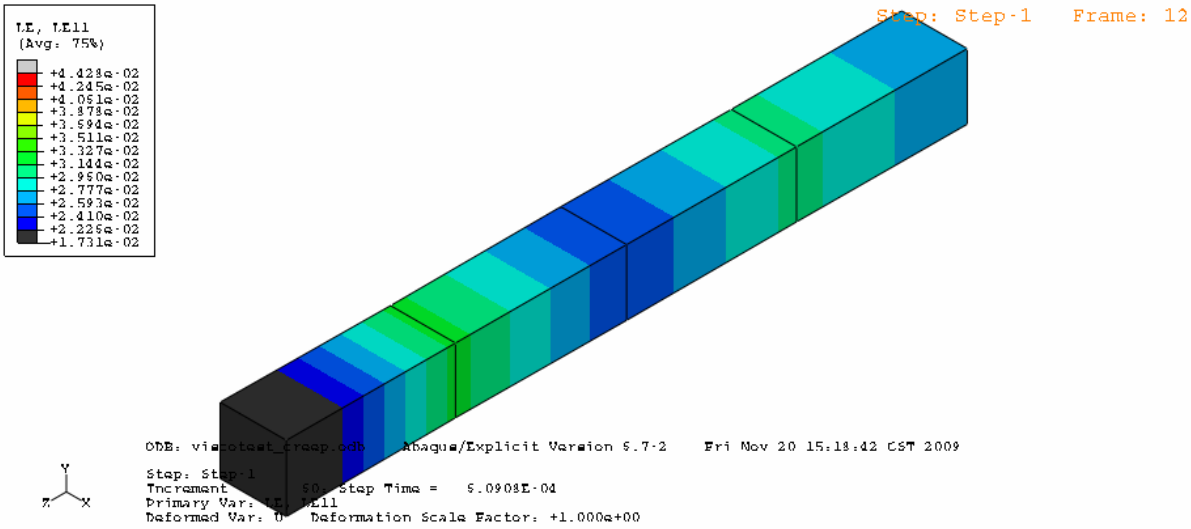

(b)

Figure 3-14 Principal axial strain at (a) t = 250 μs (b) t= 600 μs (c) t = 1000μs

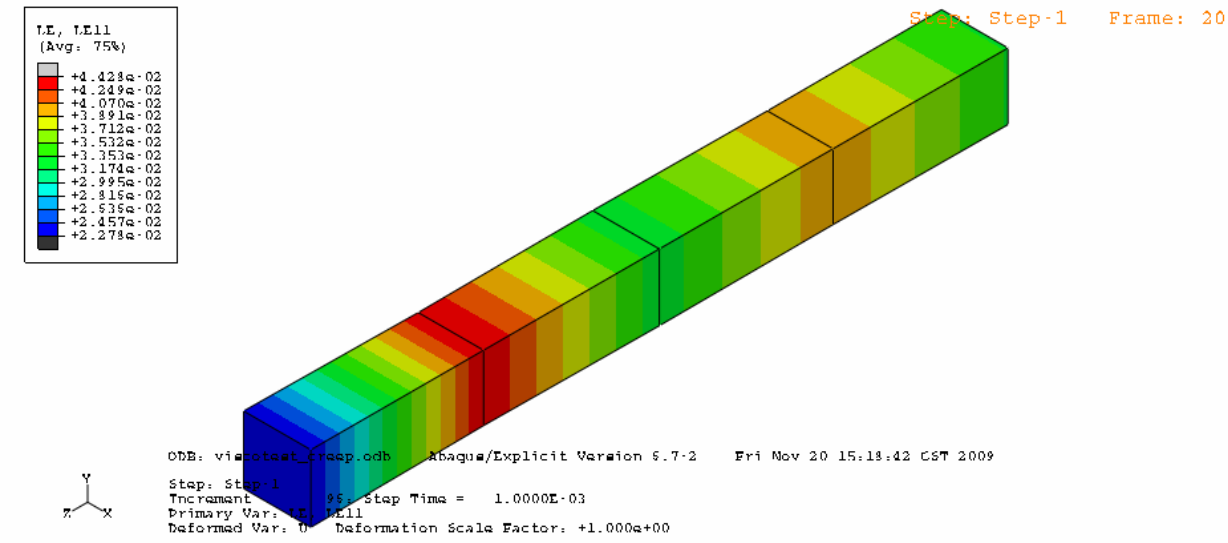

(c)

Figure 3-14 Continued

The stress-strain behavior of the viscoelastic material defined is plotted in Figure 3-15.

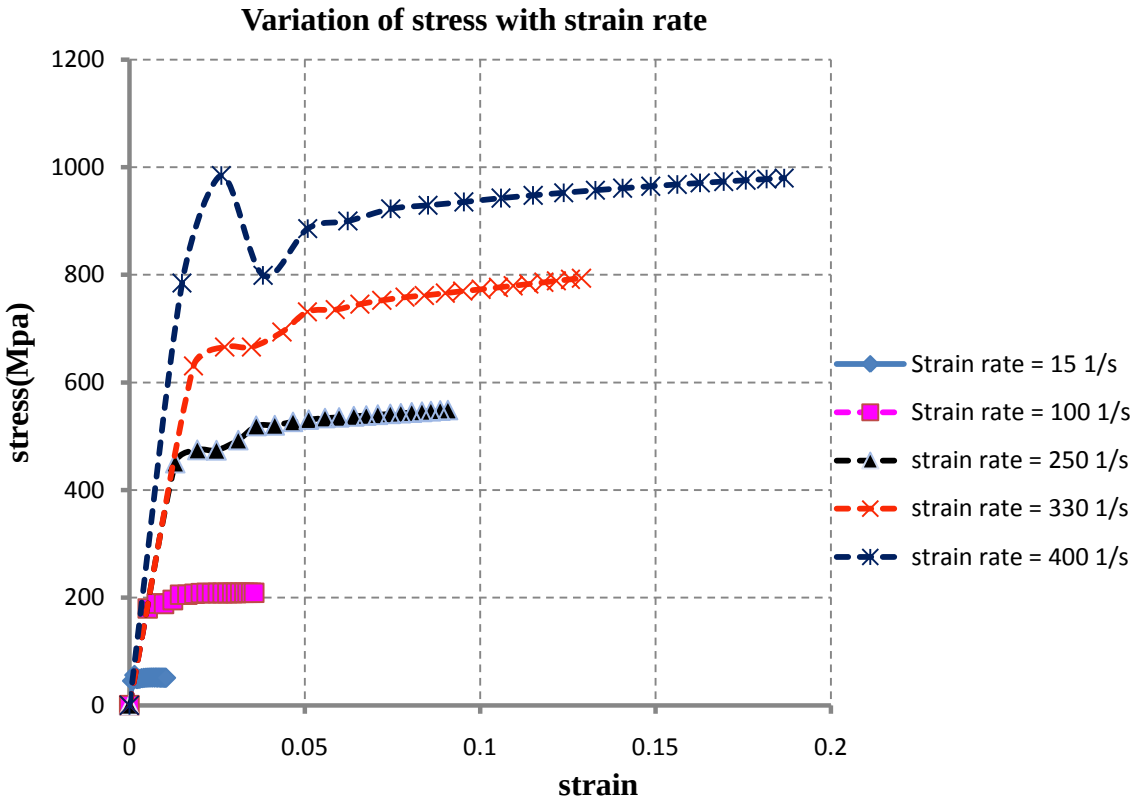

Figure 3-15 Stress-strain curves for the material at different strain rates

As expected, at higher strain rates the material exhibits a stiffer behavior as explained in previous sections. To verify the validity of the VUMAT, a numerical check is performed by solving the equation analytically under the given creep loading conditions.

Eq. (3.4) describes the 1D form of the constitutive Eq. (3.3) which can be rewritten as:

$$\left(1+\frac{K_{k_2}}{K_{k_1}}\right)\dot{\varepsilon}+\frac{K_{k_2}}{3GV}\varepsilon=\frac{\dot{\sigma}}{K_{k_1}}+\frac{\sigma}{3GV}. \tag{3.11}$$

This equation is then solved for the case of constant applied stress (creep) as shown in Figure 3-12.

Since the applied stress $\sigma = \sigma_0$ is constant throughout the time period, $\dot{\sigma} = 0$ in Eq. (3.11). Let $\left(1 + K_{k_2}/K_{k_1}\right) = a$, $K_{k_2}/3GV = b$ and $\sigma_0/3GV = c$, Eq.(3.11) reduces to

$$a\, d\varepsilon/dt + b\varepsilon = c\,, \tag{3.12}$$

which can be rewritten as

$$dt = a d\varepsilon/(c - b\varepsilon)\,. \tag{3.13}$$

Integrating Eq. (3.12), gives

$$ln\,(1 - b\varepsilon/c)/\varepsilon_0 = -\,(b/a)\,t$$

where ε_0 is an integration constant. Upon rearranging, the strain term can be expressed as

$$\varepsilon = c/b\,(1 - \varepsilon_0\, exp(-\,bt/a\,)\,) \tag{3.14}$$

The integration constant ε_0 can be obtained from the initial conditions, i.e., $\varepsilon|_{t=0}$, which gives $\varepsilon_0 = 1$. Substituting this back in Eq. (3.13), yields

$$\varepsilon = c/b\,(1 - exp(-\,bt/a\,))\,. \tag{3.15}$$

Replacing the constants *a*, *b* and *c* by the actual constants defined earlier gives the expression for the strain as

$$\varepsilon = \sigma_0/K_{k_2}\left(1 - exp\left(-\frac{K_{k_1}K_{k_2}}{3GV\left(K_{k_1} + K_{k_2}\right)}t\right)\right). \tag{3.16}$$

This equation shows that the strain is exponentially increasing with time throughout the time period when a constant stress is applied. This typical behavior of a viscoelastic material is called Creep.

The strain histories obtained from the VUMAT are compared with the numerical results obtained by substituting the constants derived earlier for different load conditions. The cases with applied uniaxial stress values of 20, 200, 500, 700 and 900 MPa are evaluated and compared with the FE results in Figure 3-16.

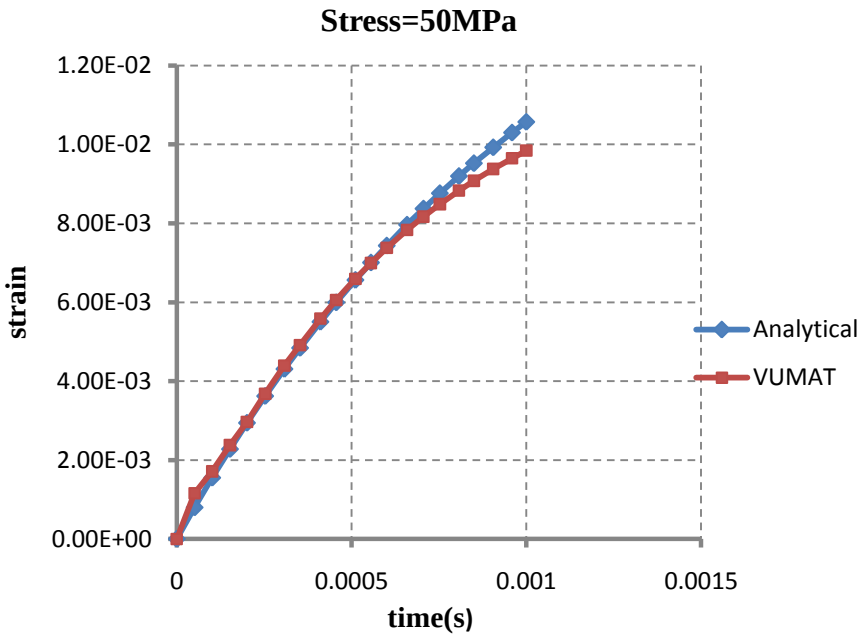

(a)

Figure 3-16 Comparison of strain histories for stress at (a) 50 MPa, (b) 200 MPa, (c) 500 MPa, and (d) 900 MPa

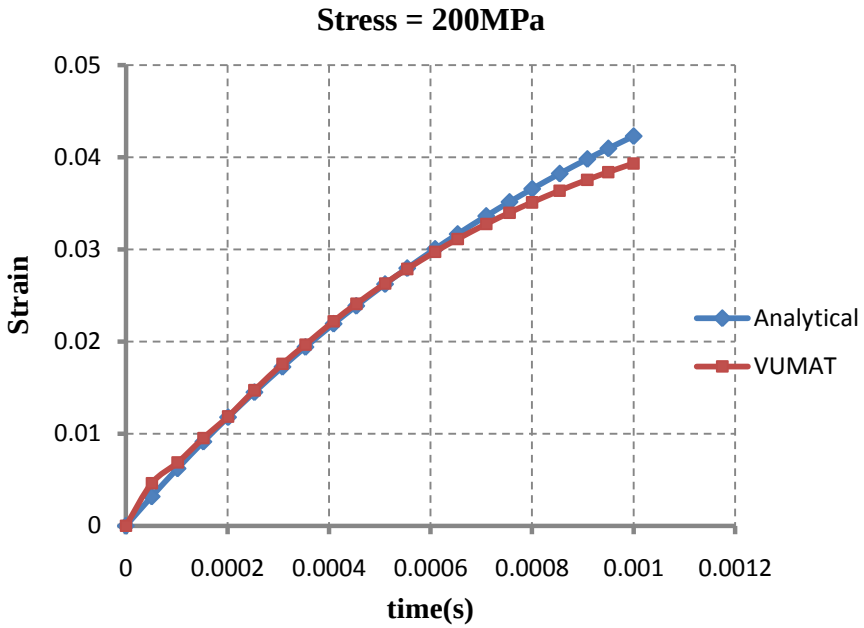

(b)

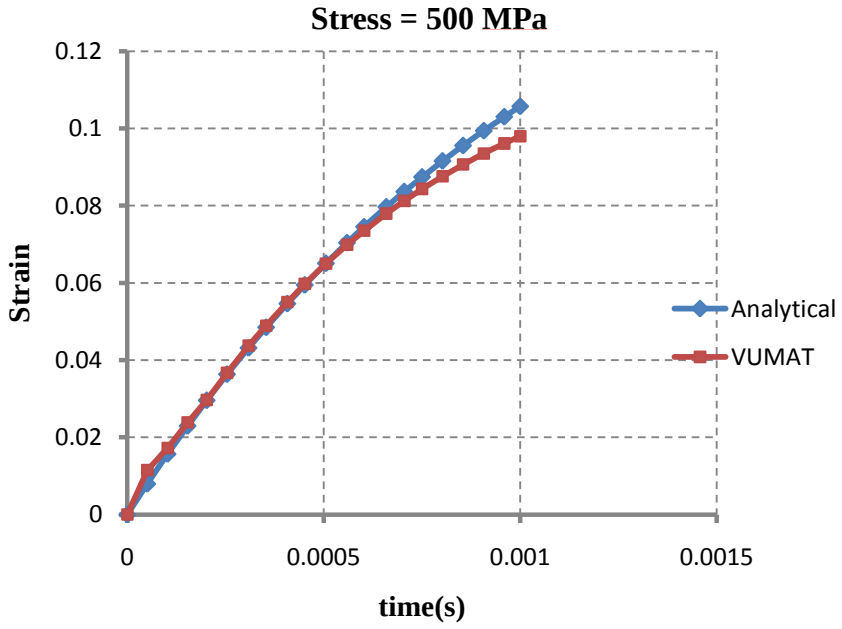

(c)

Figure 3-16 Continued

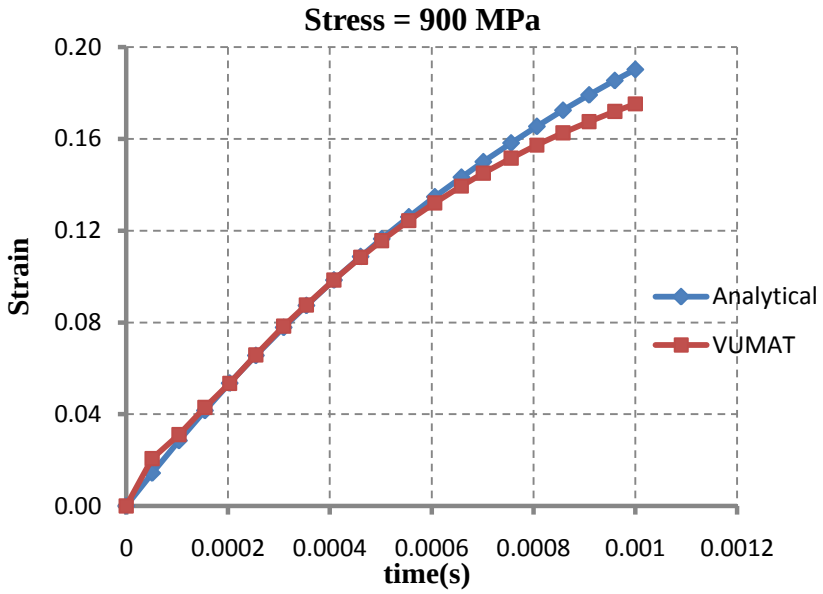

(d)

Figure 3-16 Continued

Observations

The strain history predicted by the VUMAT compares well with the analytical results. The slight deviation observed can be attributed to the following factors

1) The strain values are evaluated by averaging the value at each integration point of the four elements;
2) The strain measure used in the VUMAT is the Green strain whereas the analytical solution gives the true strain.

This VUMAT accounts for the material behavior of the Twaron CT709® fabric analyzed in the next section.

4. NUMERICAL SIMULATION RESULTS, DISCUSSION AND CONCLUSION

4.1 Validation

The fabric model proposed was analyzed in ABAQUS/Explicit for pre-defined bullet velocity and prescribed boundary conditions. The outputs have been studied and compared with results available in the literature. The residual velocity predicted by the simulation shows good correlation with the experimental results obtained by Tan et al. [37]. Table 4-1 compares the residual velocity obtained from the simulation and the experimental data for the 9mm diameter cylindrical bullet.

Table 4-1 Comparison of predicted and measured values of the residual velocity

Impact velocity(m/s)	Residual Velocity(m/s)		Relative error (%)
	Simulation	Experimental [28]	
250	245	232	5.6
332	326	320	1.875
358	351	339	3.54
427	419	412	1.7

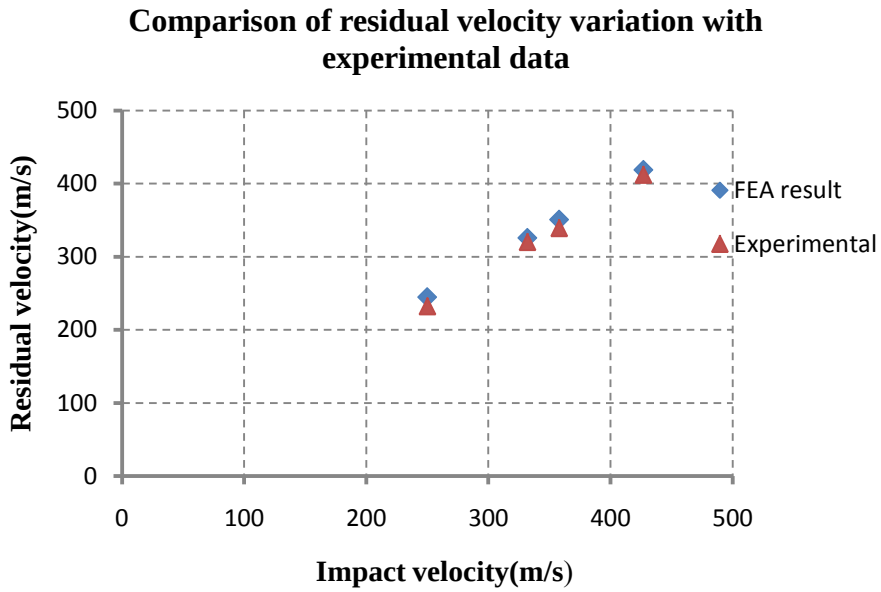

Figure 4-1 Residual vs. Impact velocity (m/s)

Figure 4-1 compares the residual velocities obtained FEA with measured values. The residual velocity values obtained in the current simulations are higher than the experimental values thereby providing a conservative ballistic limit. The deviation is mainly due to the approximations:

1) The yarn is modeled as a continuum, whereas it is actually a collection of thousands of filaments. The frictions between these filaments contribute to additional energy absorbed by the fabric.
2) When an element satisfies the user-defined failure criterion, namely the maximum stress criterion in this study, it is deleted from calculation. In reality, the damage evolution process is much gradual and follows a complex fracture process.

3) The ballistic event is assumed to be isothermal in the FEA calculations, whereas there is a slight loss of energy in the form of heat during experiments.

4.2 Parametric study

A parametric study helps understand the system response to the variation in each system parameters. It gives an idea as to how the fabric performance can be improved by varying the system properties. For the test series I, four cases with different impact velocities are studied .The remaining parameters including the bullet shape and mass, inter-yarn friction, and projectile-fabric friction are kept constant. Table 4-2 describes the four cases under consideration.

Table 4-2 Test series I: Impact velocity variation

Case	Impact velocity(m/s)
1	250
2	332
3	358
4	427

Table 4-3 shows the variation in projectile mass for the same fabric model when keeping the other parameters such as impact velocity, and projectile shape constant. This leads to the test series II results.

Table 4-3 Test series II: Variation in projectile mass

Impact velocity(m/s)	Projectile mass(g)	Simulated Projectile
332	8	9 mm
	10.2	357 magnum
	11.7	40 S&W
	15.6	44 magnum

To study the effect of projectile geometry on the impact characteristics, two more projectile shapes, namely spherical and hemispherical are considered while keeping the mass and other parameters constant. Table 4-4 lists the test series III cases.

Table 4-4 Test Series III: Projectile geometry variation

Case	Projectile shape
1	Cylindrical
2	Hemi-spherical
3	Spherical

Boundary conditions play an important role in determining the response of a fabric target. When a fabric is perforated by a projectile, the stress waves generated at the time of impact are reflected from the fabric target boundaries. Hence the effect of

two different gripping conditions is studied in test series IV. Table 4-5 shows these cases.

Table 4-5 Gripping conditions

Case	Boundary condition
1	All four edges clamped
2	Two edges clamped

Test series V deals with the study of energy absorbed by varying the number of layers of the fabric target. Table 4-6 lists the four different layers of the fabric target.

Table 4-6 Variation in fabric target layers

Case	Number of layers
1	Single
2	Double
3	3-
4	4-

Friction between the yarns affects the lateral mobility of yarns near the region of impact. Experimental studies by Briscoe et al. [38] reported a change in the compliance of weaves with a change in inter-yarn friction. In the test series VI, the effect of inter-

yarn friction on the fabric impact process is studied. Table 4-7 describes the different friction factors considered.

Table 4-7 Variation in inter-yarn friction factor

Case	Friction factor
1	0.01
2	0.1
3	0.2
4	0.3
5	0.4
6	0.5

4.2.1 Test series I: simulation of a 9mm cylindrical bullet (8g) impacting fabric at different velocities

Residual velocity values have been obtained for four different test cases. The inter-yarn friction and projectile-yarn friction is assumed to be 0.3. Figure 4-2 shows the various stages in the fabric deformation during the impact process. The pyramidal deformation can be clearly seen in the contours.

Case 1: Velocity of impact = 250 m/s

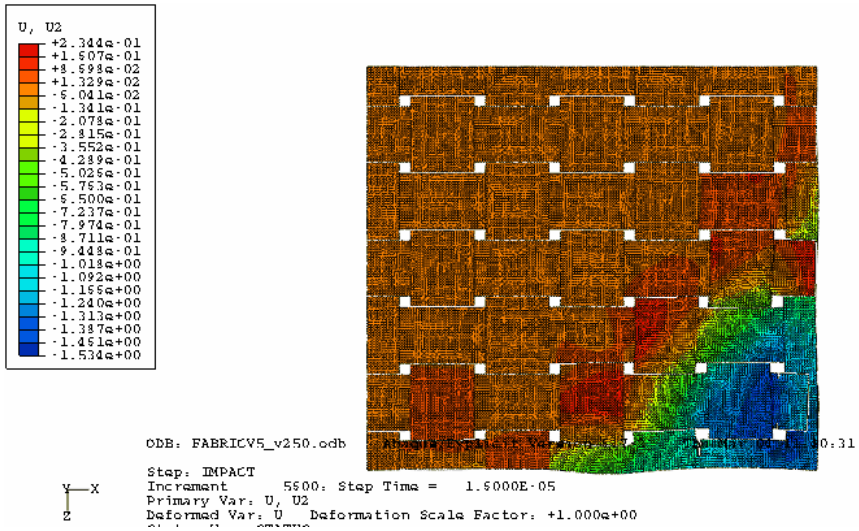

t = 15μs

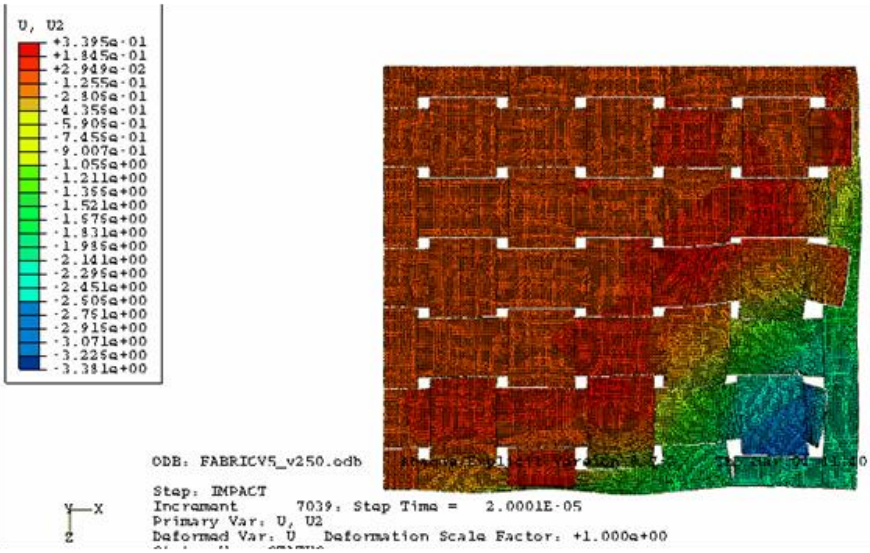

t =20 μs

Figure 4-2 Fabric transverse deformation profile for impact velocity of 250 m/s

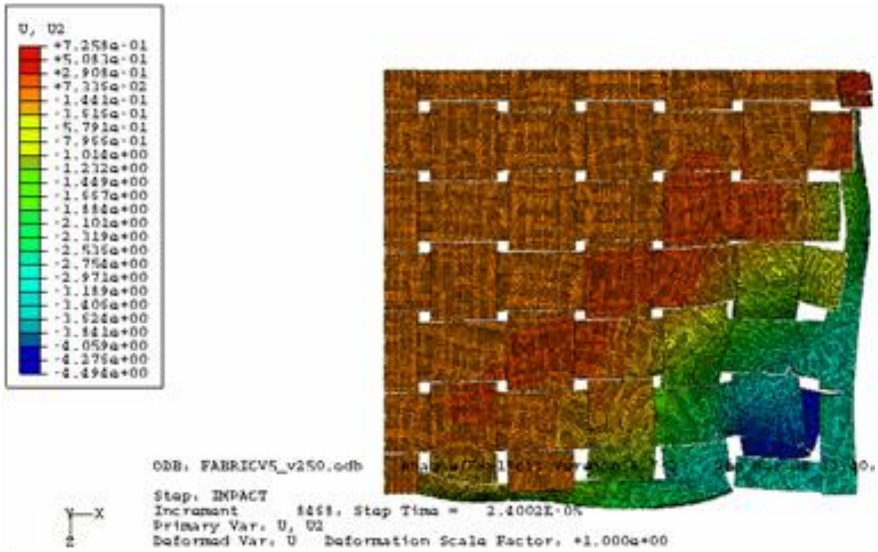

$t = 25$ μs

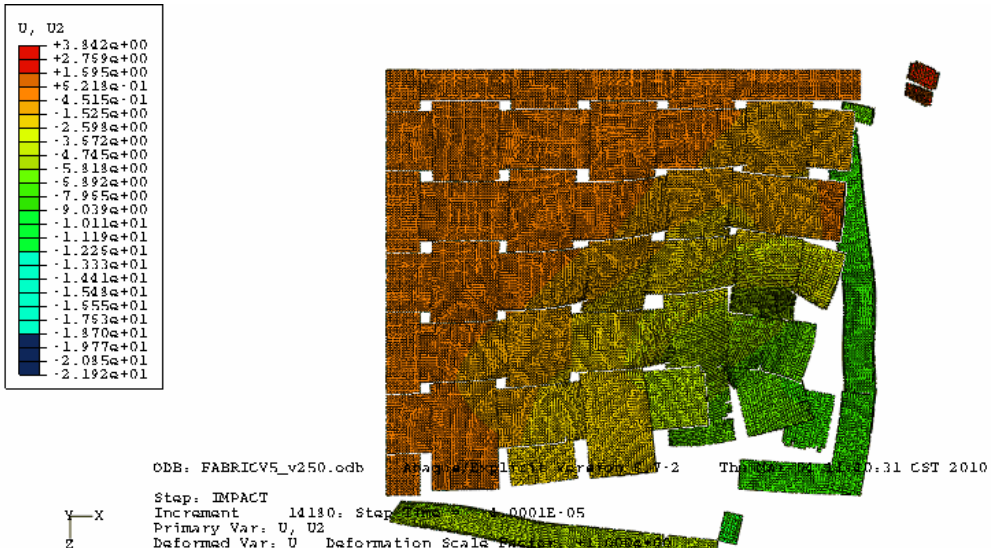

$t = 40$ μs

Figure 4-2 Continued

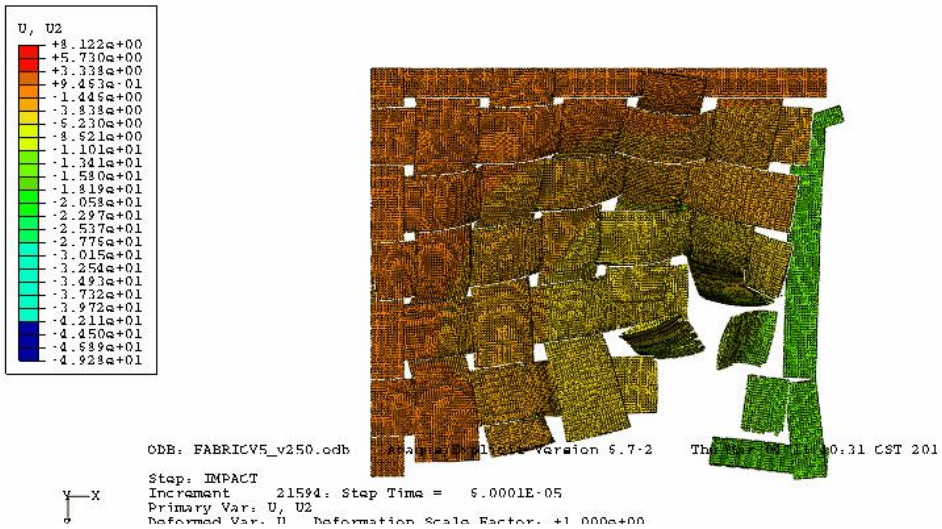

t=60 μs

Figure 4-2 Continued

Figure 4-3 and Figure 4-4 show the bullet velocity and kinetic energy history respectively for an impact velocity of 250 m/s.

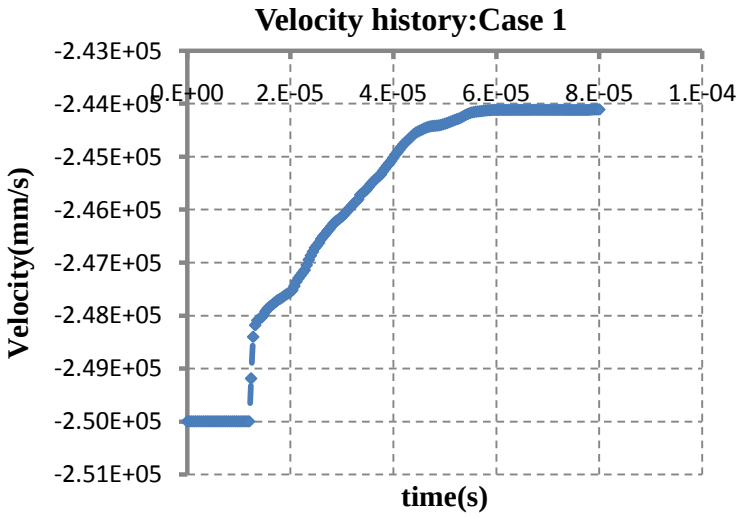

Figure 4-3 Bullet residual velocity for impact velocity of 250 m/s

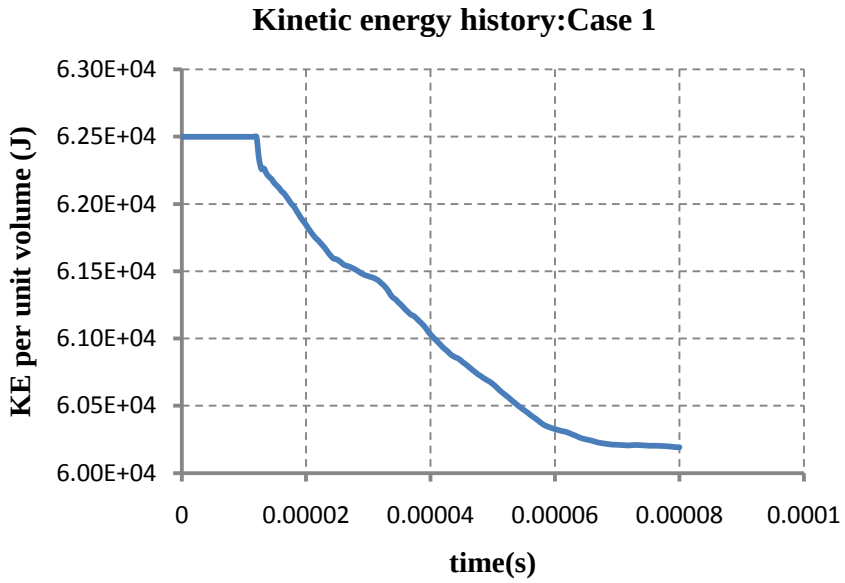

Figure 4-4 Kinetic energy loss for impact velocity of 250 m/s

Case 2: Velocity of impact = 332 m/s

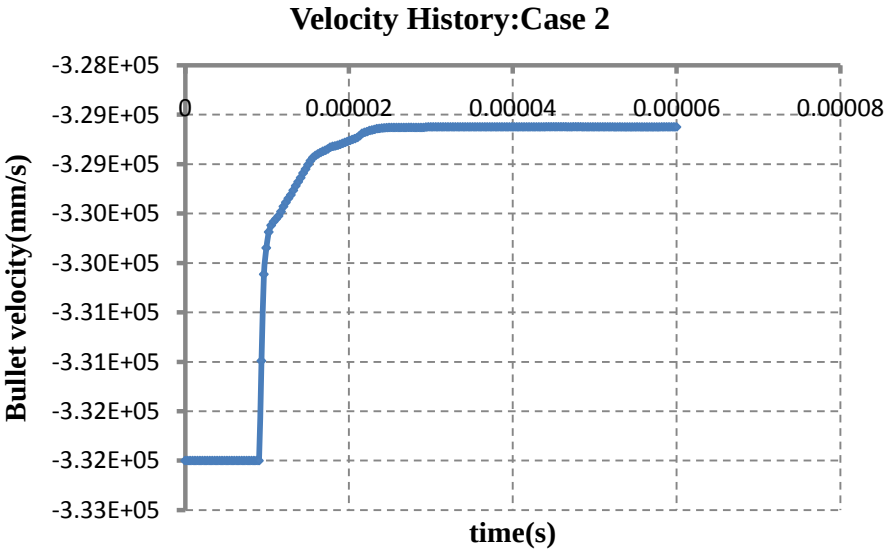

Figure 4-5 Bullet residual velocity for impact velocity of 332 m/s

Figure 4-5 and Figure 4-6 show the bullet velocity and kinetic energy history respectively for an impact velocity of 250 m/s.

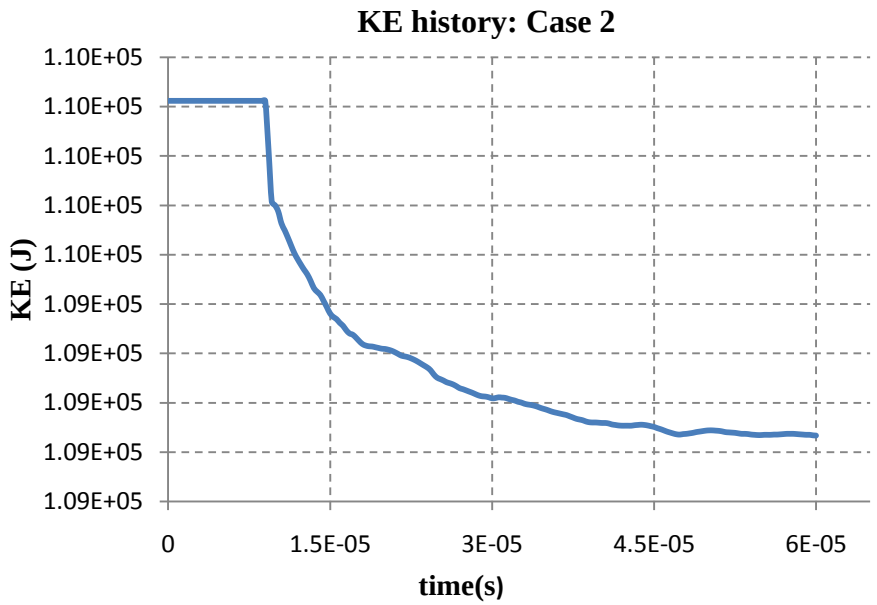

Figure 4-6 Kinetic energy (KE) loss for impact velocity of 332 m/s

Case 3: Velocity of impact = 358 m/s

Figure 4-7 shows the fabric deformation during the impact process for an impact velocity of 358 m/s.

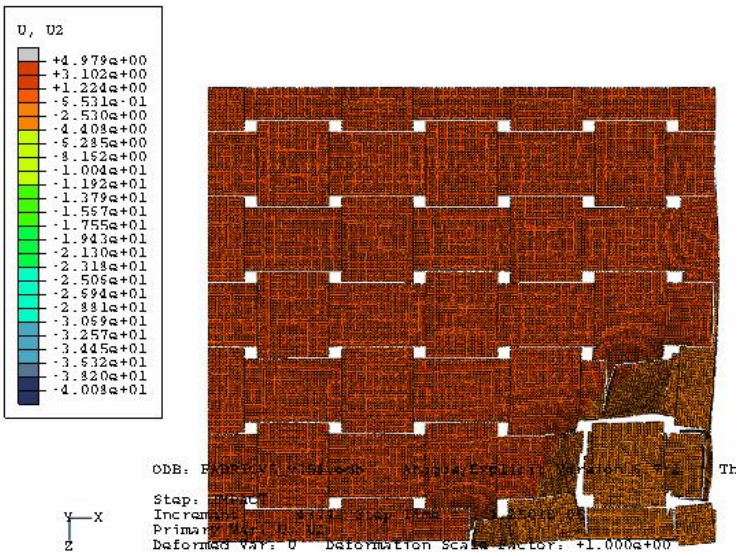

$t = 12.5\mu s$

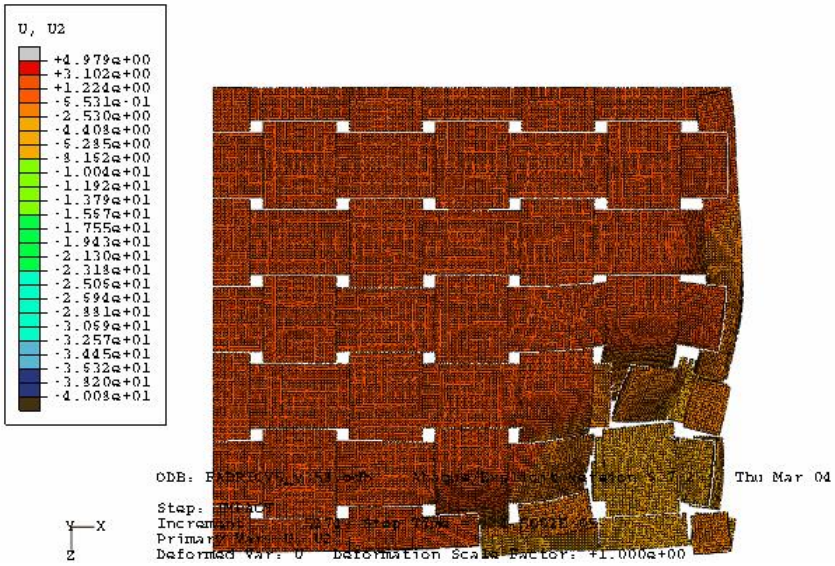

$t = 15\mu s$

Figure 4-7 Fabric transverse deformation profile for impact velocity of 358 m/s

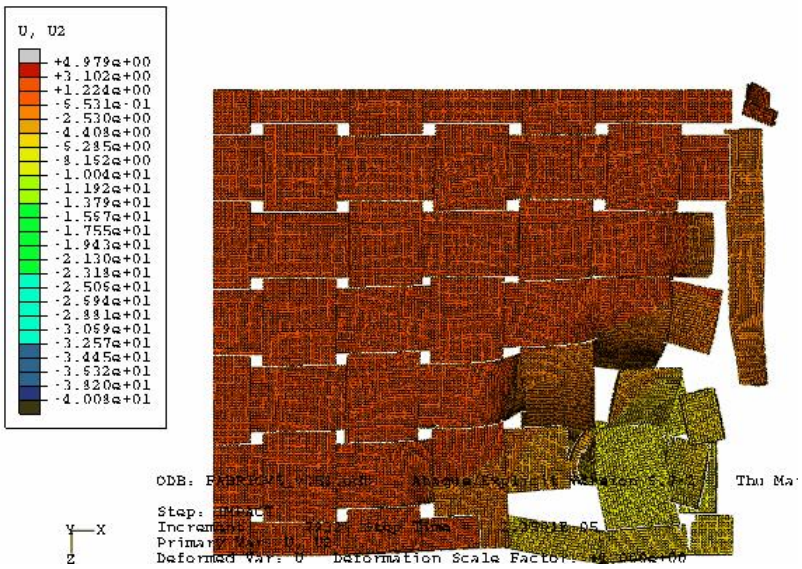

t = 22.5 μs

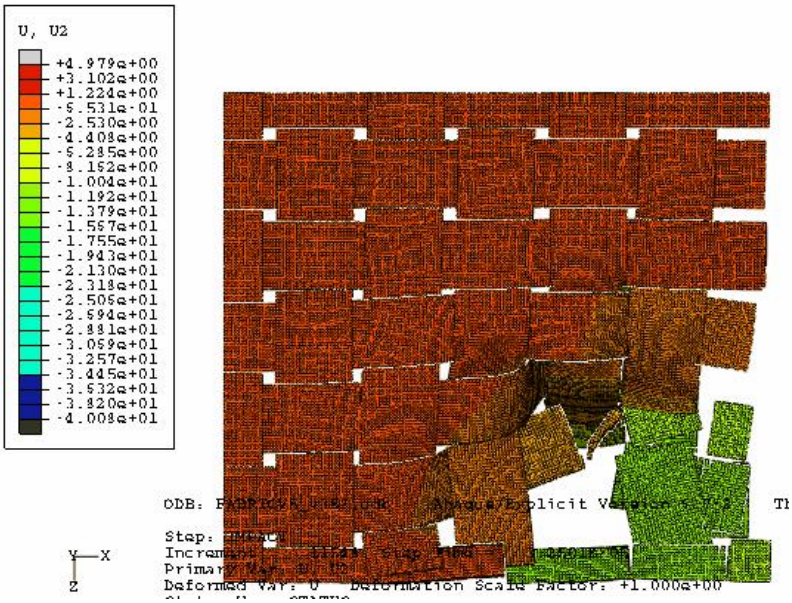

t = 32.5 μs

Figure 4-7 Continued

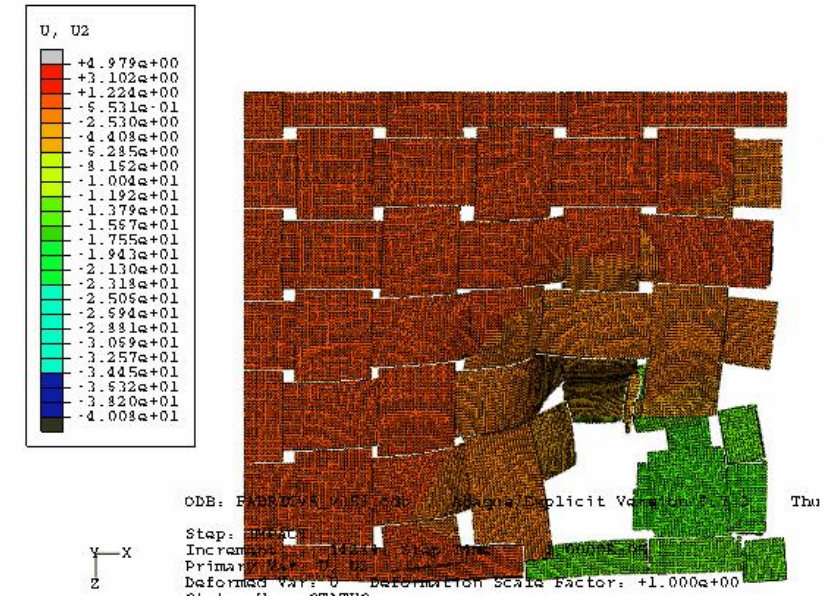

$t = 40$ μs

Figure 4-7 Continued

It can be seen that the yarn failure occurs instantaneously even before the stress wave reached the boundaries. Figures 4-8 and 4-9 depict the velocity history and KE lost by the projectile for an impact velocity of 358 m/s.

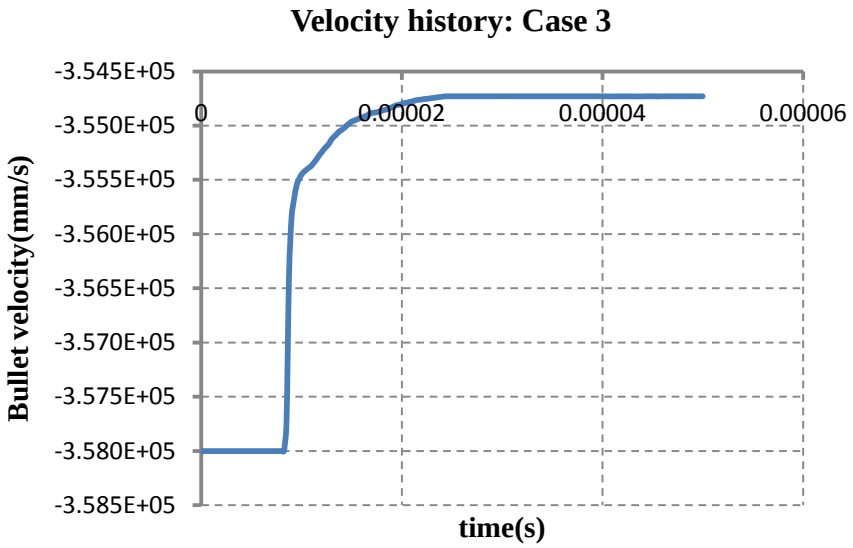

Figure 4-8 Bullet residual velocity for impact velocity of 358 m/s

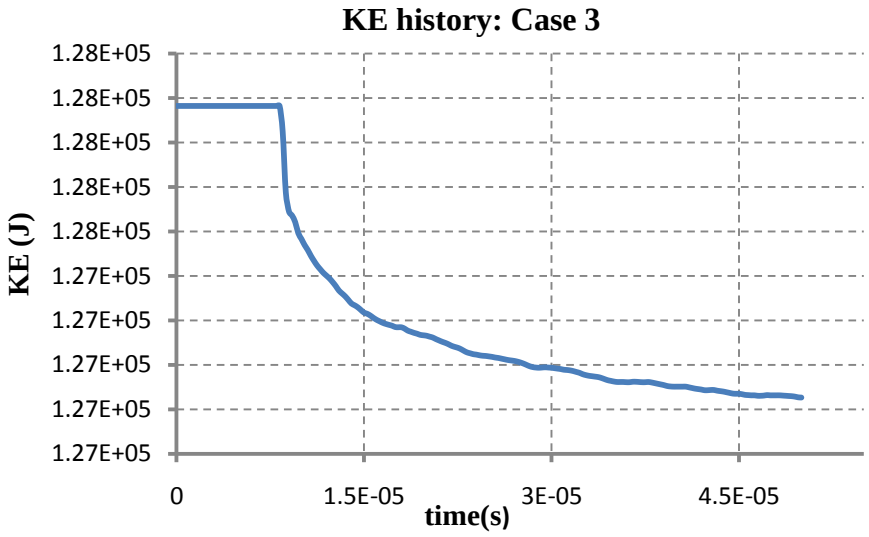

Figure 4-9 Kinetic Energy loss for impact velocity of 358 m/s

Case 4: Velocity of impact = 427 m/s

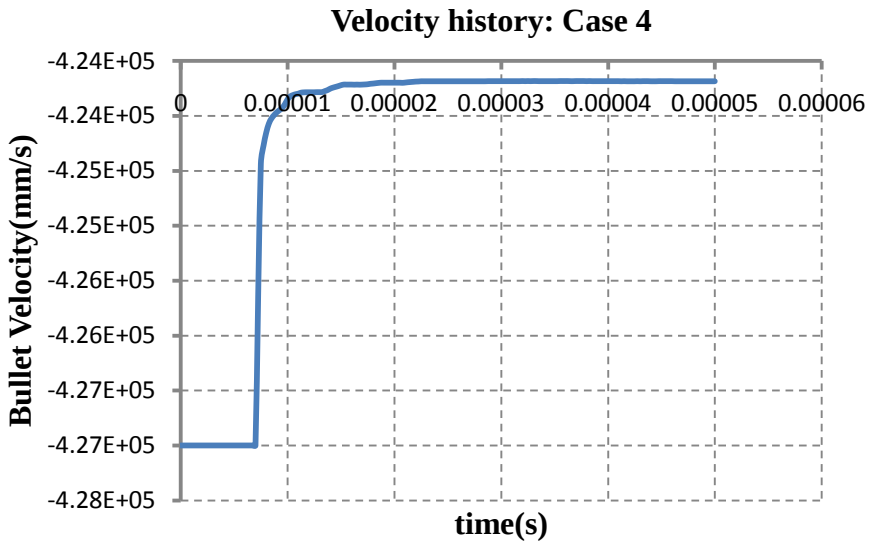

Figure 4-10 Bullet residual velocity for impact velocity of 427 m/s

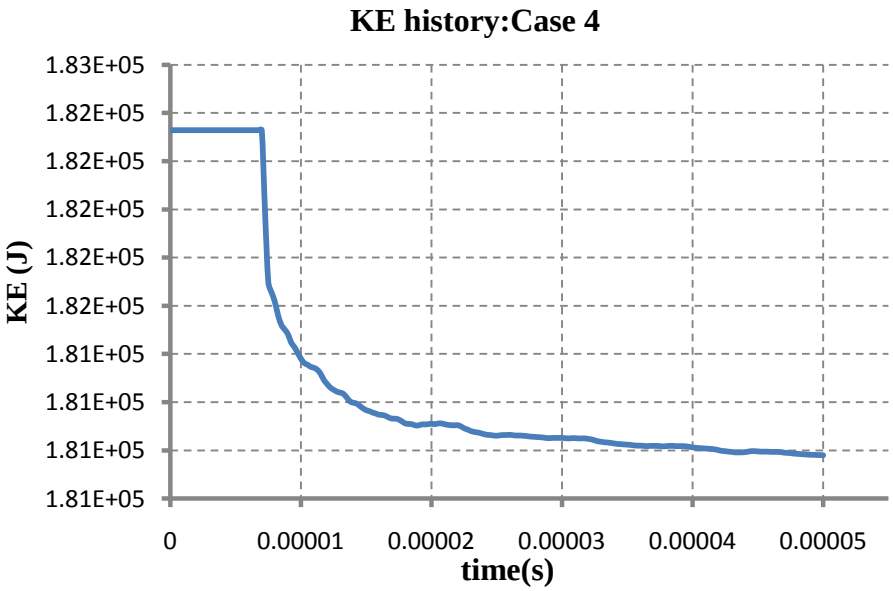

Figure 4-11 Kinetic energy loss for impact velocity 427 m/s

Figure 4-10 and Figure 4-11 depict the velocity history and KE lost by the projectile respectively for an impact velocity of 427 m/s.

The residual velocities predicted by the model compares well with the experimental results. Though the current model over predicts the residual velocity by a margin of 5-15 m/s, the trend obtained is similar.

Variation in fabric strain energy

Figure 4-12 depicts the strain energy (SE) absorption trend for different impact velocity cases.

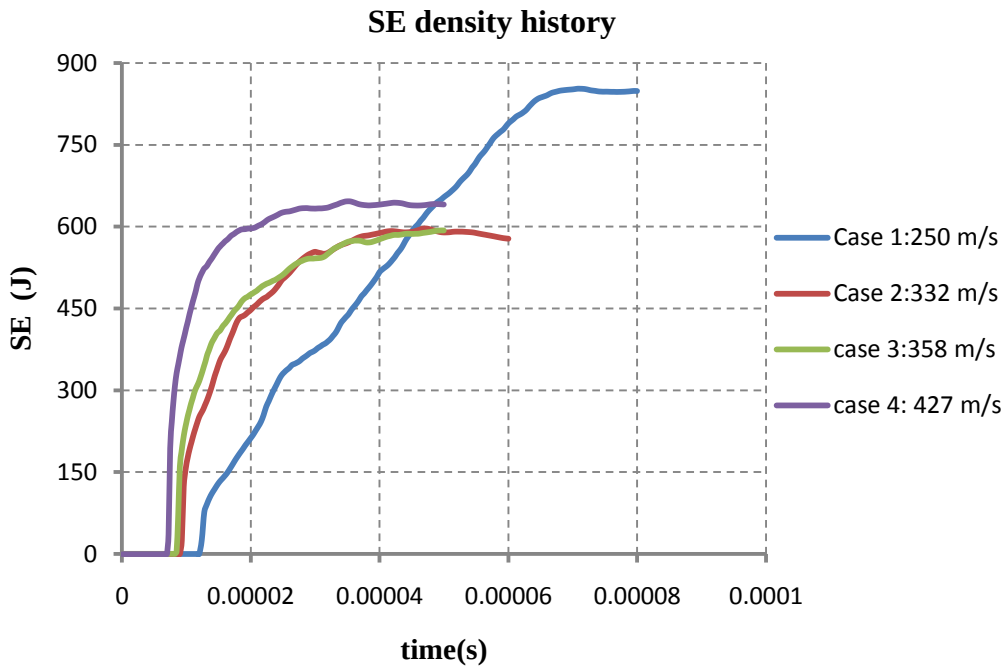

Figure 4-12 Energy absorbed by the fabric for different impact velocities

Figure 4-13 compares the frictional dissipation for different impact velocities.

Variation in frictional dissipation

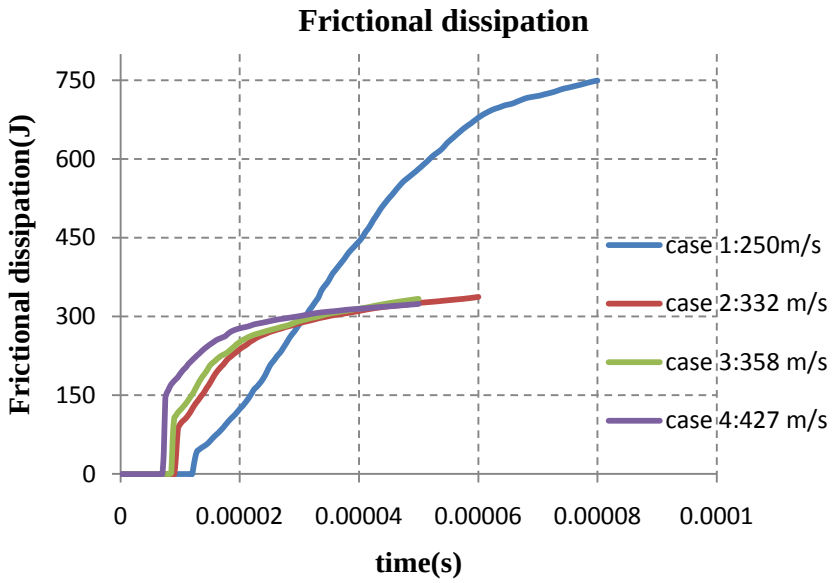

Figure 4-13 Variation of frictional dissipation

Table 4-8 compares the various energies for two representative impact velocities of 250 and 358 m/s.

Table 4-8 Comparison of energy variation

	250 m/s	358 m/s
KE lost by bullet	2300 J	1300 J
SE gained by fabric	860 J (37%)	590 J (45%)
Frictional dissipation	740 J (32%)	330 J (25%)
KE of fabric	550 J (23%)	240 J (18%)

Observations

The given velocity cases fall in the regime of the ballistic limit and the critical velocity. (The critical velocity is defined as the velocity above which there is no considerable absorption of energy by the fabric, and the bullet residual velocity is almost same as the impact velocity). This region is considered as the "low" velocity impact region, where the initial increase in stress is insufficient to attain the fracture stress of the fabric. Hence, the transverse deflection has time to propagate to the edges, which allows the fabric to absorb more energy. The behavior of the fabric within this region is denoted by extensive creasing and stretching, which contributes significantly to energy dissipation. Figure 4.2 shows that the transverse wave propagates towards the boundaries stretching the yarns .Thus, as expected, the strain energy rise in the fabric is the highest for the lowest impact velocity of 250 m/s, as depicted in Figure 4-12.

Higher velocity impacts, on the other hand, tend to break the fabric by shearing across the yarns rather than extending them as shown in Figure 4-7. The damage is localized, and the yarns fail prematurely even before significant transverse deflections can occur. Thus, the amount of strain energy rise at higher velocities is considerably lower, as shown in Figure 4-12.

Also, the amount of strain energy absorbed and a comparison with other sources of energy loss in the next sub-section indicate that the fabric strain energy gain accounts for most of the energy absorbed.

From Table 4-8 it can be observed that at low impact velocities both the yarn strain energy and frictional dissipation are major energy dissipation mechanisms.

However, as the impact velocity increases, the damage is more and more localized and the energy dissipation due to frictional sliding decreases.

Contact force on the projectile

Figure 4-14 shows the variation in contact force with projectile impact velocity.

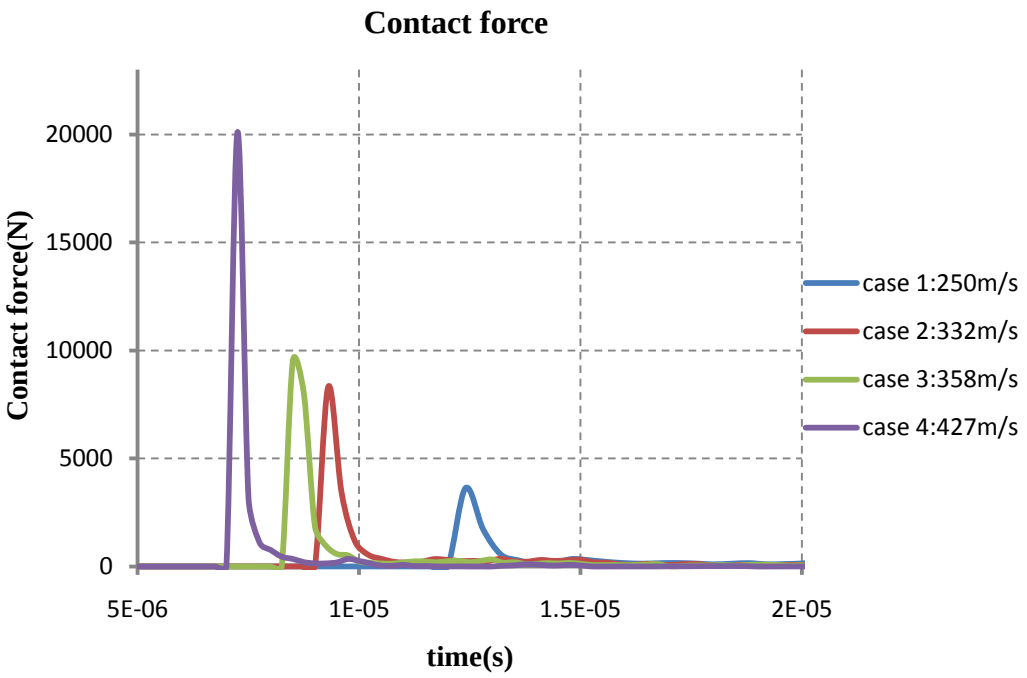

Figure 4-14 Variation in contact force with projectile velocity

It is noted that the bullet is in contact with the fabric for a very short period of time. The maximum resistance is offered to the bullet at the time of impact, and as the bullet continues penetrating the fabric, lesser area of fabric is in contact with the bullet, thereby decreasing the contact force. The decrease in contact force is abrupt owing to the geometry of the projectile. At the time of impact, due to the blunt nose of the projectile

maximum contact force is generated, which decreases abruptly as the projectile slips past the fabric.

4.2.2 Test series II: simulation for different projectile masses at impact velocity of 250 m/s

The higher the mass of projectile is the higher is the initial kinetic energy of the impact. Since the fabric offers a constant resistance, the residual velocity is higher.

Figure 4-15 shows the velocity degradation of the projectile with respect to time for four prescribed bullet masses.

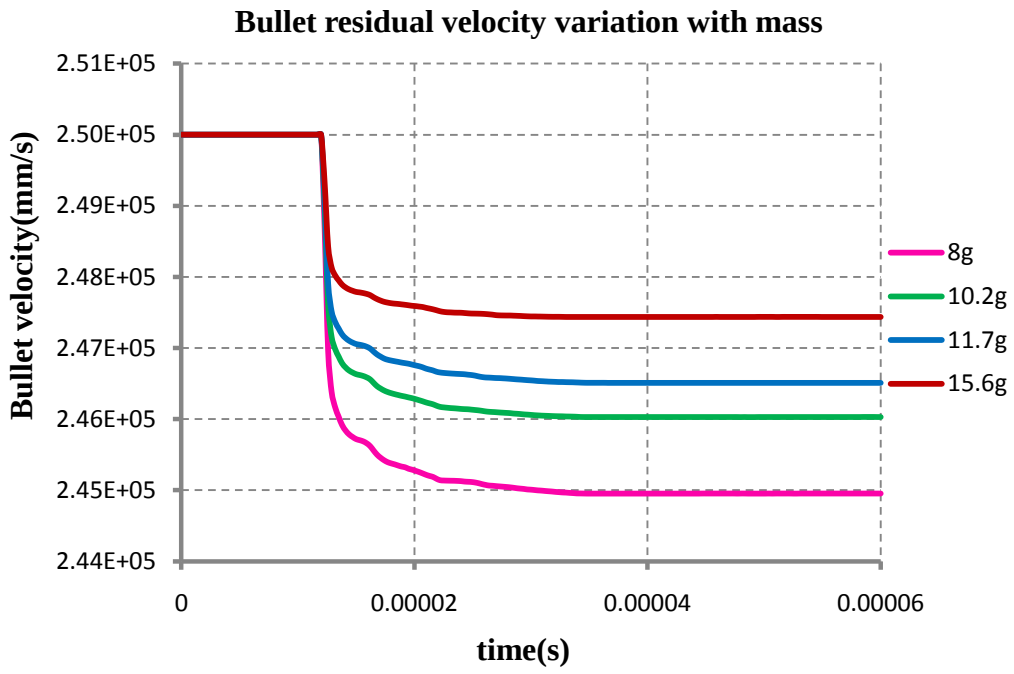

Figure 4-15 Residual velocity of bullet

Figure 4-16 shows the amount of strain energy gained by the fabric for the four cases.

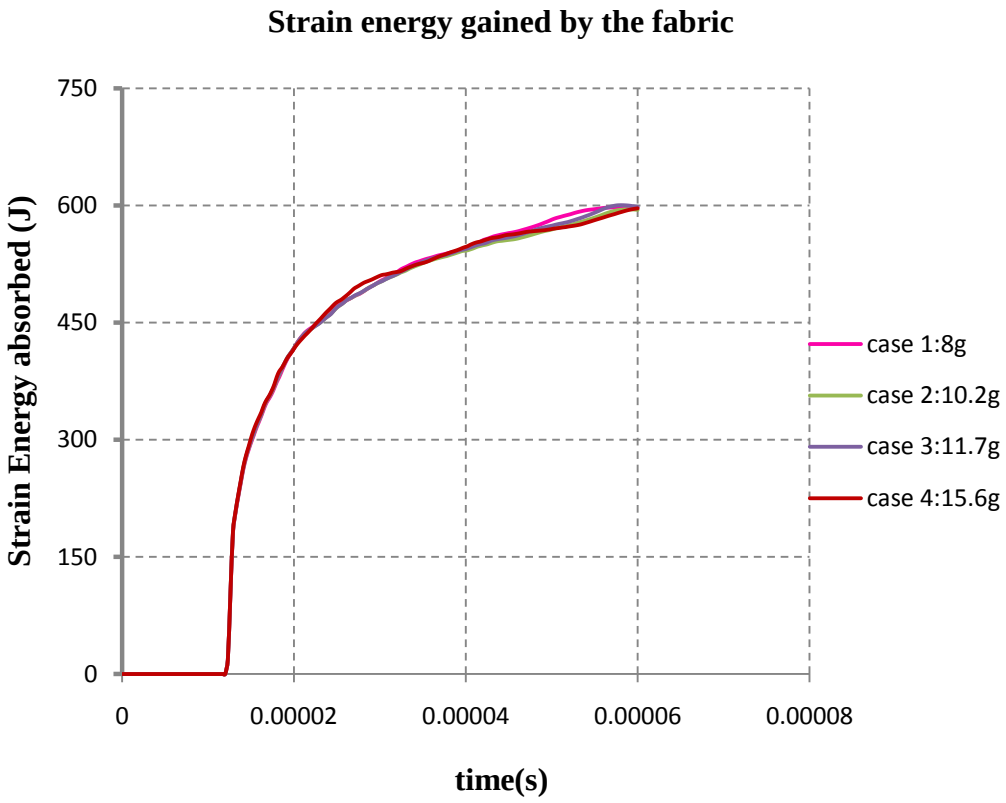

Figure 4-16 Strain energy rise in the fabric

Observations

The residual velocity of the bullet increases from 245 m/s to 247m/s with increase of the projectile mass from 8*g* to 15.6*g*. From Figure 4-16 it can be concluded that the amount of strain energy rise in the fabric remains almost the same for all four cases. Hence, the energy absorbed by the eroded fabric remains constant.

The four cases with varying projectile mass are summarized in Figure 4-17. Increase in projectile mass results in an increase in the residual velocity.

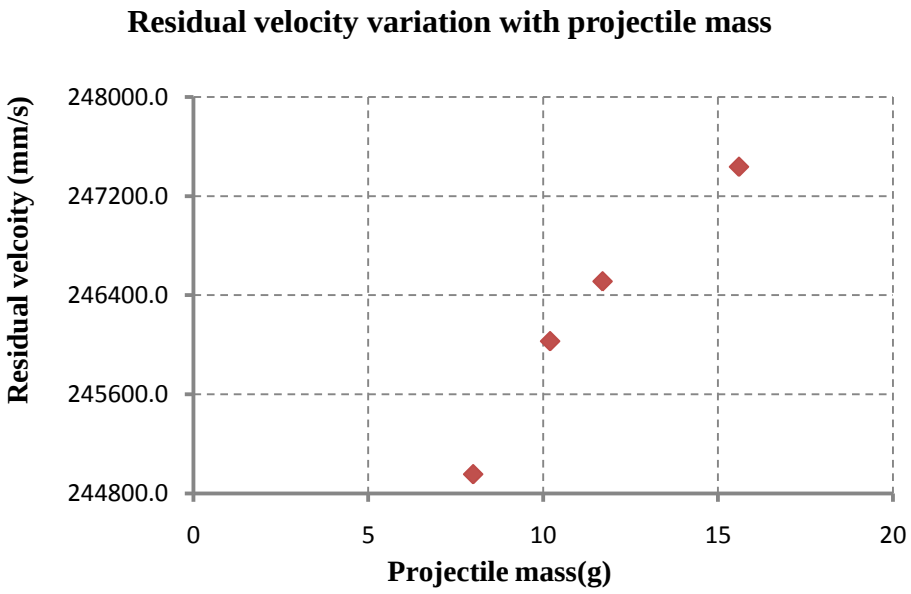

Figure 4-17 Residual velocity as a function of projectile mass

4.2.3 Test series III: simulation for three projectile shapes at impact velocity of 332 m/s

The shape of the projectile, most importantly, the projectile nose angle, has a considerable influence on the impact event. Talebi et al. [39] explained the fabric deformation mechanisms associated with the projectile shape and proved that the size of hole and the stress wave propagation vary significantly with changing projectile shape. Tan et al. [40] demonstrated that the fabric creasing and perforation mechanisms are highly dependent on the shape of the projectile. It is generally observed that sharp nosed

projectiles can penetrate fabrics easily by shearing across yarns thickness. Figure 4-18 shows the three projectile shapes under consideration.

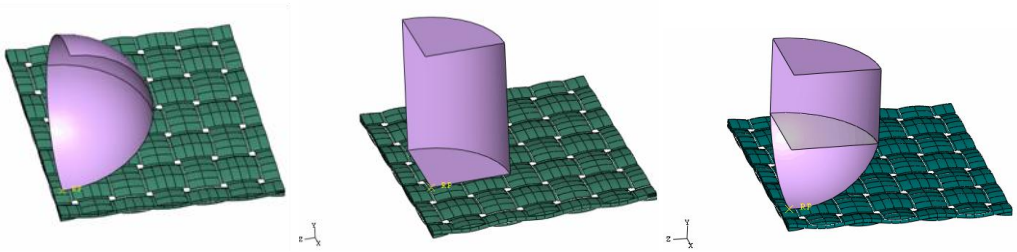

Spherical Cylindrical Hemi-spherical

Figure 4-18 Three projectile shapes used for simulation

Figure 4-19 depicts the transverse deformation of the fabric upon impact by a hemi-spherical projectile.

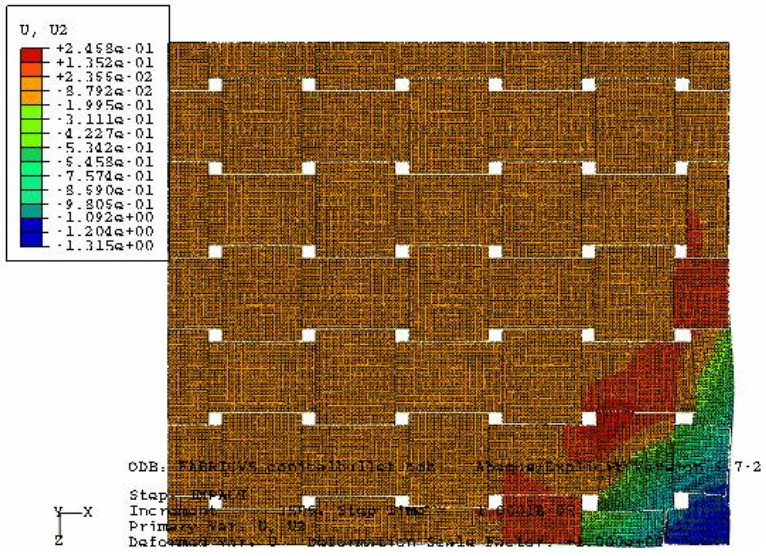

$t = 10\mu s$

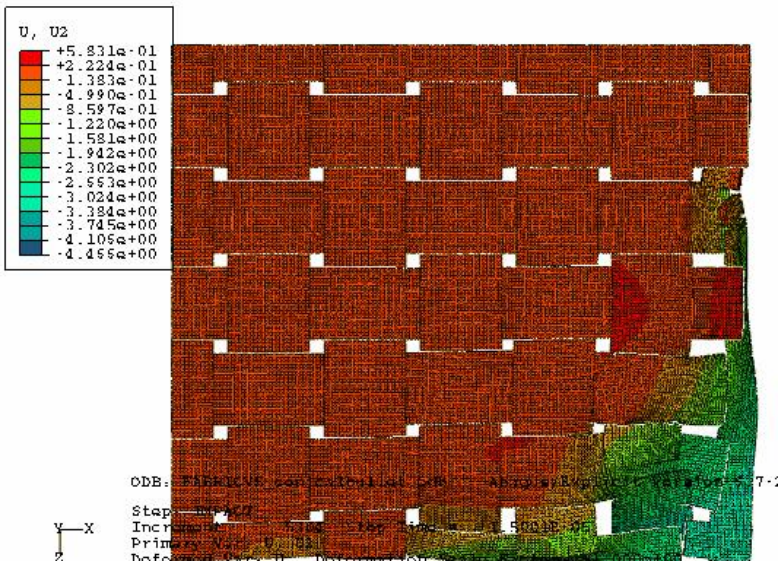

$t = 15\ \mu s$

Figure 4-19 Fabric deformation for a hemi-spherical projectile

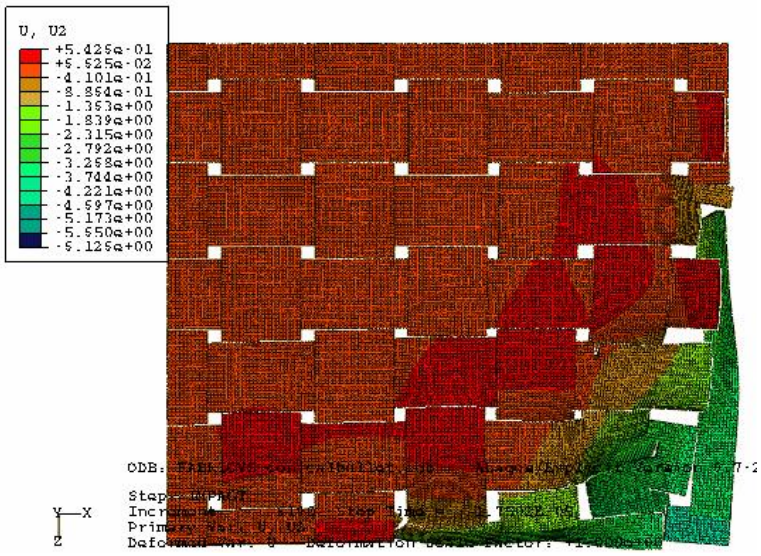

$t = 17.5$ μs

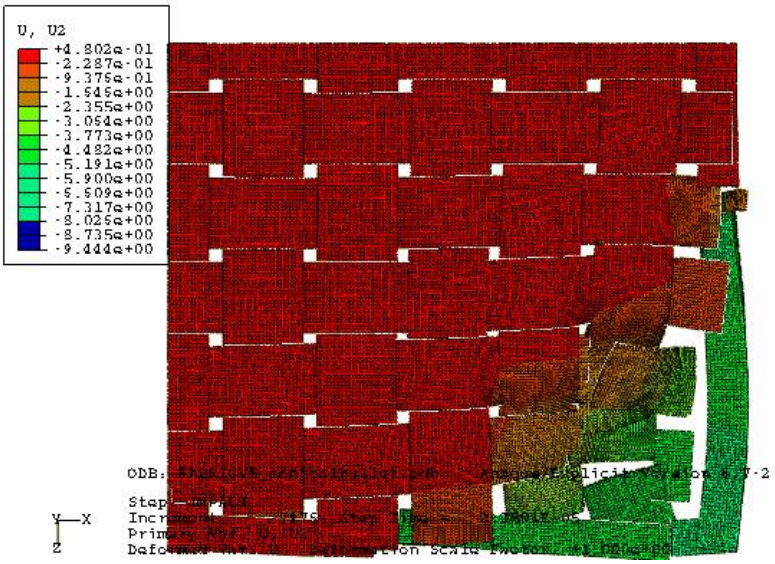

$t = 22.5$ μs

Figure 4-19 Continued

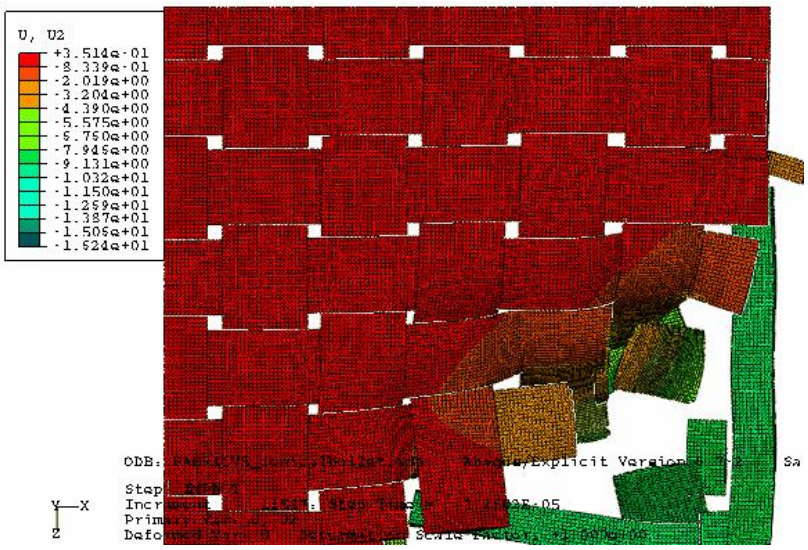

$t = 32.5$ μs

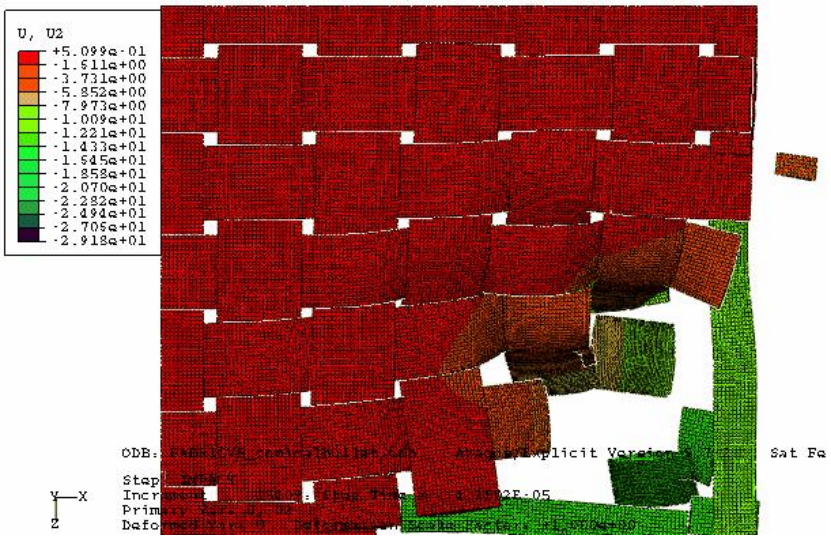

$t = 40$ μs

Figure 4-19 Continued

Figure 4-20 depicts the transverse deformation characteristics of the fabric impacted by a spherical projectile.

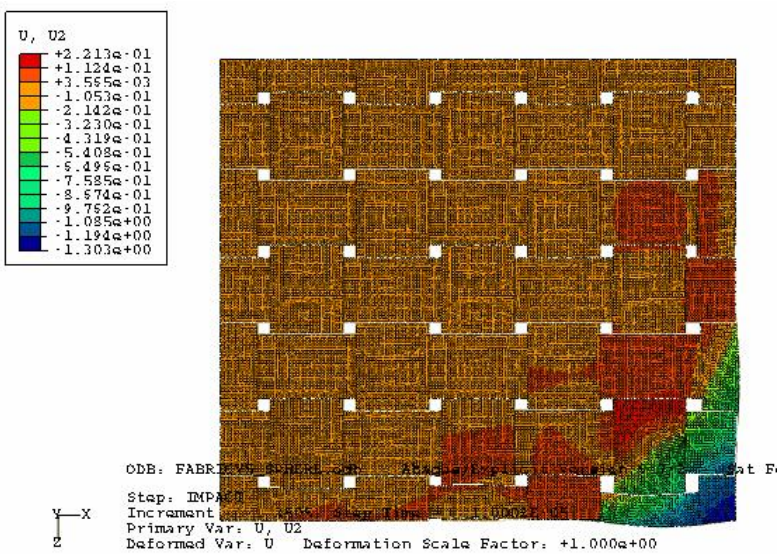

$t = 10$ μs

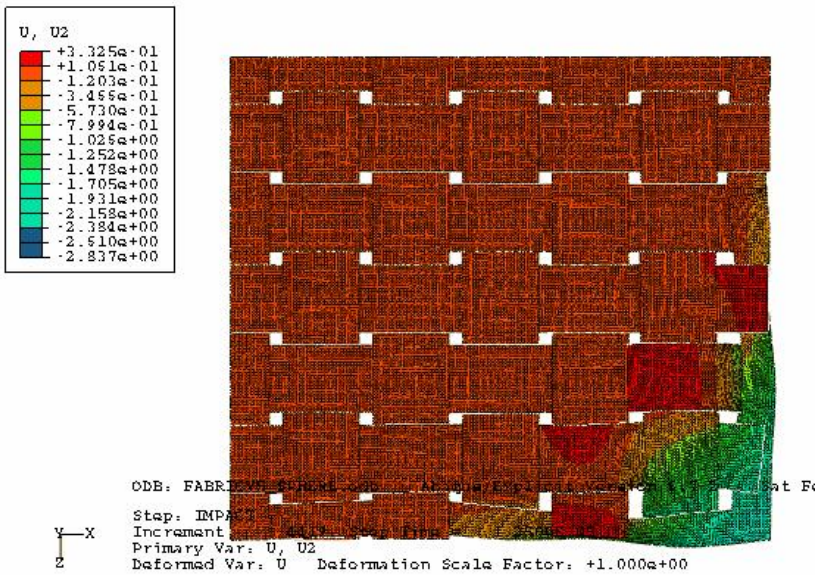

$t = 15$ μs

Figure 4-20 Fabric deformation for a spherical projectile

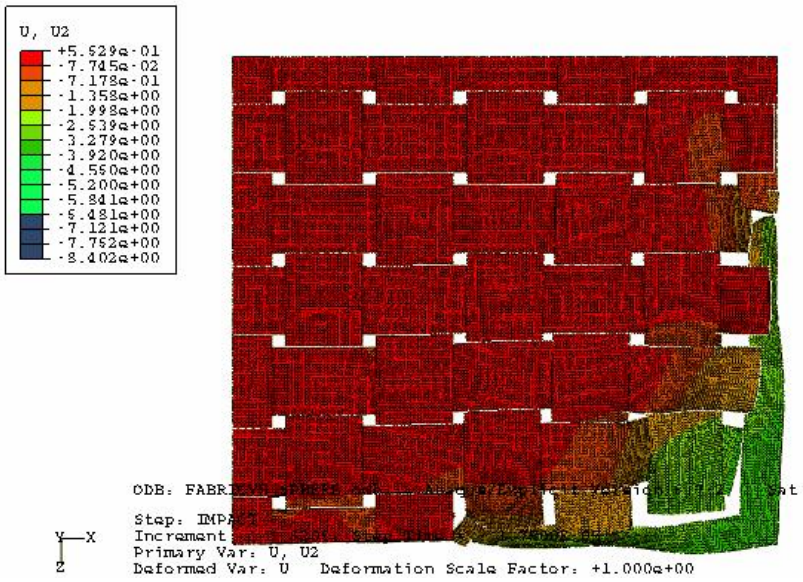

$t = 17.5$ μs

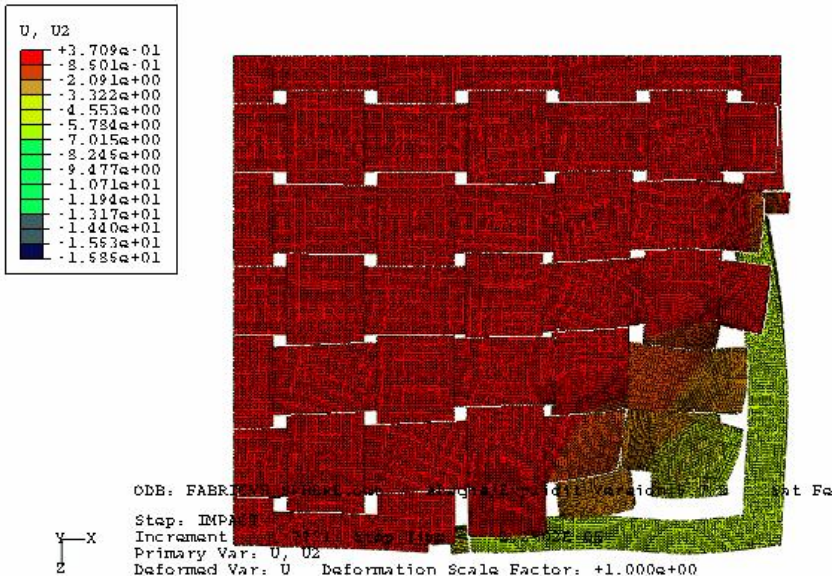

$t = 22.5$ μs

Figure 4-20 Continued

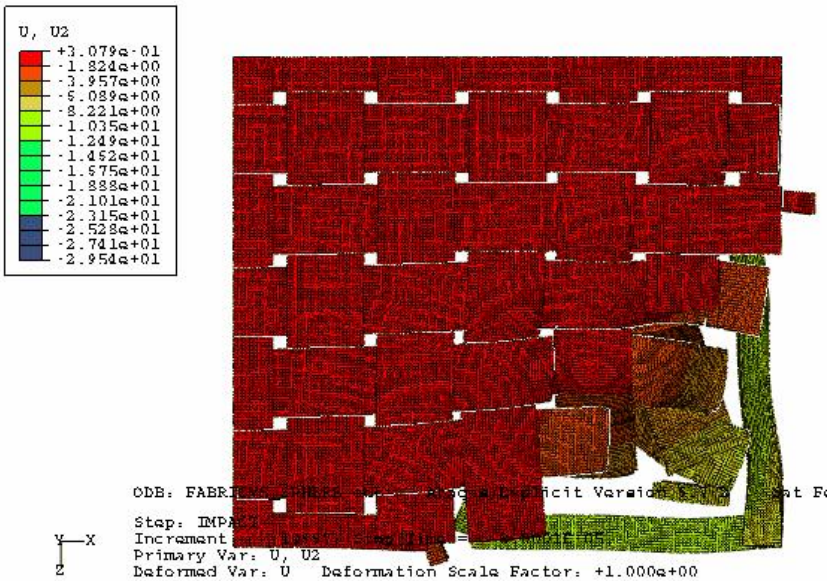

$t = 32.5$ μs

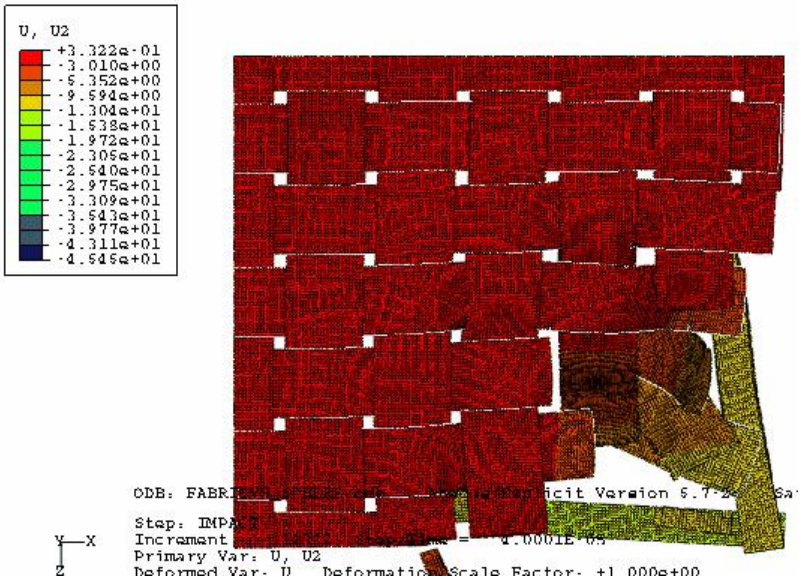

$t = 40$ μs

Figure 4-20 Continued

Figure 4-21 shows the transverse deformation of the fabric impacted by a cylindrical projectile.

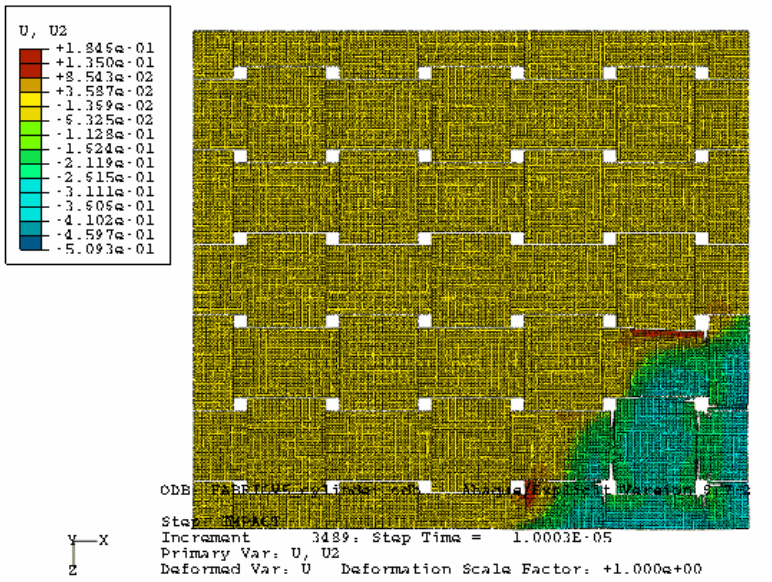

$t = 10$ μs

Figure 4-21 Fabric deformation for a cylindrical projectile

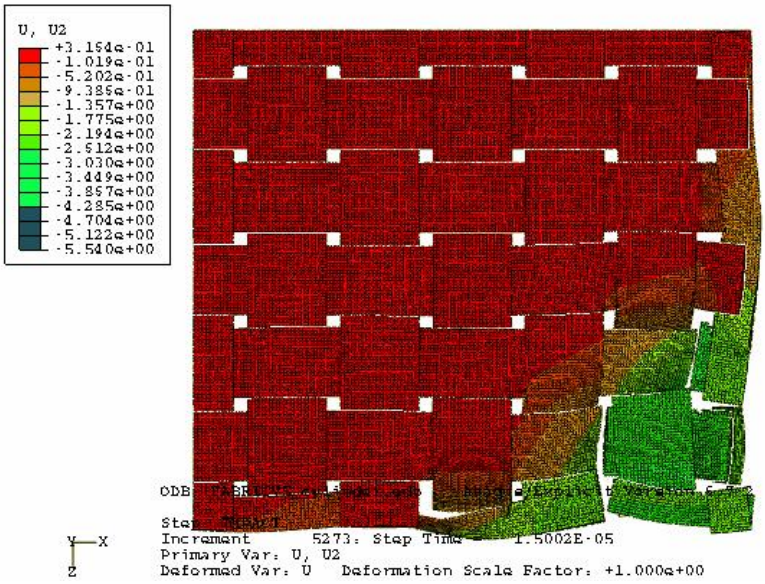

$t = 15$ μs

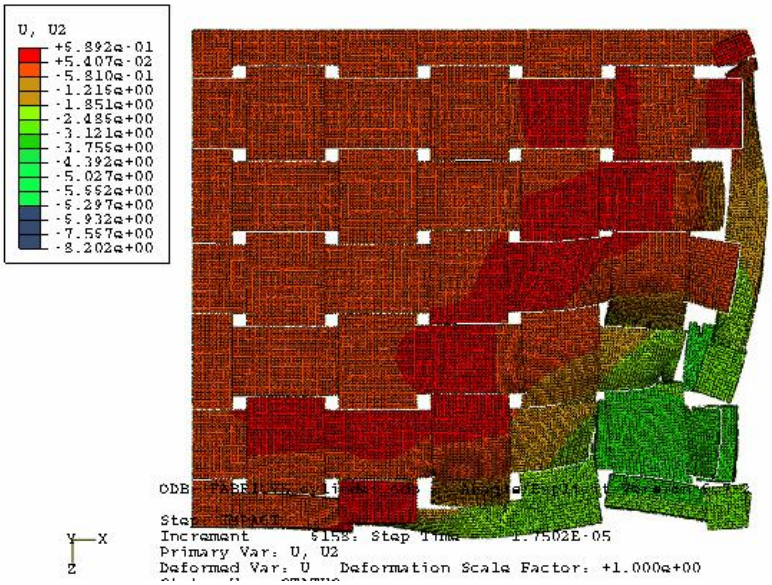

$t = 17.5$ μs

Figure 4-21 Continued

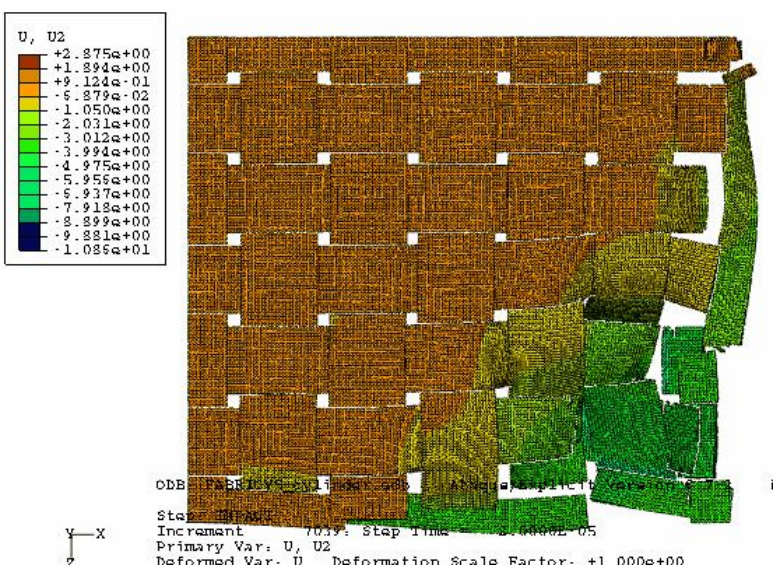

$t = 22.5$ μs

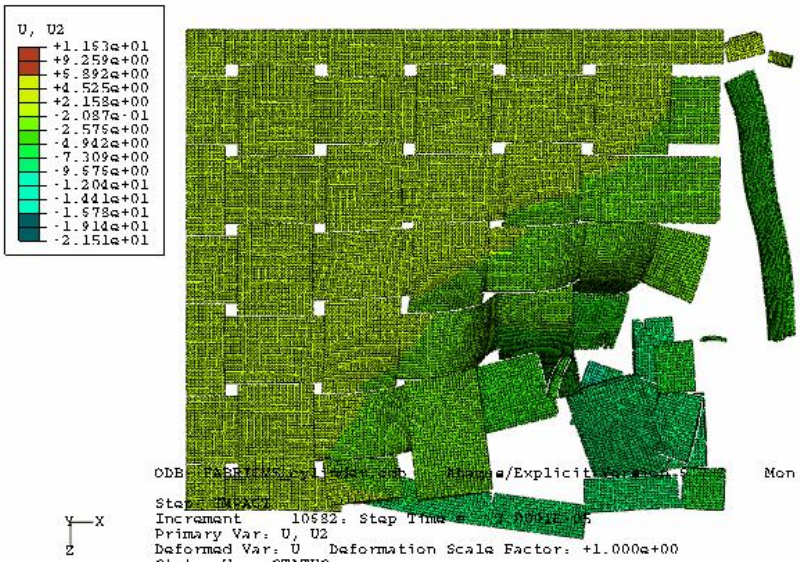

$t = 32.5$ μs

Figure 4-21 Continued

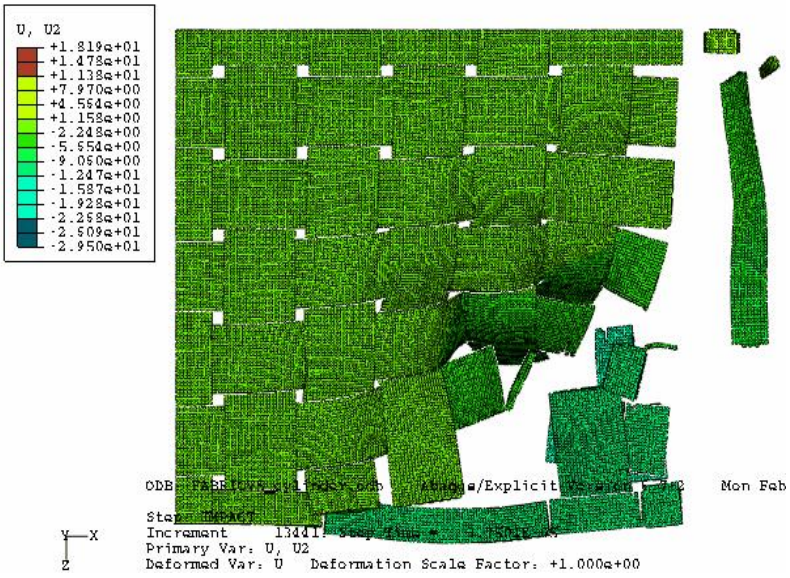

$t = 40$ μs

Figure 4-21 Continued

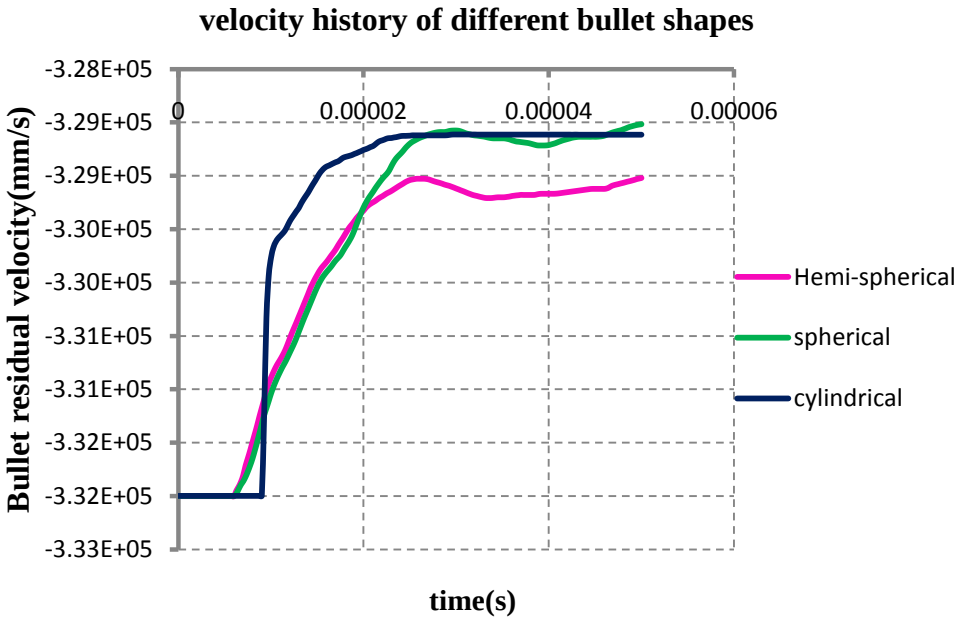

Figure 4-22 Residual velocity of the projectile with different shapes

Figure 4-22 and Figure 4-23 show the bullet residual velocity history and loss in kinetic energy after the impact respectively.

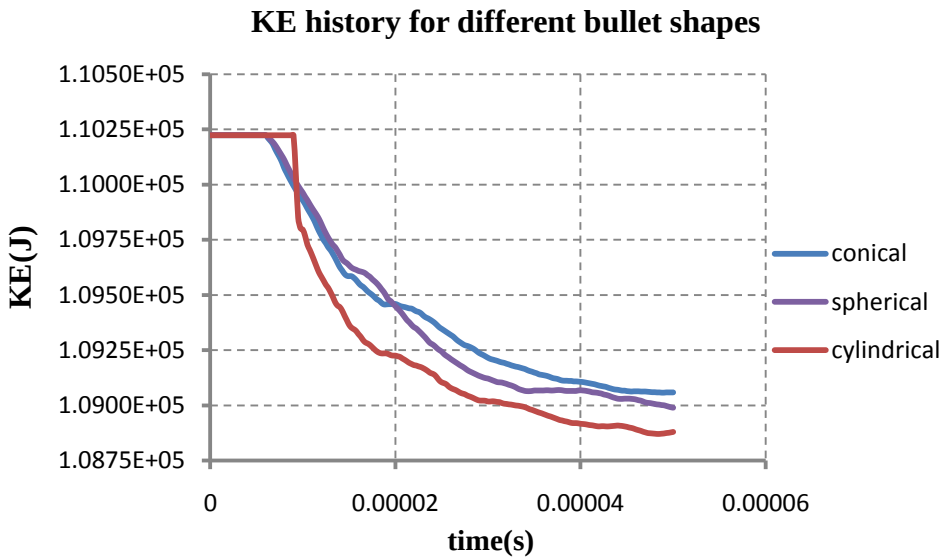

Figure 4-23 Kinetic energy lost by the projectile

Figure 4-24 depicts the strain energy rise in the target fabric.

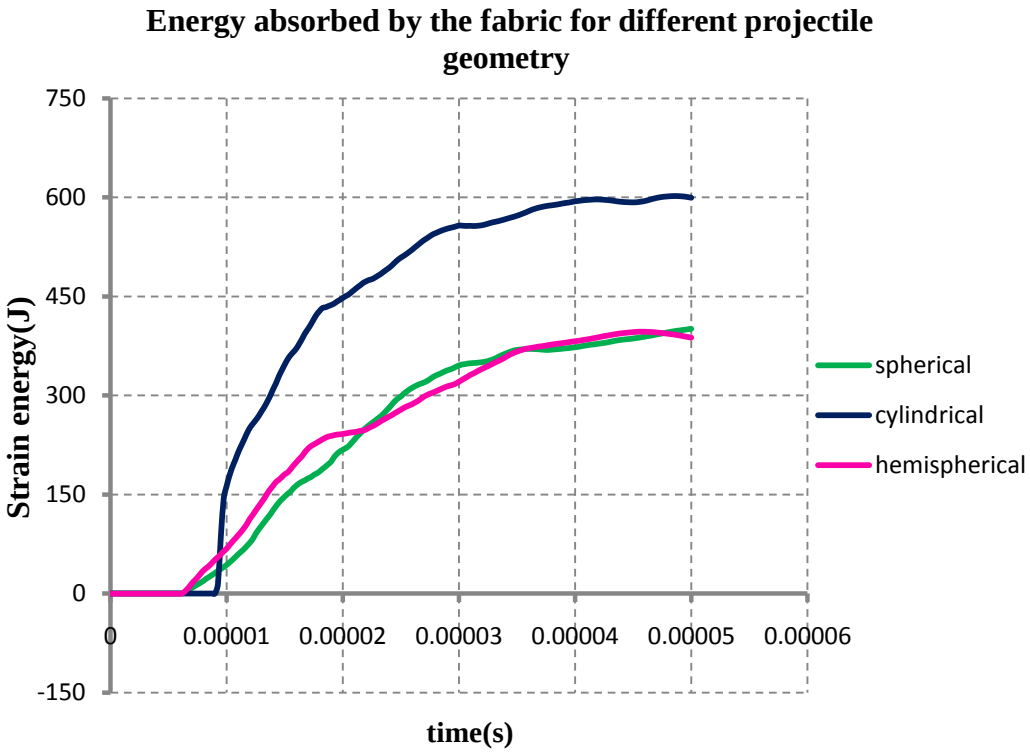

Figure 4-24 Strain energy rise in the fabric for different projectile shapes

Observations

For a projectile with lesser nose angle, such as the hemispherical and spherical projectiles, wedging-through phenomenon is predominant. Since the fabric is loosely woven, the projectile can easily slip through the opening or 'wedge' and hence leaves the fabric by pushing aside the yarns rather than breaking them. From Figure 4-19 bowing can also be seen, which refers to the condition where weft and warp yarns are non-orthogonal.

The profile of the projectile velocity history is much smoother for the hemispherical and spherical projectiles than for the blunter cylindrical projectile. The blunter the projectile is, the greater is the diameter of the hole formed. Also, for a blunt

projectile, like the cylindrical geometry, there is a greater area in contact at the time of impact, hence causing the projectile to decelerate faster. Due to its round shape the spherical projectile is in contact with the fabric for more time than the hemispherical and the cylindrical projectiles. Figure 4-25 shows the variation in contact force for two of the three projectile shapes.

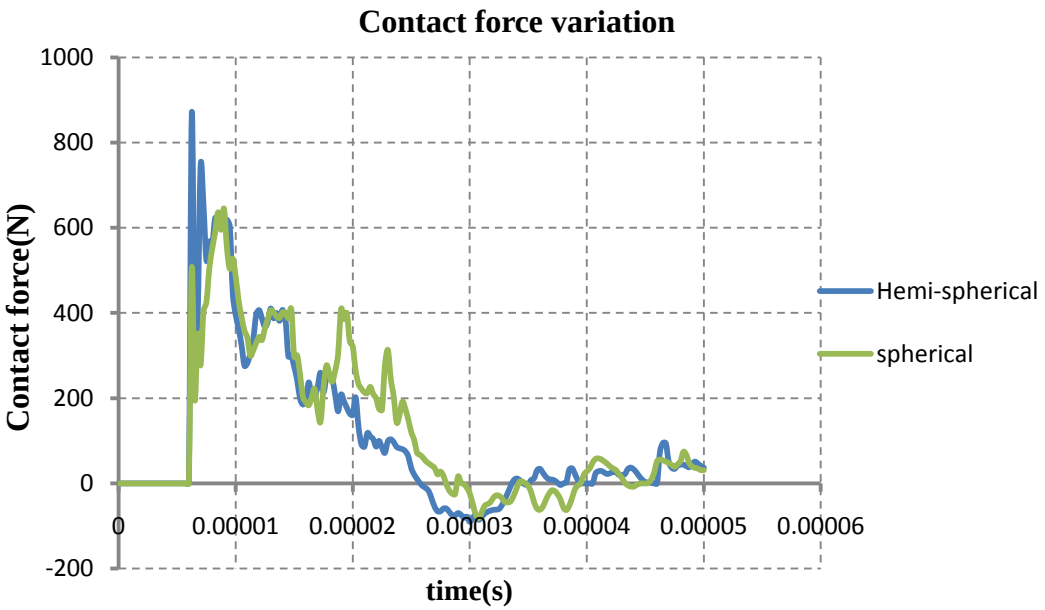

Figure 4-25 Contact force history for spherical and hemi-spherical projectiles

From Figure 4-23 and Figure 4-24 it can be observed that the energy absorbed by the fabric and the energy lost by the projectile are the highest for the cylindrical projectile, on account of the greater contact area and hence more yarns absorbing the impact energy.

4.2.4 Test series IV: simulation for different gripping conditions

The far-field gripping conditions play an important role in the impact characteristics. Chitrangad [41] observed that the ballistic performance is the best when an aramid fabric is maintained under tension. It was observed that when the fabric is gripped on all four edges, local yarn failure at the sharpest edge of the projectile is observed. Also, for the four edge case the contact force on the projectile drops abruptly to zero after perforation. In the case of the two edges clamped, several other mechanisms are observed [42]. Other than the local yarn failure, yarn pullout was observed, where yarns along the unclamped ends which are free to move are pulled out without breaking. Simulations are carried out for two different boundary conditions,i.e., (a) all four edges clamped, and (b) Two edges clamped at two different impact velocities for 100 m/s and 332 m/s.

Case 1: Impact velocity of 100 m/s for the two gripping conditions

Figure 4-26 and Figure 4-27 show the transverse deformation profile for the case of all four edges clamped and two edges clamped respectively at an impact velocity of 100 m/s.

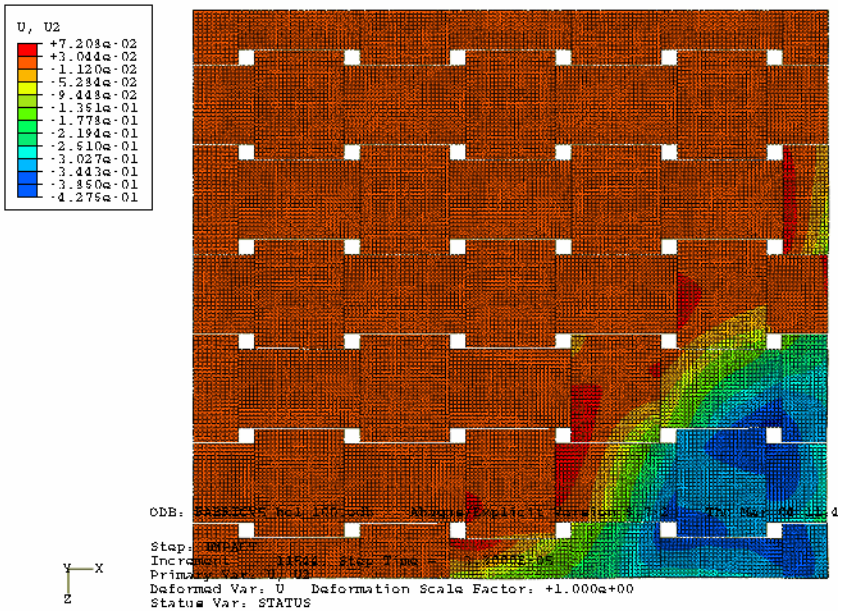

$t = 30$ μs

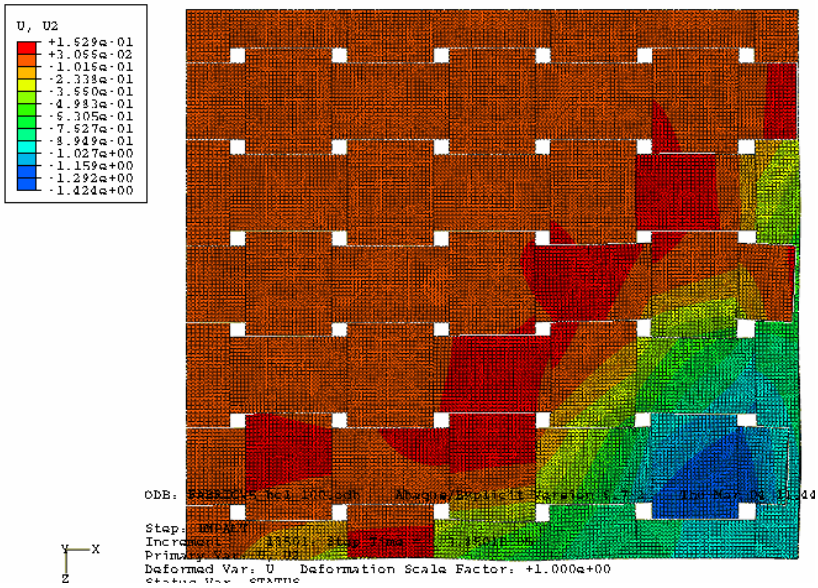

$t = 37.5$ μs

Figure 4-26 Transverse displacement of the fabric at a low impact velocity of 100 m/s for the case of all four edges clamped

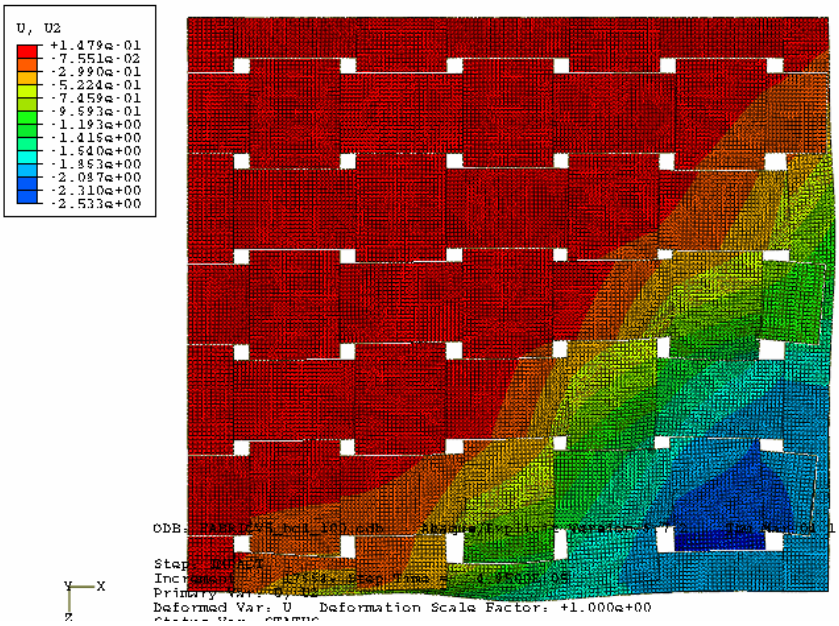

$t = 50$ μs

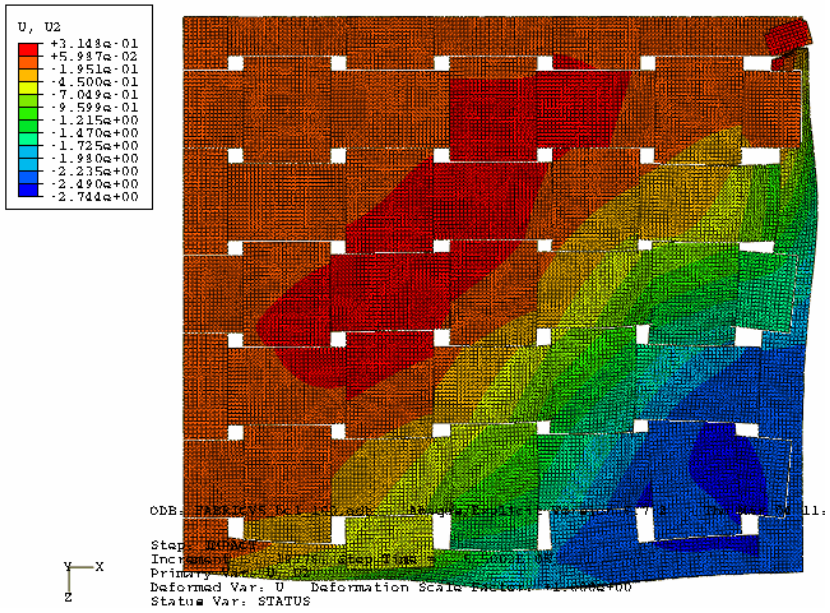

$t = 57.5$ μs

Figure 4-26 Continued

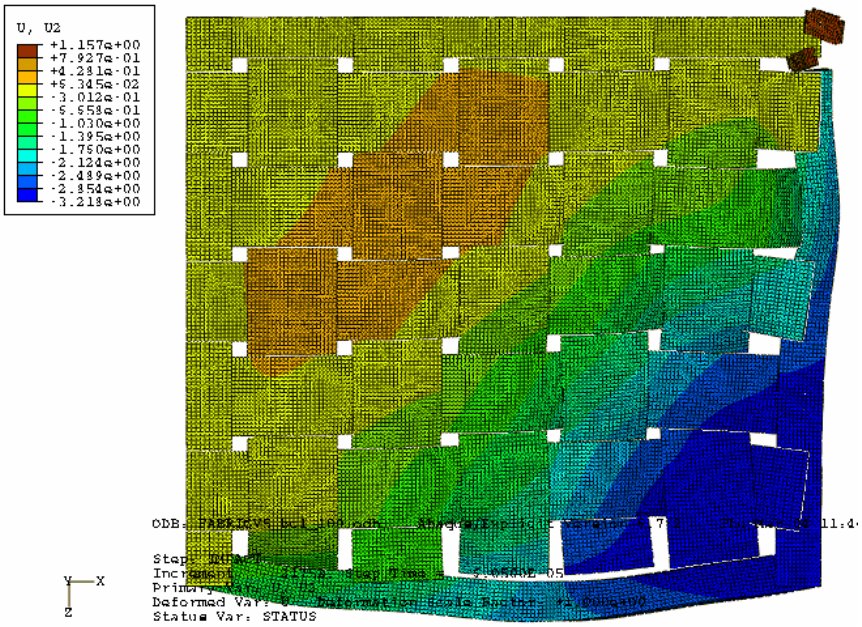

$t = 62.5$ μs

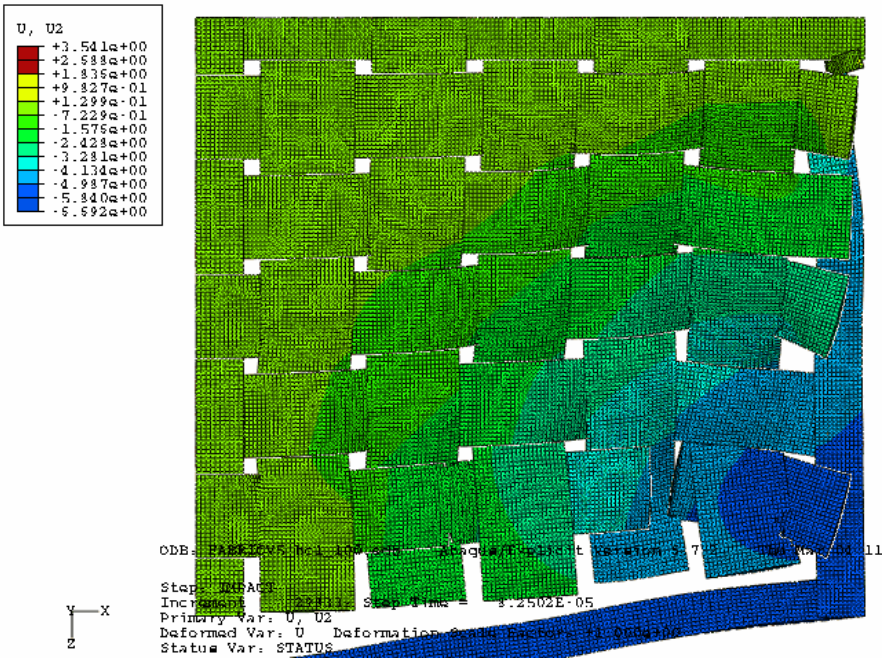

$t = 80$ μs

Figure 4-26 Continued

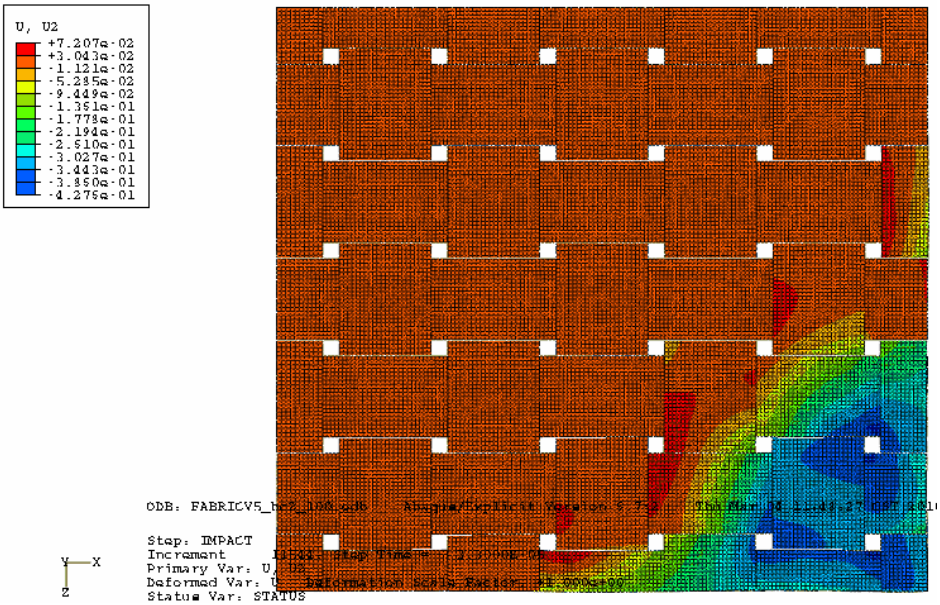

$t = 30$ μs

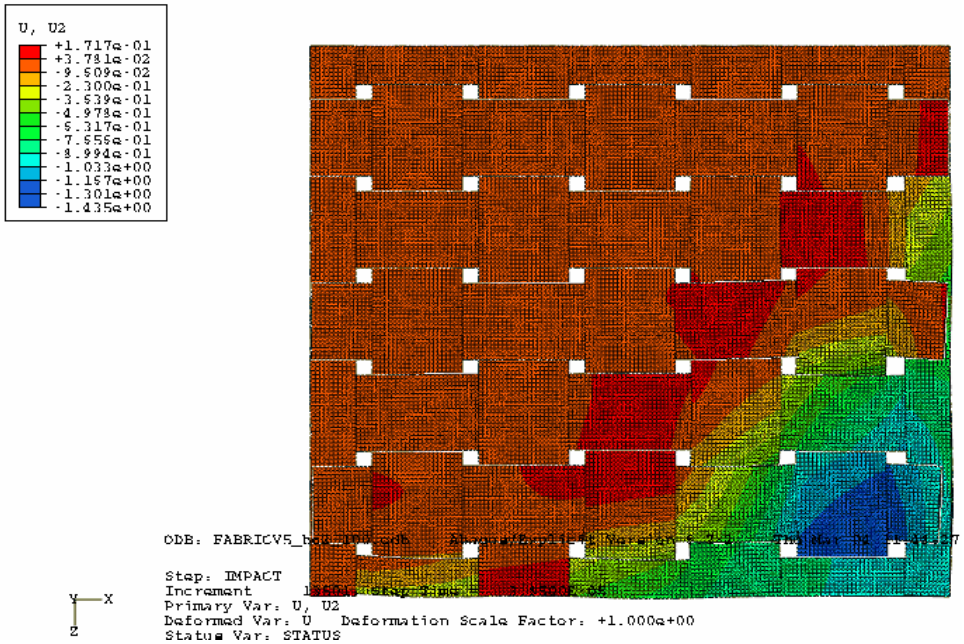

$t = 37.5$ μs

Figure 4-27 Transverse displacement of the fabric at a low impact velocity of 100 m/s for the case of two edges clamped

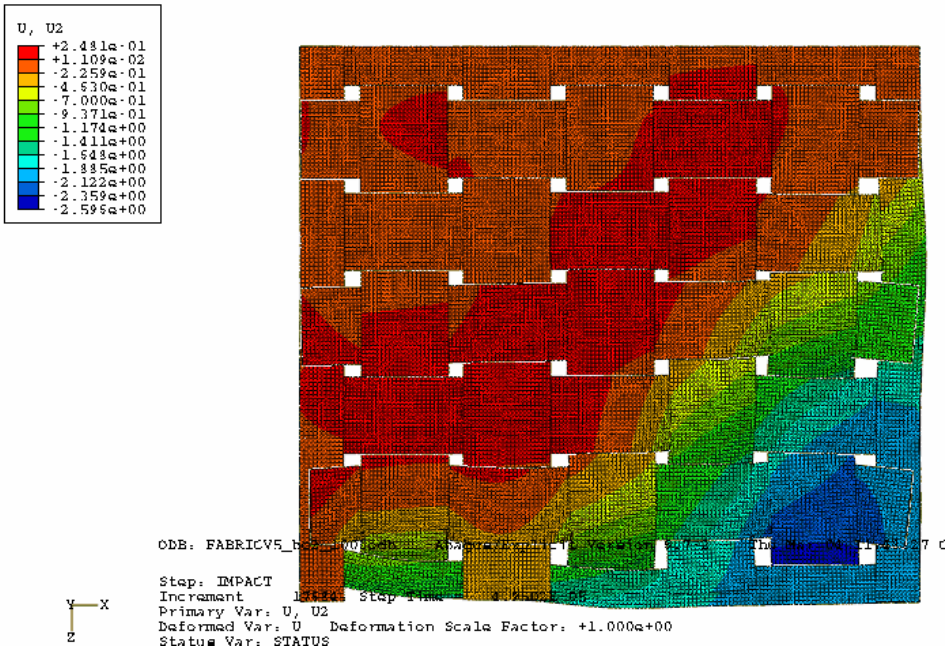

$t = 50$ μs

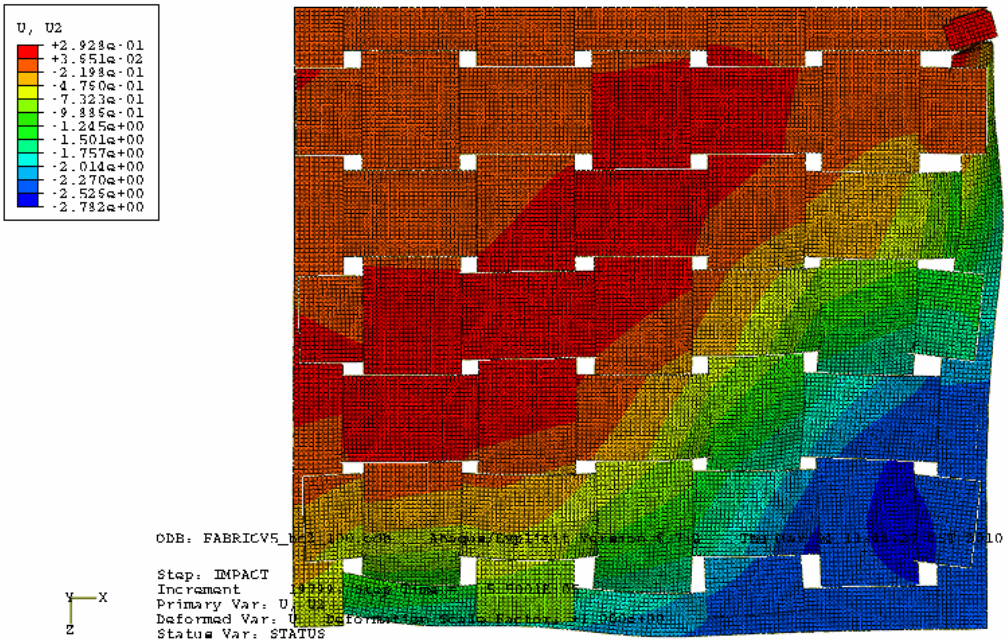

$t = 57.5$ μs

Figure 4-27 Continued

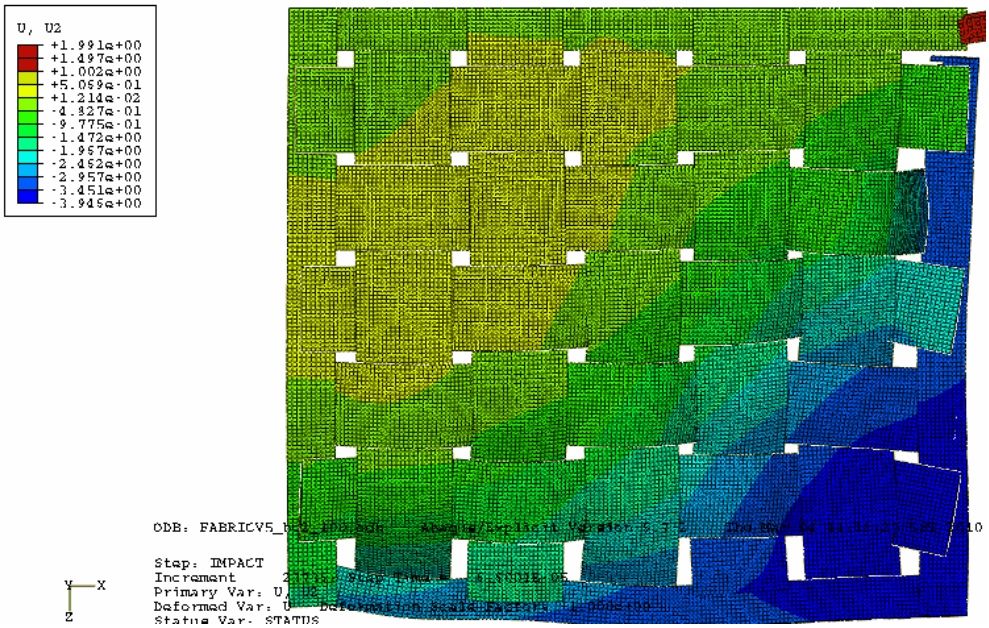

$t = 62.5$ µs

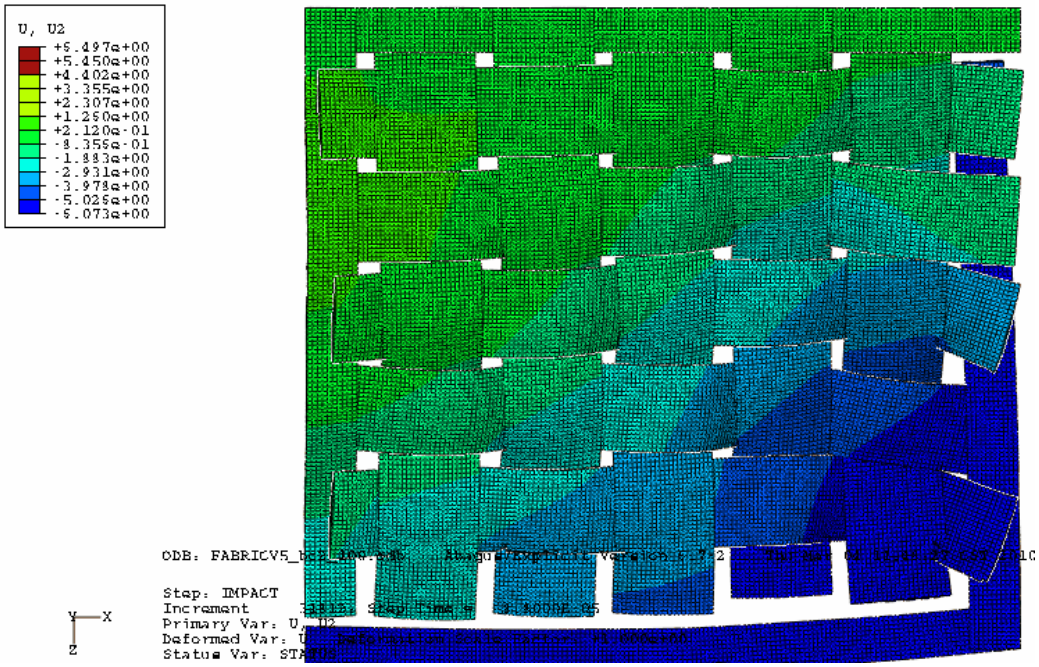

$t = 80$ µs

Figure 4-27 Continued

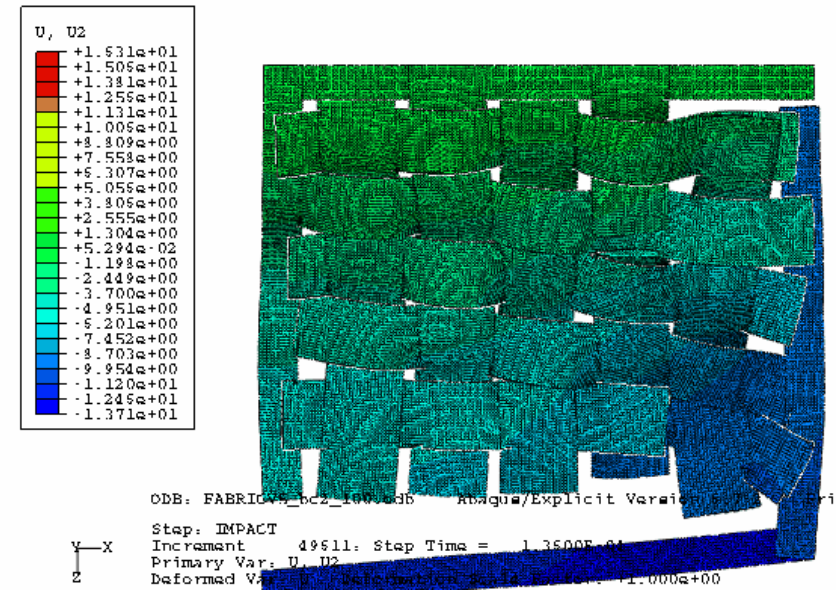

$t = 135$ μs

Figure 4-27 Continued

Figure 4-28 and Figure 4-29 show the kinetic energy lost by the projectile and the energy absorbed by the fabric for the two gripping conditions for the impact velocity of 100 m/s.

`

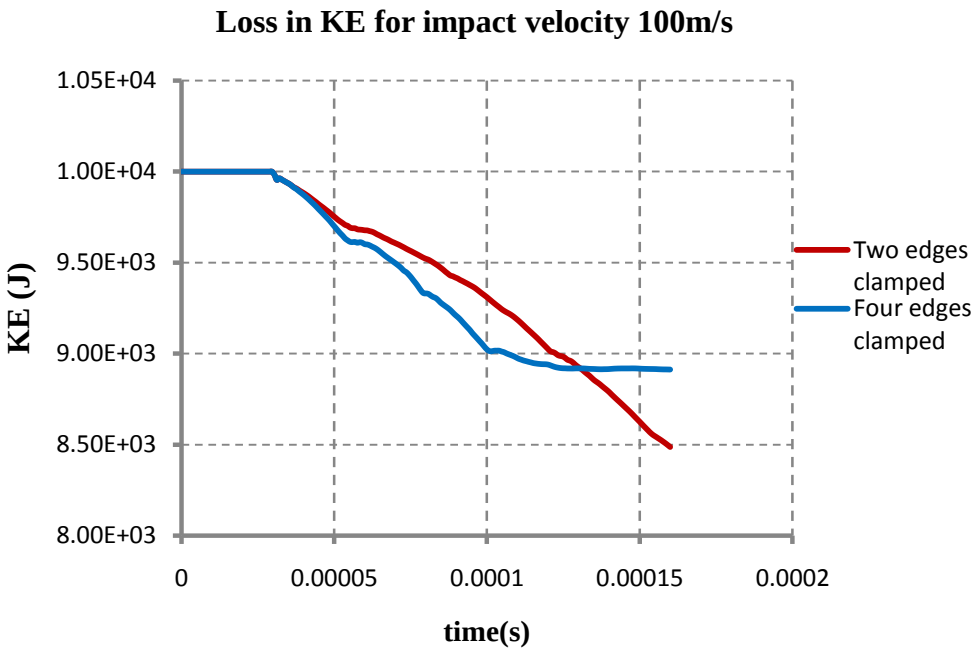

Figure 4-28 Kinetic energy lost by the projectile at the impact velocity of 100 m/s

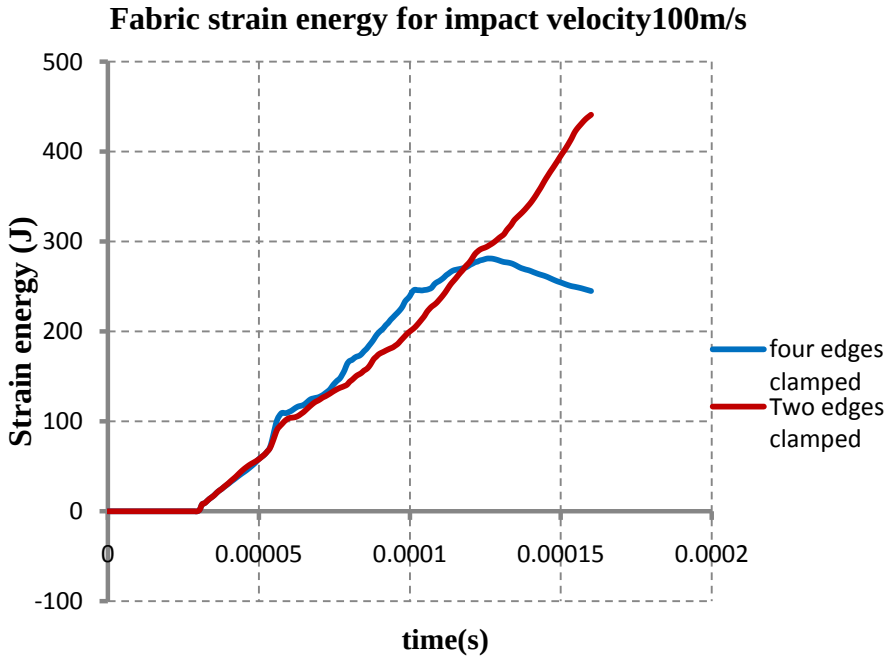

Figure 4-29 Strain energy gained by the fabric at the impact velocity of 100 m/s

Case 2: Impact velocity of 332 m/s for the two gripping conditions

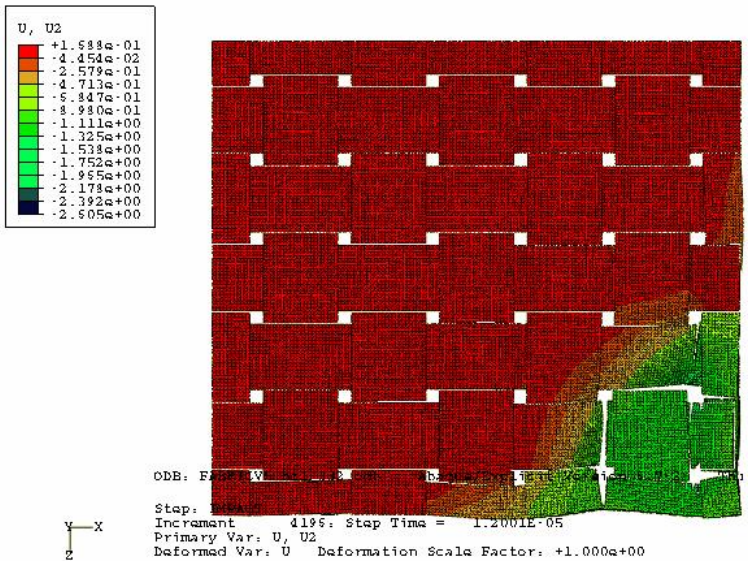

t = 12 μs

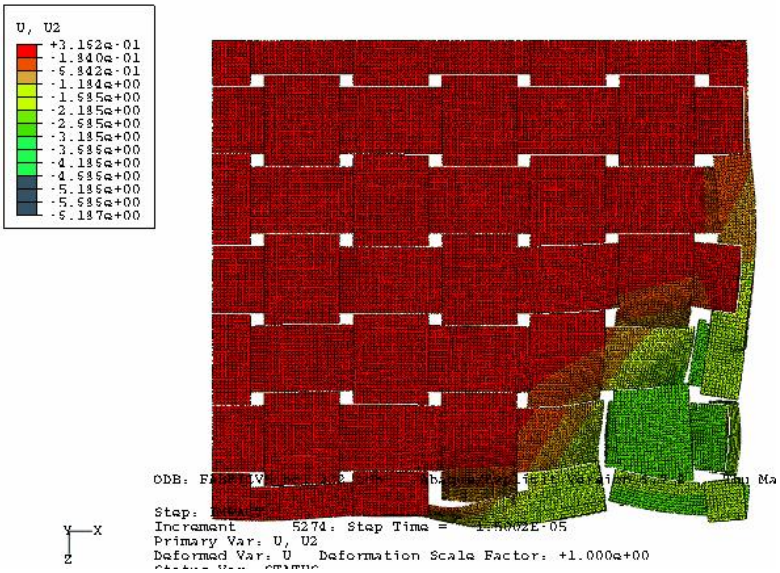

t = 15 μs

Figure 4-30 Transverse displacement of the fabric at a high impact velocity of 332 m/s for the case of all four edges clamped

$t = 21$ μs

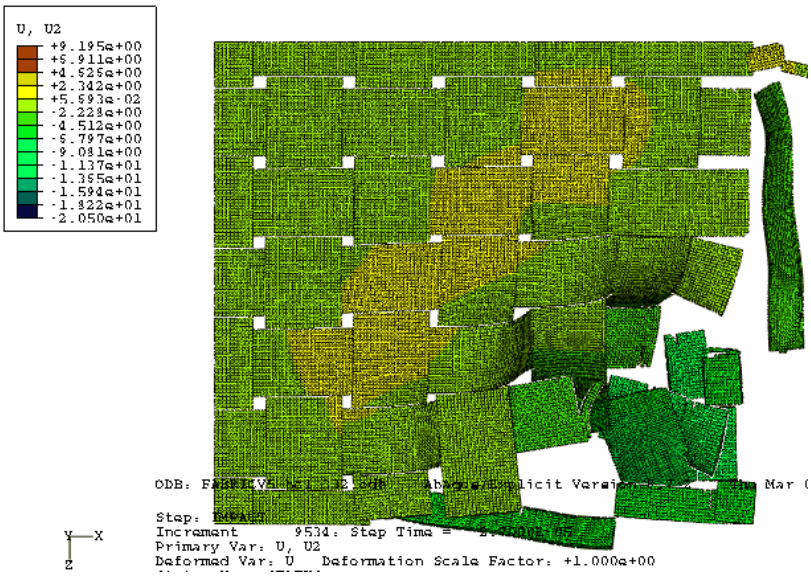

$t = 27$ μs

Figure 4-30 Continued

Figure 4-30 shows the fabric deformation history for all four edges clamped at an impact velocity of 332 m/s. Figure 4-31 shows the fabric deformation history for two edges clamped at an impact velocity of 332 m/s.

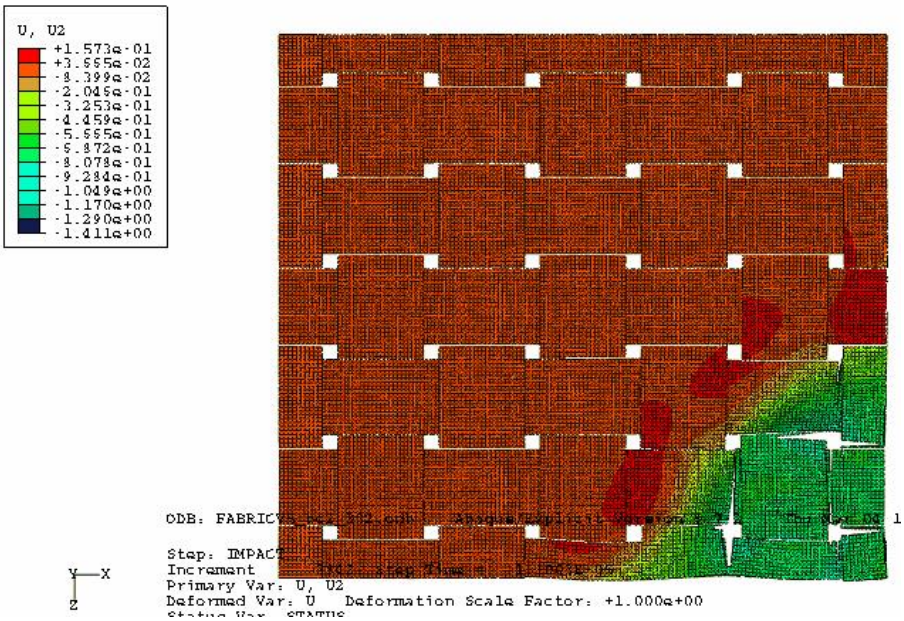

t = 11 μs

Figure 4-31 Transverse displacement of the fabric at a high impact velocity of 332 m/s for two edges clamped

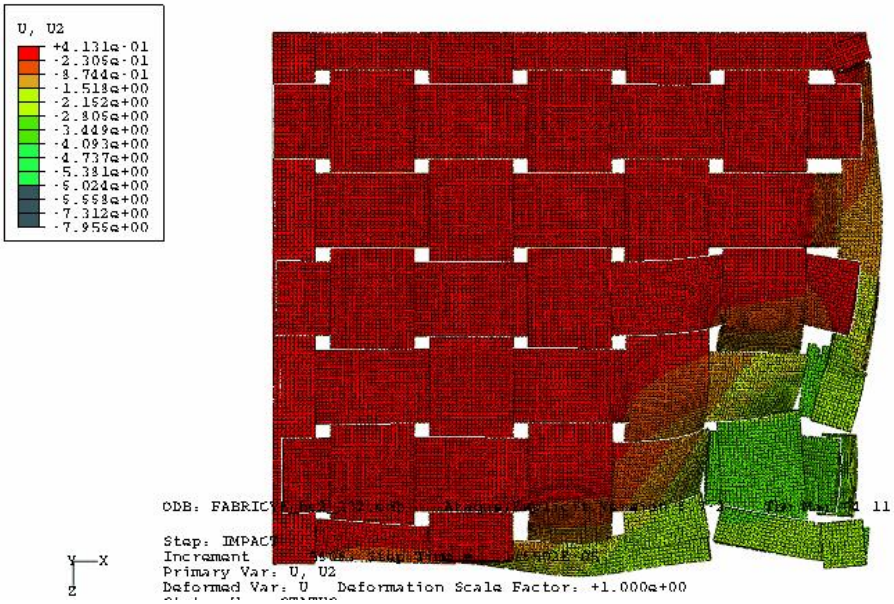

t = 15 μs

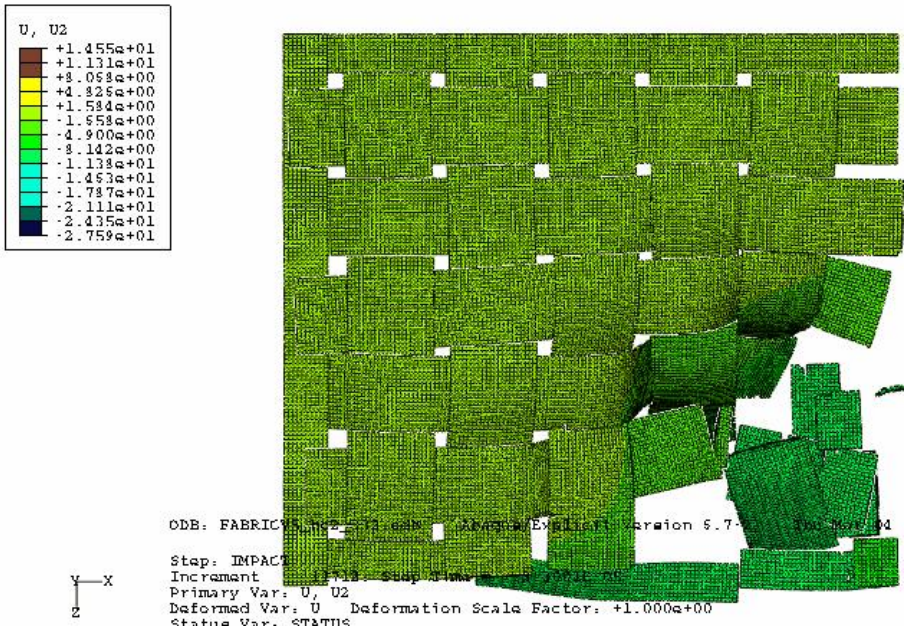

t = 33 μs

Figure 4-31 Continued

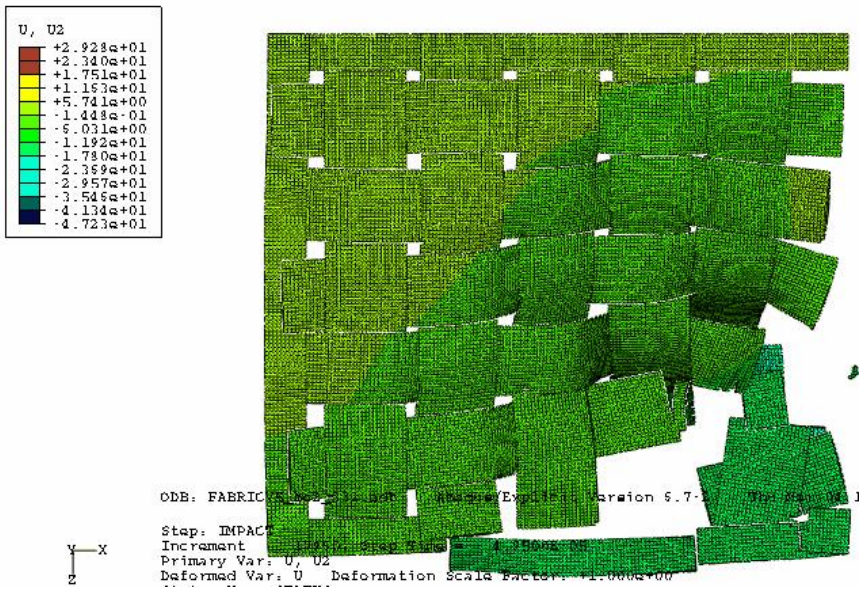

$t = 50$ μs

Figure 4-31 Continued

Figure 4-32 and Figure 4-33 show the kinetic energy lost by the projectile and the energy absorbed by the fabric for the two gripping conditions for the impact velocity of 332 m/s.

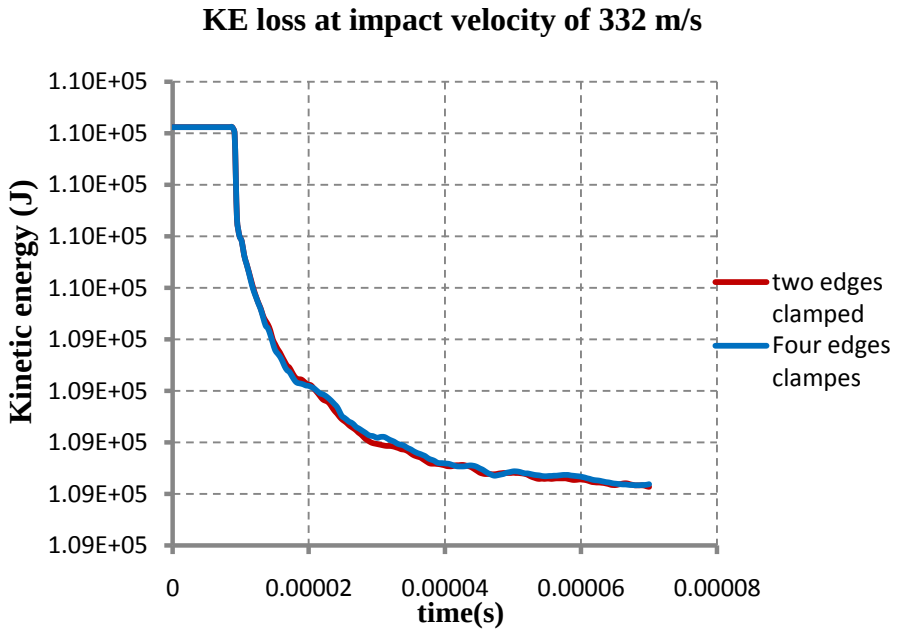

Figure 4-32 Kinetic energy lost by the projectile at the impact velocity of 332 m/s

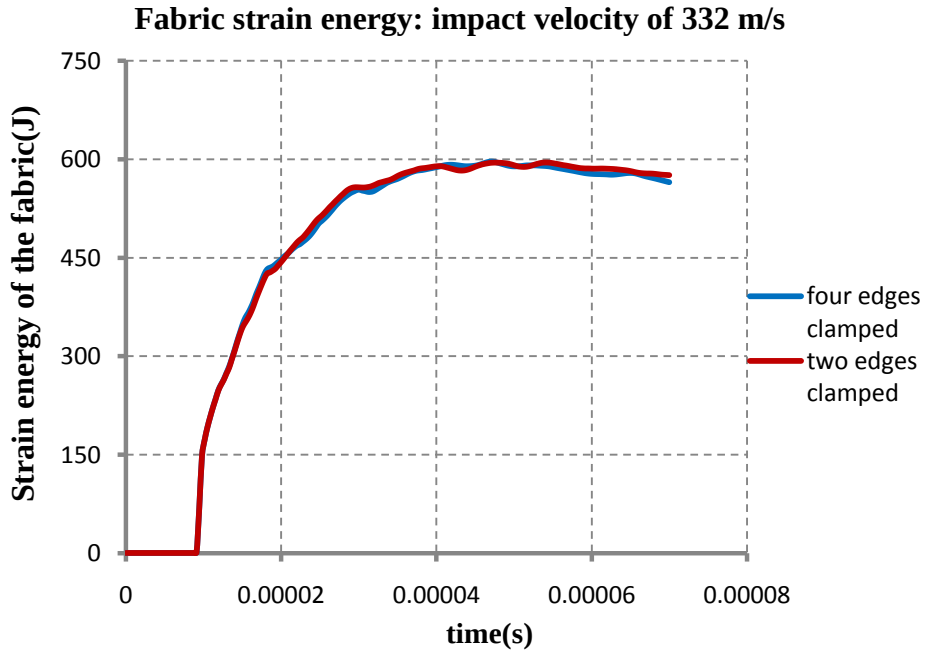

Figure 4-33 Strain energy gained by the fabric at the impact velocity of 332 m/s

Observations

Two different trends are observed for the two velocity cases. At the lower speed impacts the fabric clamped at two edges shows better energy absorption capabilities than that clamped on all four edges. However, at the higher impact velocity, the fabric with all four edges clamped absorbs slightly higher energy than that with two edges clamped.

It is clearly seen that the difference in energy absorbed by the fabric is more pronounced in the case of low velocity impact. This is because at low velocities the fabric has sufficient time to stretch, which creates high tension at the clamped edges. This effect is more pronounced in the case of low impact speeds. As the impact velocity is increased, the fabric penetration occurs even before the stress wave propagates to the boundaries. At low impact velocities, the fabric with two edges clamped absorbs more energy than the fabric with all four edges clamped. This can be explained as follows: the energy dissipation process is a net effect of fabric strain energy gain and the kinetic energy loss associated with the transverse motion of the fabric at the impact region. For the fabric with two clamped edges, due to yarn pull-out at the free edges, the fabric is free to undergo a transverse displacement. Hence the fabric kinetic energy is much higher than that in the case where all the four edges are restricted. For the latter, the strain energy is much higher.

The difference in the time taken for penetration is another reason for the difference in the energy absorbed. Stress waves originating from the impact point are reflected from the clamped edges or are converted into kinetic energy of the fabric due to the inward movement of the fabric material at the unclamped edges. For the all edges

clamped case, the stress waves are significantly amplified after their reflection from boundaries, thereby promoting early damage.

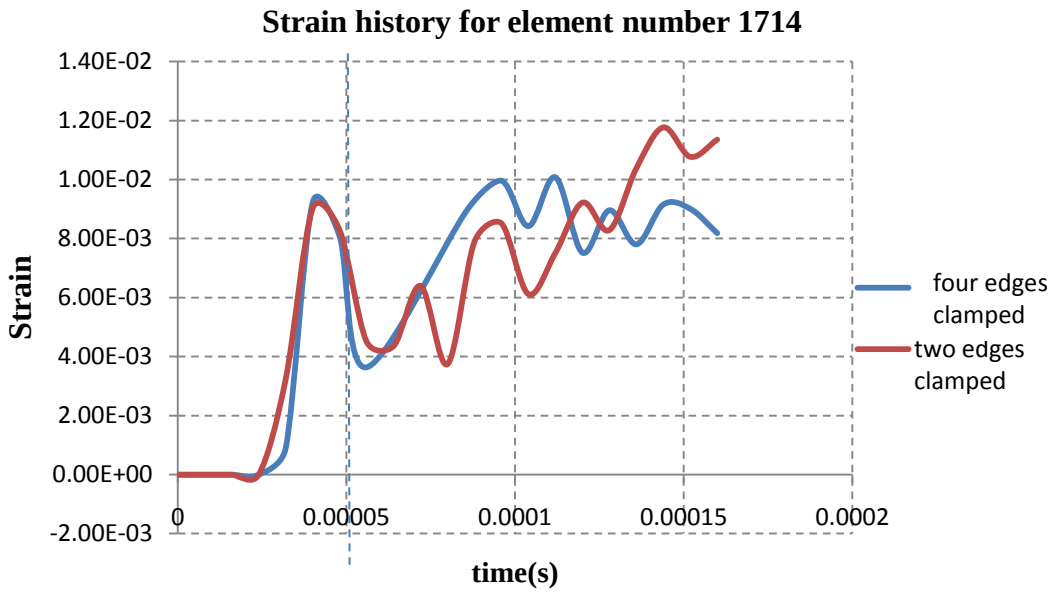

Figure 4-34 Strain history for element 1714 for the two gripping conditions

This can be seen in Figure 4-34 where the strain history of element 1714 near the impact region is plotted. At 5 μs after the impact, when the stress waves are reflected back from the clamped edges, the strain increases at a high rate for the fabric with all four edges clamped. In the case of the fabric with two edges clamped, the strain increase is much gradual, and the projectile is engaged for a much longer time.

4.2.5 Test series V: simulation of 8g, hemi-spherical projectile impact for 1- , 2-, 3-, and 4- fabric layers

Shockey et al. [43] reported that an increase in the number of plies resulted in a significant increase in the amount of strain energy absorbed by the fabric system. This can be attributed to the fact that the inter-layer friction inhibits the sideways motion of the yarns in the first-hit layer, causing an increased ballistic penetration resistance. In the current study, results are obtained for four different fabric layer systems. Figure 4-35 shows the system mesh for four fabric layers.

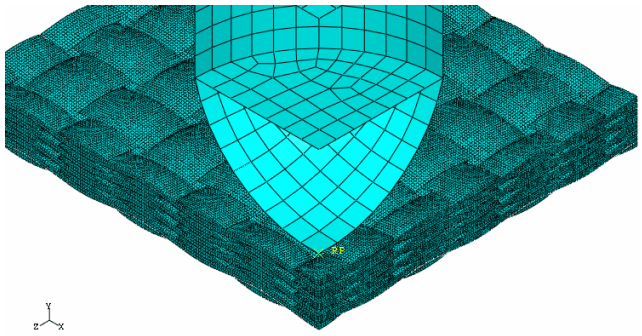

Figure 4-35 Fabric layers

Figure 4-36 shows the bullet velocity history for the1-, 2-, 3- and 4- fabric layer cases. The residual velocities for the four cases are listed in Table 4-9.

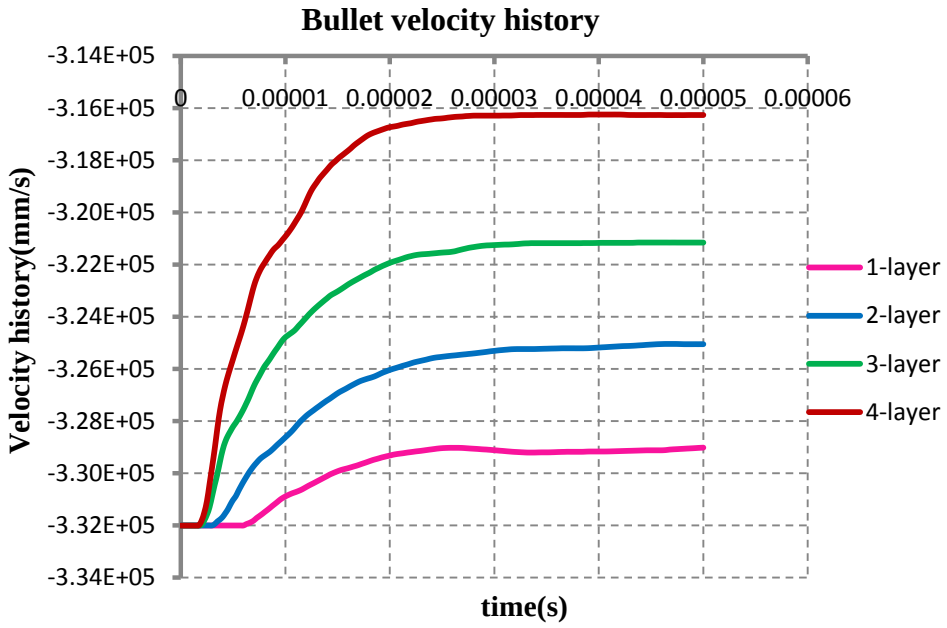

Figure 4-36 Residual velocity for different fabric layers

Table 4-9 List of residual velocities

Impact velocity(m/s)	layers	Residual velocity(m/s)
332	1	329
	2	325
	3	321
	4	316

Experimental work of Karahan et al. [44] showed that the energy absorbing capacity of fabric panels increases and the amount of energy transmitted to the back of

panels decreases with an increase in the number of fabric layers, thereby reducing the blunt trauma.

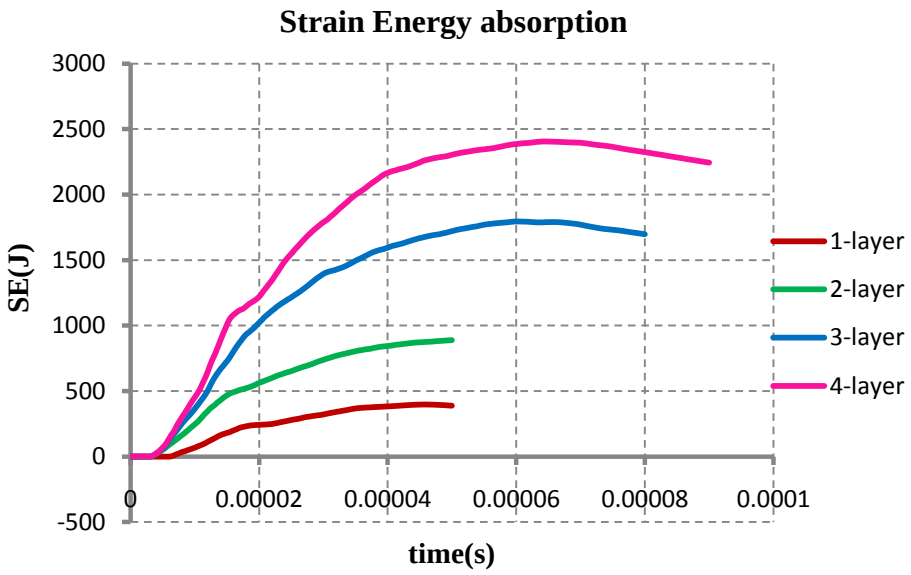

Figure 4-37 Strain energy rise in the fabric layer system

Observations

From Figure 4-37 it is observed that the fabric energy absorbing capability is proportional to the number of fabric layers. With each added layer, there is a significant decrease in the residual velocity of the projectile, as seen in Figure 4-36. With each additional layer, the percentage increase in strain energy absorbed by the fabric decreases. With an addition of a 2nd layer the percentage increase in fabric strain energy absorption is 124%. The addition of a 3rd layer increases the fabric strain energy absorption by 100%, whereas adding a 4th layer gives the increase that is just around 33%. Hence it can be concluded that the addition of fabric layers is advantageous only

to a certain extent beyond which it becomes redundant, as it makes the system bulky without adding any significant energy absorption capability.

4.2.6 Test series VI: simulations for studying frictional effects on energy absorbed by the fabric

There are three sources of friction during the ballistic impact of woven fabrics, namely yarn-yarn friction, projectile-yarn friction, and fiber-fiber friction. Experimental studies have revealed that inter-yarn friction affects the energy absorption of fabrics subjected to ballistic impact. Fabrics with high friction were observed to absorb larger amounts of energy, compared to those with lower friction .The inter-yarn friction plays a major role in the energy dissipation associated with yarn pullout. Lee et al. [42] has shown that restricting the ability of the yarn to move laterally out of the path of the projectile during impact increases the amount of energy that the fabric can absorb, i.e., increasing the friction between the projectile and the fabric and between the yarns themselves will hinder the mobility of the yarn and require the projectile to engage and break more yarns, which would result in greater energy absorption.

The variation in energy absorbed by the fabric for different friction factors ranging from 0.01 to 0.5 has been obtained. Figure 4-38 compares the fabric deformation for the two friction cases with the friction coefficient being 0.01 and 0.5 at different time instants after impact.

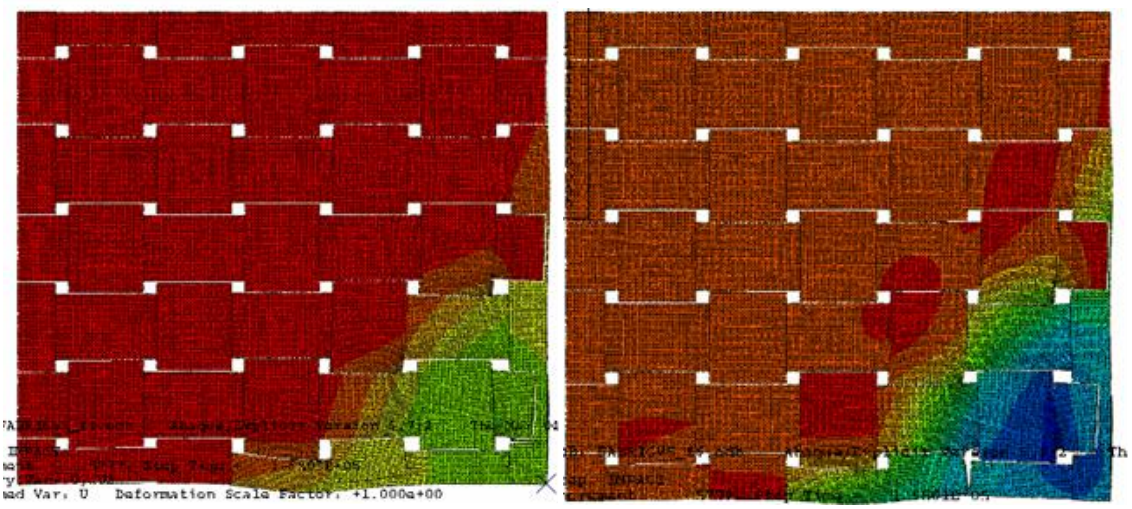

t = 16 μs

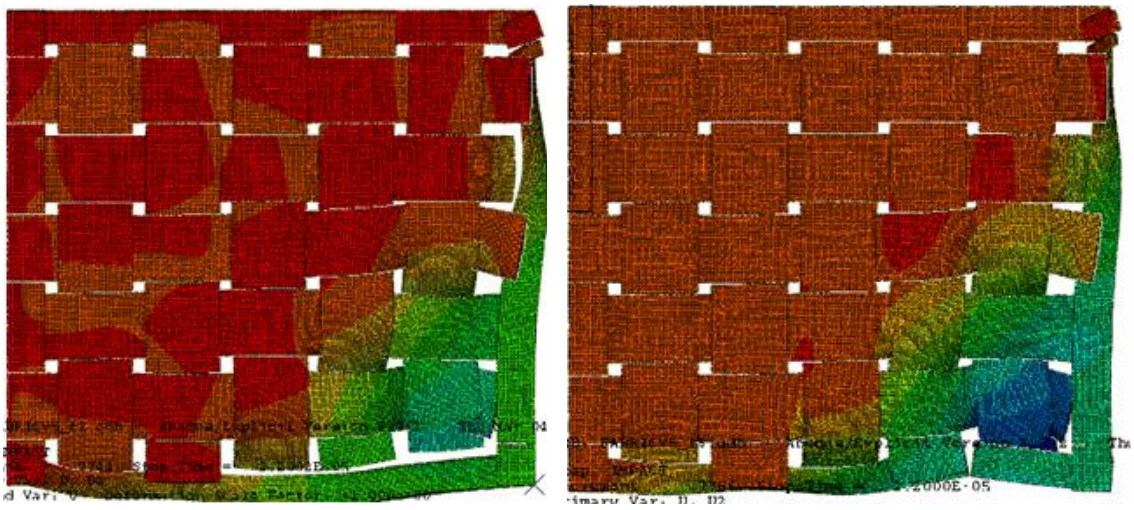

t = 22 μs

(a) (b)

Figure 4-38 Fabric deformation history for (a) f =0.01 (b) f =0.5

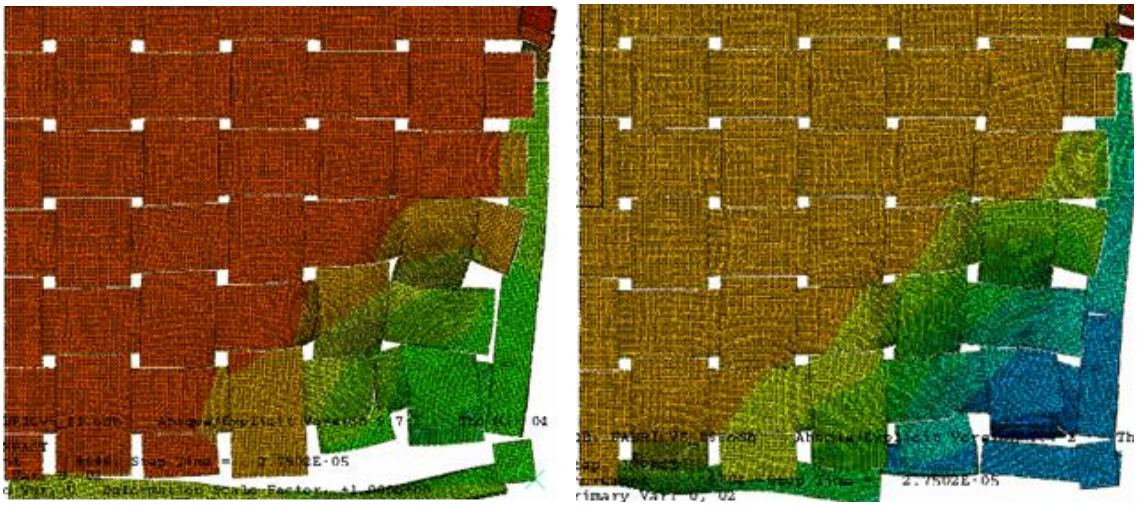

t = 27 μs

t = 38 μs

(a) (b)

Figure 4-38 Continued

Figure 4-39 shows the energy lost by the projectile with varying yarn-yarn friction.

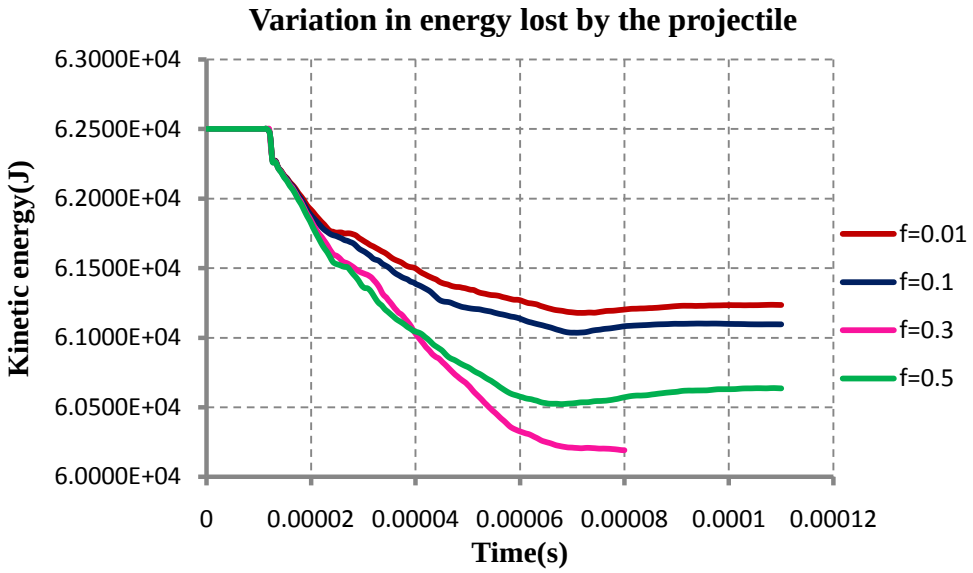

Figure **4**-39 Kinetic energy lost by the projectile for different friction coefficients

Figure 4-40 shows the increase in the fabric strain energy for the three representative cases.

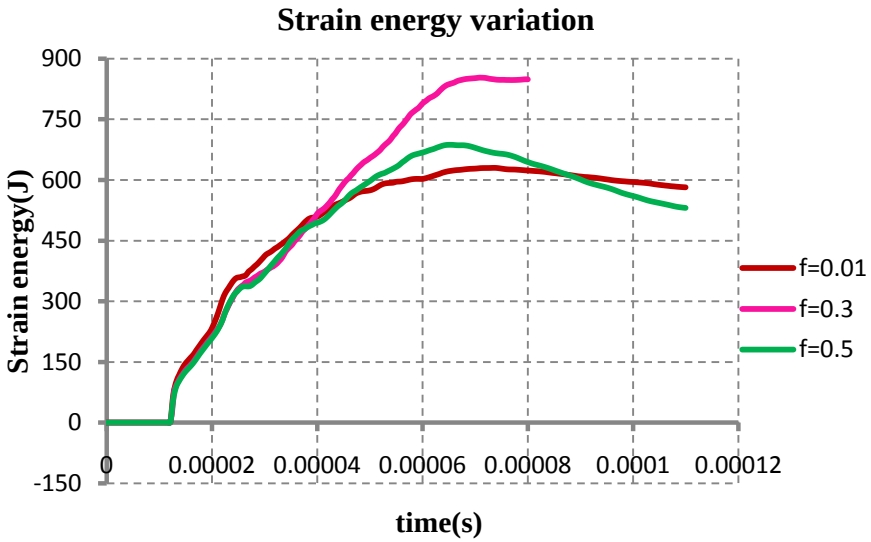

Figure 4-40 Increase in the fabric strain energy

Figure 4-41 shows the frictional dissipation plots for the cases f =0.01 and f =0.5.

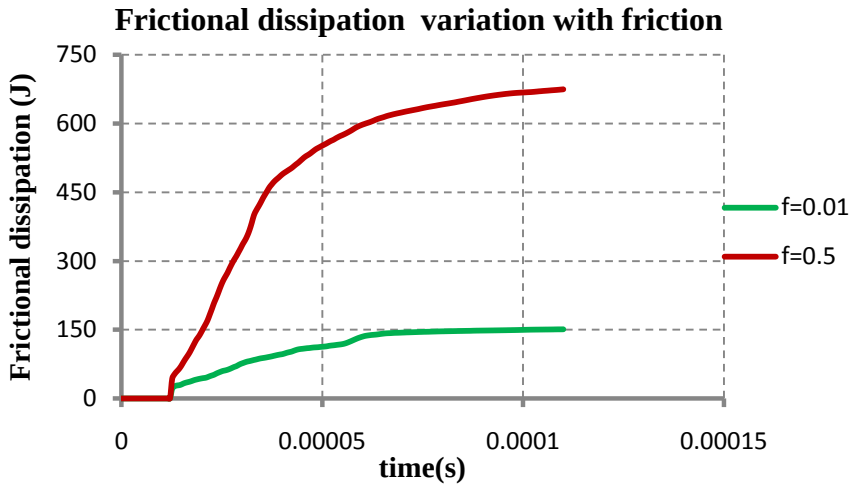

Figure 4-41 Frictional dissipation in the fabric

Observations

From Figure 4-39 it is clearly seen that as the friction between the yarns increases, the energy absorbed by the fabric also increases. However, the energy absorbed when the friction coefficient *f* is 0.5 is less than that when *f* is 0.3.

The result indicates that the fabric with the higher friction slows down the projectile more quickly than the fabric with no friction. As more yarns are involved and are forced to move at a quicker speed as seen in Figure 4-38, there was more kinetic energy for the cases with higher friction coefficients. From the deformation contours it can be noted the fabric with the higher friction held the projectile for a longer time, i.e., the failure of yarns is delayed. But as the yarn-yarn friction increases beyond a certain level, it hinders the relative motion between yarns and resists decrimping of the fabric weave tightness, thereby inducing the fabric to fail earlier during impact. This can be clearly seen in the Figure 4-42 which shows a decrease in strain energy of the fabric for f =0.5.

Figure 4-42 shows the fabric's von Mises stress history for an element near the impact zone in the two cases of f =0.01 and f =0.5.

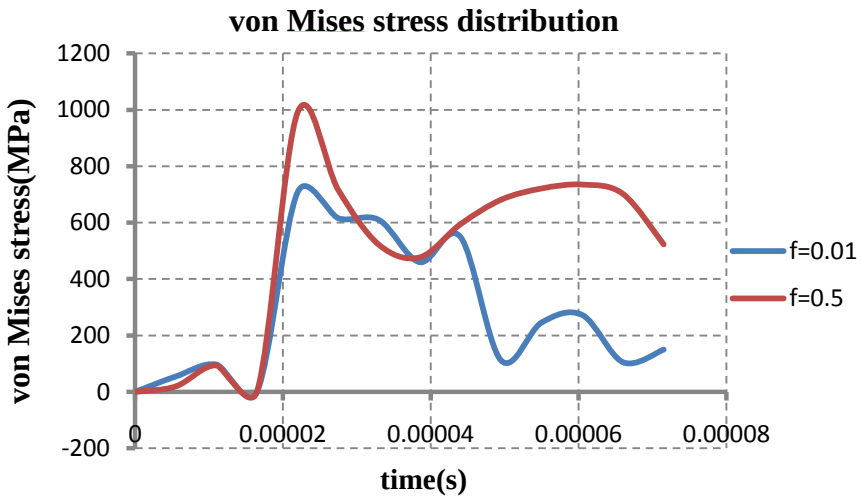

Figure 4-42 von Mises stress history for an element near the impact zone

It is observed that the stress levels are higher for the case with f=0.5 case. This can be attributed to the fact that the presence of friction hinders the lateral motion of yarns, and thereby leading to more yarns that are loaded. Due to the higher stresses, more strain energy was stored for the case with f=0.5. This is consistent with the predictions of Duan et al. [21].

Table 4-10 Comparison of the energy history

	f=0.01	f=0.5
KE lost by the bullet	1270 J	1900 J
SE gained by the fabric	630 J	690 J
Frictional dissipation	160 J	670 J

Table 4-10 compares the energy histories for the two cases with f =0.01 and f =0.5.

Comparing the two cases with f =0.01 and f =0.5, it can be seen that the total fabric energy absorption for the case with f =0.01 is only 58% of the value when f =0.5. For the case where μ=0.01, the kinetic energy lost by the projectile is mostly absorbed by the fabric as the strain energy and kinetic energy of the fabric. As the penetration process advances in time, it can be observed that the yarn strain energy becomes the primary energy absorption mechanism contributing 81% of the total absorbed energy for the case with f =0.01.

However, for the case with f =0.5 it is observed from Figure 4-41 that the frictional dissipation accounts for a small portion of energy before the yarn breakage initiates at 38 μs, but the yarn strain energy increases in the presence of friction. Also, as time progresses, the frictional dissipation accounts for almost 49% of the total energy absorbed by the fabric. Hence, it can be concluded that the energy dissipated via frictional sliding is an important energy absorbing mechanism only after the yarn breakage initiates.

4.3 Conclusions and future work

A finite element model has been developed to study the ballistic responses of the Twaron CT709® plain weave fabrics. ABAQUS/Explicit is used, and a user subroutine VUMAT is incorporated in the analysis to define the material behavior of the fabrics. The residual velocities obtained from the current model correlate well with the published

experimental data. The simulation results provided in the present study include bullet residual velocity, fabric deformation and damage pattern, kinetic energy of the system, fabric strain energy, frictional dissipation energy, and impact force on the bullet.

Parametric studies have been carried out at velocities higher than ballistic limit and lower than critical velocity to analyze the system responses to different variables associated with the impact phenomenon. These studies can be summarized as follows.

4.3.1 Impact velocity

By varying the impact velocity, it was observed that the fabric deformation is more localized near the impact region. At low impact velocities, the fabric deformation is distinguished by extensive stretching and creasing which results in higher energy absorption in the form of strain energy. However, as the impact velocity increases, the damage is more localized and the yarns fail long before any significant transverse deflection of the fabric can occur.

4.3.2 Projectile mass

Increased projectile mass implies an increased energy of impact. As the fabric offers almost the same resistance irrespective of the projectile mass, the strain energy absorbed by the fabric for different projectile masses remains about the same. Hence, the loss in kinetic energy of the projectile decreases, leading to an increased residual velocity.

4.3.3 Projectile shape

Projectile shape is found to have a significant effect on the ballistic properties. For sharper projectiles, the wedge-through phenomenon was found to be predominant. Instead of breaking yarns, sharper projectiles tend to push aside the yarns and slip through the initial perforation. Hence, for sharp projectiles, the loss in kinetic energy is lower. In the case of blunt projectiles, the energy absorbed is much higher, as a greater area of the projectile is in contact with the fabric at the time of impact, thereby distributing the load to a greater number of yarns.

4.3.4 Gripping conditions

Far-field gripping conditions were found to be have a much pronounced effect only for low velocity impacts, as the fabric has sufficient time to stretch and the transverse wave can propagate to the edges. It was observed that at a low impact velocity the fabric constrained at two edges shows a better energy absorbing capability because of the higher fabric kinetic energy due to the pull out of yarns from the unclamped edges.

It was also seen that the fabric clamped at two edges arrests the projectile for a longer time without failure of yarns than the fabric with all four edges clamped. At high velocity impacts, the far field boundary conditions were found to have no significant effect on the ballistic behavior.

4.3.5 Number of fabric layers

The impact response to the number of fabric layers is also studied. It was observed that an increase in the number of layers leads to much higher energy absorption. More number of layers beyond a certain limit, however, adds bulk materials to the system, and the ultimate goal of maximizing the strength to weight ratio is compromised.

4.3.6 Friction

The effect of inter-yarn friction on the fabric energy absorption is analyzed. It was found that the presence of friction enhances the amount of energy absorbed by the fabric by increasing the number of yarns carrying the impact load and additional energy loss through frictional dissipation due to slippage. It is concluded that the optimal level of inter-yarn friction is between 0.3-0.5 to achieve the maximum energy absorption.

The present study successfully utilizes the combination of 3D weave architecture and the strain rate dependent material behavior. Most of the existing work is based either on geometrical simplifications or on assumptions material behavior. Another significant advantage with the present approach is that the mechanical constitutive relation, coded in FORTRAN®, is universal in applications. The desired material behavior can be obtained by just varying the material constants in the code. This allows for the extension of this work to fabric materials which exhibit a strain-rate dependent behavior in addition to the Twaron® fabric.

The findings pertaining to the optimal number of fabric layers and inter-yarn friction levels can aid in the manufacturing of fabrics with desired level of lubrication/additives to improve the fabric performance under impact.

The impact process is a complex phenomenon, and no model can be completely accurate to replicate the exact fabric behavior. The finite element modeling involves many simplifying assumptions on geometry, and material behavior, which lead to slight discrepancies in the predictions. For example, the residual velocity predictions in the current study are more conservative than the experimental values, though the relative error is very low. With regard to the geometry, the current analysis is limited to only a single yarn undulation. The effect of yarn undulations can be studied to understand the influence of the type of weaving on the impact behavior. Also, the effect of the size of fabric patch can be explored.

It is assumed in this study that the failure of the Twaron fibers is controlled by the maximum stress. This approximation is applicable only for the high velocity impact cases. A thorough experimental study on the failure behavior of fibers at various strain rates is required to understand the exact damage propagation. For a less complex implementation of the VUMAT, the mechanical properties such as the Young's modulus of the Twaron yarns are assumed to be constant with time. In reality, however, such properties vary with the applied strain rate. Realistic implementation of these strain rate dependant properties has to be incorporated into the VUMAT subroutine. A more sophisticated contact algorithm between the overlapping yarns also needs to be proposed to reduce the computational time.

Considering all things, the study of ballistic fabrics as armor materials is of growing importance and the need to identify lighter and stronger advanced materials for body armor applications is a necessity. This supports what was concluded in David, Gao and Zheng [1] in a more general context.

REFERENCES

[1] David NV, Gao XL, Zheng JQ. Ballistic resistant body armor: Contemporary and prospective materials and related protection mechanisms. Applied Mechanics Reviews 2009;62(5):050802-20.

[2] Teijin. Twaron. http://www.teijinaramid.com/smartsite.dws?id=20090. (February 27, 2009).

[3] Mary Bellis. History of body armor and bullet proof vests: Designs developed of a bullet proof vest made of seven layers of Kevlar fabric. http://inventors.about.com/od/bstartinventions/a/Body_Armor_2.htm. (January 24, 2010).

[4] Monster. Ballistic test setup. http://defensetech.military.com/archives/cat_armor.html. (December 15,2010).

[5] Mall S, Gao XL. A two-dimensional rule-of-mixtures micromechanics model for woven fabric composites. ASTM Journal of Composites Technology and Research 2000;22(2):60-70.

[6] Fiber Materials Inc. 2-D woven structures. http://www.fibermaterialsinc.com/2Dws.htm. (December 23, 2005)

[7] Gu B. Analytical modeling for the ballistic perforation of planar plain-woven fabric target by projectile. Composites Part B: Engineering 2003;34:361-371.

[8] Naik NK, Shrirao P, Reddy BCK. Ballistic impact behaviour of woven fabric composites: Formulation. International Journal of Impact Engineering 2006;32: 1521-1552.

[9] Sedgwick RK, Hageman LJ, Herrmann RG, Waddell JL. Numerical investigations in penetration mechanics. International Journal of Engineering Science 1978;16: 859-869.

[10] Chen EP. Finite element simulation of perforation and penetration of aluminum targets by conical-nosed steel rods. Mechanics of Materials 1990;10:107-115.

[11] Vinson JR, Zukas JA. On the ballistic impact of textile body armor. ASME Journal of Applied Mechanics 1975;42(6):263-268.

[12] Ching TW, Tan VBC. Modelling ballistic impact on woven fabrics with LS-DYNA, in: Liu GR, Tan VBC, Han X. (Eds.) Computational methods. The Netherlands: Springer 2006. p. 1879-1884.

[13] Simons W, Erlich DC, Shockey DA. Finite element design model for ballistic response of woven fabrics. In: Proceedings of the 19th international symposium on ballistics, Interlaken, Switzerland, 2001. p. 1415-22.

[14] Lim CT, Shim VPW, Ng YH. Finite-element modeling of the ballistic impact of fabric armor. International Journal of Impact Engineering 2003;28:13-31.

[15] Gu B. Ballistic penetration of conically cylindrical steel projectile into plain-woven fabric target: A finite element simulation. Journal of Composite Materials 2004; 38:2049-2074.

[16] Rao MP, Nilakantan G, Keefe M, Powers BM, Bogetti TA. Global/local modeling of ballistic impact onto woven fabrics. Journal of Composite Materials 2009;43: 445-467.

[17] Shahkarami A, Vaziri R, Poursartip A. A numerical investigation of the effect of projectile mass on the energy absorption of fabric panels subjected to ballistic impact. In: Proceedings of the 20th international symposium on Ballistics, Orlando, FL, 2002.

[18] Stronge WJ. Impact mechanics. Cambridge: Cambridge University Press; 2000.

[19] Smith JC, McCrackin FL, Schiefer HF, Stone WK, Towne WK. Stress-strain relationships in yarns subjected to rapid impact loading: Part V: Wave propagation

in long Textile yarns impacted transversely. Textile Research Journal 1958;28: 288-302.

[20] Cheeseman BA, Bogetti TA. Ballistic impact into fabric and compliant composite laminates. Composite Structures 2003;61:161-173.

[21] Duan Y, Keefe M, Bogetti TA, Cheeseman BA. Modeling friction effects on the ballistic impact behavior of a single-ply high-strength fabric. International Journal of Impact Engineering 2005;31:996-1012.

[22] Wang SS, Roylance D. Penetration mechanics of textile structures: Influence of non-linear viscoelastic relaxation. Polymer Engineering & Science 1978;18:1068-1072.

[23] Shockey DA, Simons JW, Erlich DC. Improved barriers to turbine engine fragments: Interim Report I. DOT/FAA/AR-99/8, I, June 1999.

[24] Shim VPW, Lim CT, Foo KJ. Dynamic mechanical properties of fabric armour. International Journal of Impact Engineering 2001;25:1-15.

[25] Termonia Y, Meakin P, Smith P. Theoretical study of the influence of strain rate and temperature on the maximum strength of perfectly ordered and oriented polyethylene. Macromolecules 1986;19(1):154-159.

[26] ABAQUS. Theory manual, version 6.7, Simulia, 2008.

[27] Ahmad MR, Ahmad WYW,Salleh J, Samsuri A. Performance of natural rubber coated fabrics under ballistic impact. Malaysian Polymer Journal 2007;24:39-51.

[28] Dong Z, Sun CT. Testing and modeling of yarn pull-out in plain woven Kevlar fabrics. Composites Part A: Applied Science and Manufacturing 2009;40(12): 1863-1869.

[29] Rebouillat S. Tribological properties of woven para-aramid fabrics and their constituent yarns. Journal of Materials Science 1998;33(13):3293-3301.

[30] Committee on materials for lightweight military vehicles. Report of the Materials for lightweight military combat vehicles. National Materials Advisory Board. NMAB-396, Washington, D.C.: National Academy Press, 1982.

[31] Barauskas R, Ausra A. Computational analysis of impact of a bullet against the multilayer fabrics in LS-DYNA. International Journal of Impact Engineering 2007; 34(7):1286-1305.

[32] Lee SK, Byun JH, Hong SH. Effect of fiber geometry on the elastic constants of the plain woven fabric reinforced aluminum matrix composites. Materials Science and Engineering A 2003;347(1-2):346-358.

[33] Bicerano J. Prediction of polymer properties, 2nd ed. New York: Marcel Dekker, 1996.

[34] Richter F.Upsetting and viscoelasticity of vitreous SiO2: Experiments, interpretation and simulation. PhD dissertation, Technische Universität Berlin, Germany, 2006.

[35] David NV, Gao XL, Zheng JQ. Modeling of viscoelastic behavior of ballistic fabrics at low and high strain rates. International Journal for Multiscale Computational Engineering 2009;7(4):295-308.

[36] Shim VPW, Tan VBC, Tay TE. Modelling deformation and damage characteristics of woven fabric under small projectile impact. International Journal of Impact Engineering 1995;16(4):585-605.

[37] Tan VBC, Ching TW. Computational simulation of fabric armour subjected to ballistic impacts. International Journal of Impact Engineering 2006;32(11):1737-1751.

[38] Briscoe BJ, Motamedi F. The ballistic impact characteristics of aramid fabrics: The influence of interface friction. Wear 1992;158(1-2):229-247.

[39] Talebi H, Wong SV, Hamouda AMS. Finite element evaluation of projectile nose angle effects in ballistic perforation of high strength fabric. Composite Structures 2009;87(4):314-320.

[40] Tan VBC, Lim CT, Cheong CH. Perforation of high-strength fabric by projectiles of different geometry. International Journal of Impact Engineering 2003;28(2): 207-222.

[41] Chitrangad. U.S.Patent 5,275,873, 4 January1994. Ballistic structure.

[42] Lee BL, Walsh TF, Won ST, Patts HM, Song JW, Mayer AH. Penetration failure mechanisms of armor-grade fiber composites under impact. Journal of Composite Materials 2001;35(18):1605-1633.

[43] Shockey DA, Simons JW, Erlich DC. Improved barriers to turbine engine fragments: Final annual Report. DOT/FAA/AR-99/8, 2000.

[44] Karahan M, Kus A, Eren R. An investigation into ballistic performance and energy absorption capabilities of woven aramid fabrics. International Journal of Impact Engineering 2008;35(6):499-510.

VITA

Name:	Sireesha Gogineni
Address:	3123 TAMU, College Station, TX 77843-3123, c/o Xin-Lin Gao
Email Address:	siri.gogineni@gmail.com
Education:	B.E., Mechanical Engineering, Osmania University, 2007
	M.S., Mechanical Engineering, Texas A&M University, 2010